

分子システム解析チーム

(チームリーダー：田原 太平)

二次元蛍光寿命相関分光法による シトクロム *c* のマイクロ秒構造ダイナミクス解析

乙須拓洋, 石井邦彦, 田原太平

理研・田原分子分光

蛋白質のダイナミクスにはピコ秒から秒に至る幅広い時間階層性があり、その本質的な理解には各時間領域での構造ダイナミクスの定量的な解析が重要である。特にマイクロ秒領域は蛋白質折れ畳みの初期過程に対応しており、また MD シミュレーションと実験の直接比較が可能であることから、分子レベルでのダイナミクス理解において重要な時間領域である[1]。しかしながら、現在普及している解析手法である一分子計測の時間分解能は 100 マイクロ秒程度であり、マイクロ秒領域での詳細な解析はこれまで研究が進んでいなかった。

我々の研究室では最近、マイクロ秒の時間分解能で定量的な解析を可能とする二次元蛍光寿命相関分光法 (2D-FLCS) を開発した[2]。本手法は共焦点顕微鏡の焦点領域から検出された一分子由来の蛍光光子について、光子間の蛍光寿命の相関を解析する手法であり、構造に敏感な蛍光寿命を通して蛋白質の構造不均一性や構造間ダイナミクスを理解することができる (図 1)。本研究では、2D-FLCS の蛋白質研究への初めての応用として、酸性条件下でのシトクロム *c* の構造ダイナミクスを解析した[3]。

本研究に際し、シトクロム *c* の C 端領域に蛍光共鳴エネルギー移動 (FRET) のドナーとなる色素を付与し、シトクロム *c* に内在するヘム鉄への FRET に由来するドナー蛍光寿命の変化を、シトクロム *c* 構造変化のプロブとして解析した。まず始めに異なる pH 条件での蛍光寿命解析を行い、ドナーの蛍光寿命がシトクロム *c* の酸変性過程に伴う構造変化を反映していることを確認した。そこで変性中点である pH 3.5 において 2D-FLCS による測定・解析を行った結果、複数の蛍光寿命成分が観測された (図 2 a)。それらのうち 70 ps, 280 ps の 2 つの成分の間のクロスピークは、 $\Delta T = 0.2\text{-}4 \mu\text{s}$ の二次元マップには見られなかったのに対し、 $\Delta T = 8\text{-}12 \mu\text{s}$ のマップにおいてははっきりと確認された。クロスピークは関与する二つの蛍光寿命成分間の交換が ΔT の間に起こっていることを意味する。つまりこの結果は 70 ps 成分と 280 ps 成分の間の交換が約 $5 \mu\text{s}$ 程度の時定数で起こっていることを強く示唆する。別に行った蛍光寿命解析の結果、短寿命成分がシトクロム *c* の天然状態に帰属されたことから、本解析の結果はシトクロム *c* の天然状態と変性中間状態間の構造転移ダイナミクスが約 $5 \mu\text{s}$ で起こっていることを意味する。シトクロム *c* は古くから調べられている折れ畳み研究のモデル蛋白質であるが、2D-FLCS を用いた本研究により初めてマイクロ秒領域

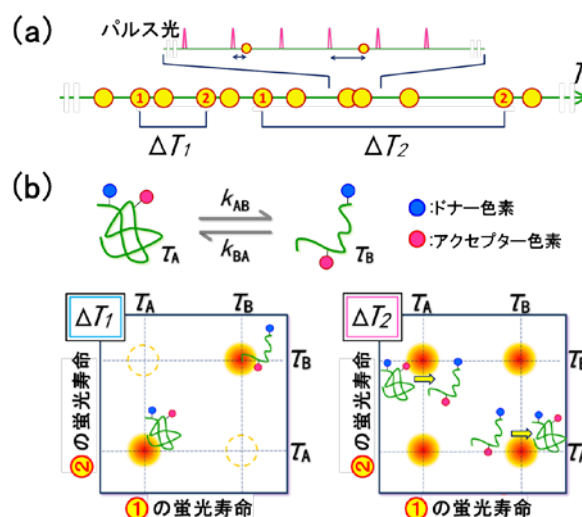


図 1. 2D FLCS の概要。(a) 検出される蛍光光子の模式図。パルス光から蛍光検出までの遅延時間が蛍光寿命の情報を与える。(b) 二つの構造間でのダイナミクスがあるときに期待される結果。二つの光子間の時間差(ΔT)が構造間ダイナミクスの時定数より長い場合、構造間転移が二次元マップ上のクロスピークとして表れる(ΔT_2)。

の天然状態構造のダイナミクスを観測することができた。その他のピークについても考慮すると、3つの変性中間体 (I_1 , I_2 , I_3) を含むシトクロムcの複雑な折れ畳みモデル (図2b) が示唆される。

本研究ではさらに、2D-FLCSをさまざまな ΔT で行い、検出された各ピーク (=準安定構造) の相関関数を抽出した。得られた相関関数について理論関数によるフィッティングを行った結果、新たに変性中間状態 (I_2+I_3)、ならびに変性状態 (U) のマイクロ秒ダイナミクスを検出することに成功した (図3a)。二次元マップ上にクロスピークが検出されなかったのは、これらが蛍光寿命の非常に短い (本測定的时间分解能以下) 成分との間でのダイナミクスであるためであることが他の実験より示唆された。以上の結果、最終的に図3bのような折れ畳みモデルを提案した。本解析より、シトクロムcの非常に複雑な構造転移機構が初めて明らかとなった。

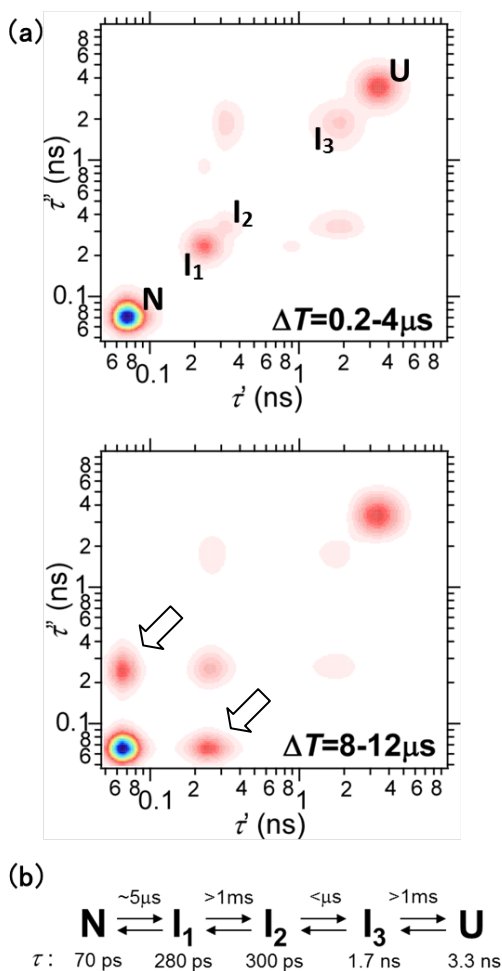


図2. (a) 異なる ΔT で得られたシトクロム c の蛍光寿命相関マップ。検出された天然状態と変性中間体間のクロスピークを矢印で示している。(b) 蛍光寿命相関マップのピークパターン解析より示唆されたシトクロム c の構造転移スキーム。

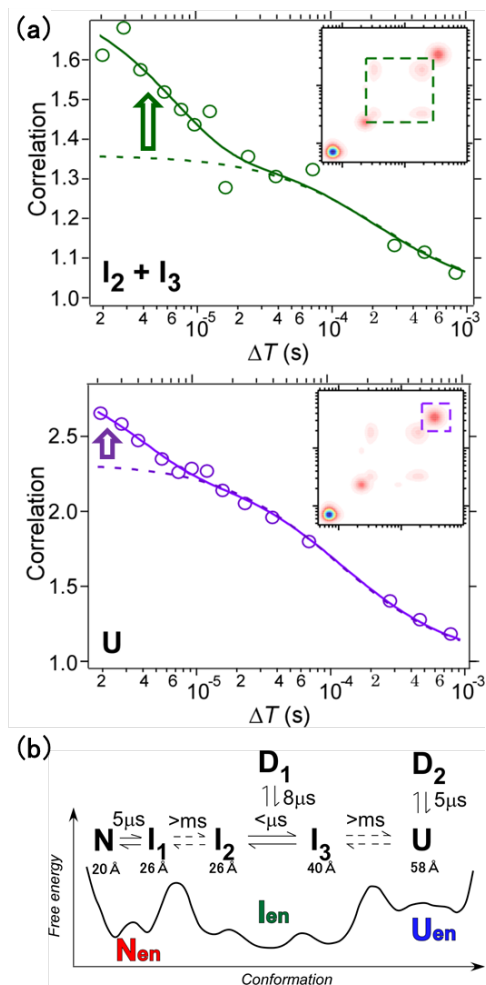


図3. (a) 変性中間状態 (I_2+I_3) ならびに変性状態 (U) の蛍光強度の自己相関。マイクロ秒のダイナミクスに起因する相関振幅を矢印で強調している。(b) 最終的に提案したシトクロム c の構造転移スキームと自由エネルギー地形。

【参考文献】

- [1] Shaw, D.E., et al. *Science* **2010**, 330, 341. [2] Ishii, K.; Tahara, T. *J. Phys. Chem. B* **2013**, 117, 11414.& 11423. [3] Otsu, T; Ishii, K; Tahara, T. *submitted*.

蛍光相関分光におけるアフターパルス効果の補正法の開発

石井邦彦, 田原太平

理研・田原分子分光

蛍光相関分光法 (Fluorescence Correlation Spectroscopy, FCS) は生体分子のマイクロ秒オーダーの自発的な揺らぎを観測する有力な手段であり、我々はこれを利用した新しい分光法の開発と応用を進めている[1,2]。FCSを数マイクロ秒の時間領域で応用する際に問題となる点の一つは、光子検出器として用いられるアバランシェフォトダイオード (APD) のアフターパルス効果である。アフターパルスは本来の光子信号パルスが発生してからある遅延時間 (数マイクロ秒以下) 経った後に、偽のパルス信号が確率的に発生する現象である。この影響で、数マイクロ秒までの時間領域で蛍光相関信号が大きく歪むことが知られている。これを避けるため、通常はAPDを2台用いてそれらの相互相関信号のみを利用するのが一般的である。しかし、この方式では得られた光子対の半分が使用されず非効率であるだけでなく、蛍光相関計測の多チャンネル化[3]や多色化[4]など分子ダイナミクス計測の高度化を目指す際には光学配置が煩雑になるという問題が無視できなくなる。従って、より簡便に蛍光相関信号に対するアフターパルスの影響を評価し、分離することが重要である。

我々は光子信号の解析においてアフターパルス効果を補正するために、相関信号の時間反転対称性を用いる方法を検討した[5]。この方法では、試料溶液をパルス励起し、発生した蛍光光子の励起 - 検出遅延時間を時間相関光子計数法 (TCSPC) で計測する。蛍光プローブ分子からの蛍光は一般に指数関数的に減衰する遅延時間特性を示すが、アフターパルスは通常蛍光よりはるかに長い時間領域で発生するため、蛍光寿命の時間スケールでは遅延時間の分布はほぼ平坦になる。そこで各光子の遅延時間のデータを用いて相関信号を展開した二次元蛍光遅延時間相関マップ[1,2]を作成し、このマップの対称性を調べる。真の蛍光信号のみからなるマップは、系が平衡状態にある場合、詳細釣り合いの原理から、対角線を挟んで対称な形になると予測される (図1 a)。一方アフターパルス効果による偽の光子信号は、必ず別の光子信号の後に発生するため、時間反転対称性が破れ、二次元マップが非対称な形になる (図1 b)。そこでこの非対称性を定量的に評価することで、アフターパルスの発生確率を求め、その寄与を相関信号から差し引くことができる。

この方法の有効性を確かめるため、蛍光色素分子を用いて検証実験を行った。図2はテトラメチルローダミン (TMR) の蛍光相関信号である。黒点線は2台のAPDを用いた従来法により得られた相互相関信号、青線はその内1台の出力のみから計算した自己相関信号である。自己相関信号のサブマイクロ秒領域に顕著に見られる減衰成分がアフターパルスの効果である。(ただし 10^{-7} sでの相関信号の消失はTCSPCの不感

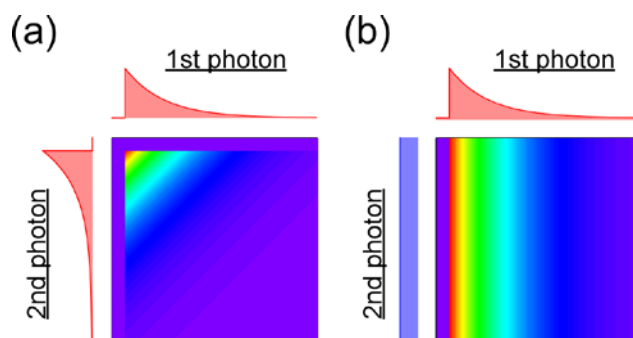


図1. 予想される二次元蛍光遅延時間相関マップの形状。(a)真の蛍光信号。(b)アフターパルス効果。

時間によるものである。) この自己相関信号から上記の方法でアフターパルスの寄与を差し引いたもの(赤線)はほぼ完全に相互相関信号の形を再現しており、アフターパルスの影響を取り除けていることが確認できる。

図3はTMRとCy3の2種類の蛍光色素を混合した試料の蛍光相関信号である。これらの色素は大きく異なる蛍光寿命(TMR:2.4 ns, Cy3:0.18 ns)をもつが、この場合でも今回の方法でアフターパルスの影響を取り除くことができている。緑点線で示したのは発光遅延時間を利用した別のアフターパルス補正法[6]を適用した結果であるが、相互相関信号と比較すると、系統的に相関強度を低く評価していることが分かる。これは試料分子の蛍光寿命の不均一性に起因するものであるが、一方で時間反転対称性の情報を取り入れた今回の方法はこのような不均一性が存在する場合でも有効であることが示された。

以上のように、本手法によりサブマイクロ秒までの時間領域において単一の検出器のみを用いて正確な蛍光相関関数を計測することが可能となった。この方法は我々が独自に開発した二次元蛍光寿命相関分光法(2D-FLCS) [1,2]と組み合わせて使うことができる。これにより2D-FLCSの多色化・多点化などの拡張が容易になり、生体分子のマイクロ秒領域の自発揺らぎをより精度良く調べることができるようになると期待される。

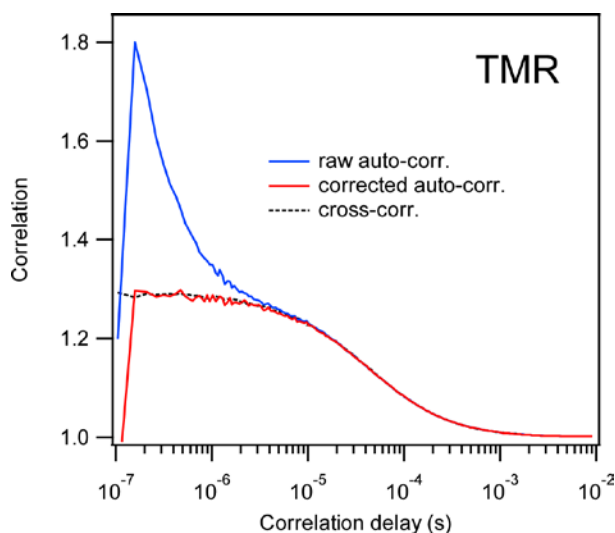


図2. TMRの蛍光相関信号。

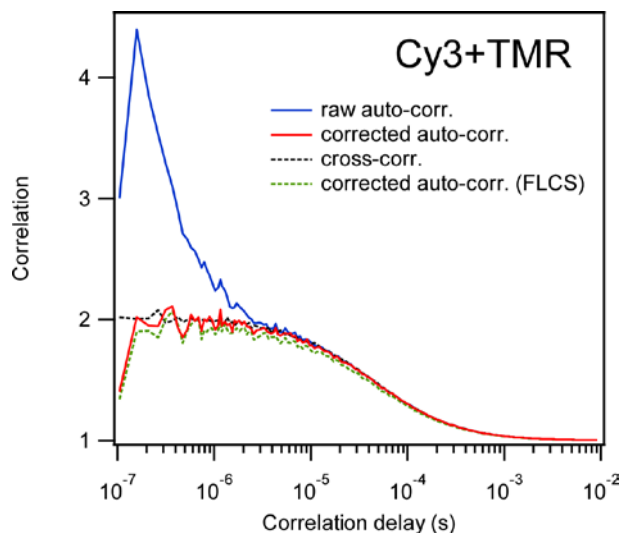


図3. TMRとCy3の混合試料の蛍光相関信号。

【参考文献】

- [1] Ishii, K.; Tahara, T. *J. Phys. Chem. B* **2013**, *117*, 11414.
- [2] Ishii, K.; Tahara, T. *J. Phys. Chem. B* **2013**, *117*, 11423.
- [3] 乙須拓洋・石井邦彦・田原太平, 第7回分子科学討論会, 2013, 2D21.
- [4] 石井邦彦・Chao-Han Cheng・田原太平, 第7回分子科学討論会, 2013, 2D20.
- [5] 石井邦彦・田原太平, 第6回分子科学討論会, 2012, 1P086.
- [6] Enderlein, J.; Gregor, I. *Rev. Sci. Instrum.* **2005**, *76*, 033102.

蛍光相関分光法の測定時間短縮に向けた 多焦点共焦点顕微鏡システムの開発

乙須拓洋, 石井邦彦, 田原太平

理研・田原分子分光

我々が最近開発した二次元蛍光寿命相関分光法 (2D-FLCS) は、蛋白質をはじめとする生体高分子の複雑なダイナミクスを、高い時間分解能で定量的に解析することができる新しい手法である [1]。我々はこれまでヘアピン DNA [1] やシトクロム *c* [2] をサンプルとして用い、それらのマイクロ秒構造転移ダイナミクスの解析を行うことにより、本手法の有用性を示してきた。しかしながら、原理的に本手法ではきわめて多くの光子データとそのための長時間測定が必要とされる。実際我々が行ったシトクロム *c* の解析においては、データ取得に 6 日間の信号積算を要した。この点を克服すべく本研究では多焦点共焦点顕微鏡の開発を行い、同等の光子データを複数の焦点領域から同時取得することにより測定時間の短縮を試みた。

本研究では対物レンズの無限遠補正光学系を利用した多焦点形成を行った。無限遠系の対物レンズの焦点面上の点光源から発せられる光は対物レンズを通過することで平行光として伝播する (図 1)。点光源が二つであった場合これらに由来する平行光は光軸との角度が異なっており、これらを適切なフォーカスレンズ (対物レンズによって定められており、図では $f = 200$ mm) で結像させると対物レンズの倍率に従った像が得られる (図 1 a)。一方でフォーカスレンズがない状況では、これら二つの平行光の中心間距離は対物レンズからの距離に伴い広がっていき、図 1 に示すような 100 倍対物レンズでは、点光源間の距離が $10 \mu\text{m}$ であった場合、 200 mm 地点で 1 mm、 2 m 地点では 10 mm となる。このことは逆に、 2 m 地点で 10 mm の中心間距離を有する二つの平行光を対物レンズの瞳に入射することにより、 $10 \mu\text{m}$ 離れた二つの焦点を形成できることを意味している (図 1 b)。

図 2 に無限遠系を利用した多焦点共焦点顕微鏡の概略図を示す。チタンサファイアレーザーのパルス光出力 (800 nm、 100 fs、 80 MHz) をフォトニック結晶ファイバーに集光して白色光を発生させ、バンドパスフィルターで目的の波長の光を取り出し、蛍光励起光とした。励起光は 7 つの台形ビームスプリッターを用いて 8 つに分け、そのうちの 7 つを使用した。マルチミラー (M2) を用いて個別に角度を調整した 7 つの励起光を 5 m 程度の長い光路を経て対物レンズ ($60\times$, water immersion) の瞳に入射した。これにより、マルチミラー上での各励起光の中心間距離とミラーから対物レンズまでの距離に依存した相対空間配置を有する 7 つの焦点を試料上に形成することが可能となる (図 2 b)。各焦点から発せられる蛍光はバンドパスフィルターを通過させた後、集光レンズを用いてファイバーバンドルの端面上に結像させた。ファイバーバンドルは 7 本のファイバーを結像されるイメージに対応するように束ねたもので

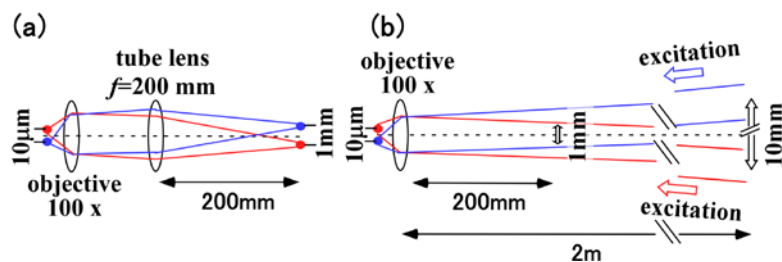


図 1. 無限遠補正光学系を利用した多焦点形成の概略図。

あり、ファイバーそれぞれが対応する焦点領域からの蛍光を収集する。収集された蛍光光子は単一光子アヴァランシェフォトダイオード (SPAD) で検出し、時間相関単一光子計数ボードで解析した。

まず始めに本装置を用いて通常の蛍光相関解析を行った。測定にはローダミン 6G のエチレングリコール (EG) 溶液 (2.5 nM) を用いた。通常、単一 SPAD を用いた相関解析では計数率に依存する時間原点のシフトやアフターパルスの影響が問題となるが、これらについては我々が開発した補正法により取り除いた[3,4]。その結果、図 3 に示すようにすべての焦点からほぼ同等の相関関数を得ることができた。

次に同じ試料を用いて蛍光寿命測定を行った。

各焦点から得られた蛍光減衰カーブには、EG からのラマン散乱、ならびに他の励起光によるバックグラウンド蛍光 (クロストーク) が検出された (図 4 矢印)。しかしながら、これらの寄与については 2D-FLCS により相関成分の蛍光減衰カーブを抽出することで完全に除去することができた (図 4 青線)。この結果は、クロストークが完全に無相関であることを示すとともに、本装置を用いて 7 つの焦点からクロストークフリーの相関成分を抽出可能、すなわち 2D-FLCS によるさらなる解析が可能であることを示している。これにより、本装置を用いることで 2D-FLCS の測定時間を単焦点系の 1/7 に短縮することが可能となった [5]。

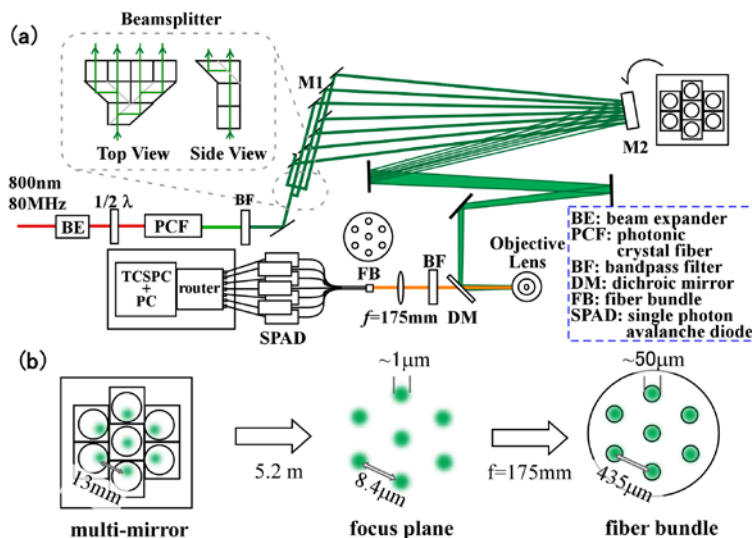


図 2. (a) 開発した多焦点共焦点顕微鏡の概略図。(b) マルチミラー、焦点、ファイバーバンドル端面での励起光、または結像イメージ。

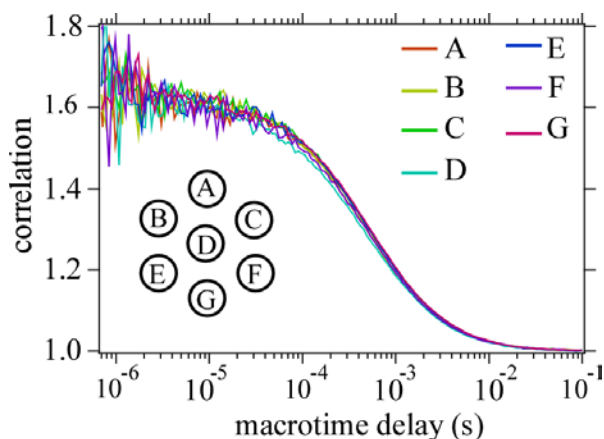


図 3. 本装置を用いて各焦点から得た相関関数。

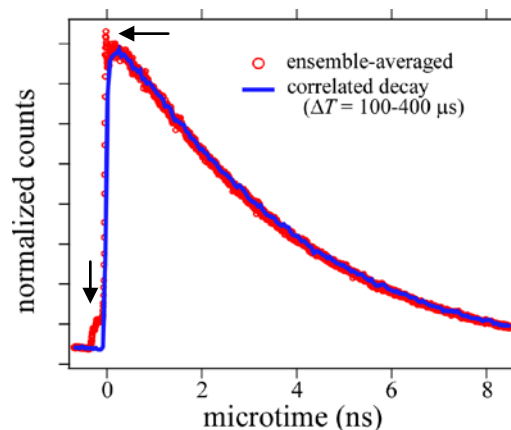


図 4. 本装置により得られた蛍光減衰カーブ (赤丸) と 2D-FLCS により抽出した相関成分の蛍光減衰カーブ (青線)。

【参考文献】

[1] Ishii, K.; Tahara, T. *J. Phys. Chem. B* **2013**, *117*, 11414.& 11423. [2] Otsu, T; Ishii, K; Tahara, T. submitted. [3] Otsu, T; Ishii, K.; Tahara, T. *Rev. Sci. Instrum.* **2013**, *84*, 036105. [4] Ishii, K.; Tahara, T. to be submitted. [5] Otsu, T; Ishii, K; Tahara, T. to be submitted.

帯電界面における水の構造とホフマイスター対イオン効果

二本柳聡史, 山口祥一, 田原太平

理研・田原分子分光

たんぱく質の溶解度に及ぼす塩効果の序列はホフマイスター系列として知られている(図 1)。この系列はたんぱく質の塩析のみならず、酵素活性のような複雑な生体機能から界面活性剤の臨界ミセル濃度のような単純な物性にいたるまで非常に多くの溶質の多様な物性に共通している。そのためホフマイスター系列を理解することは生物物理および物理化学の広範な学問領域において非常に重要である。しかしながら、その重要性にもかかわらず、その微視的なメカニズムについてはよくわかっていない。ホフマイスター塩効果は微視的には界面(たんぱく質/水溶液、界面活性剤/水溶液)の問題として捉えることができる。従って、溶質分子と共存イオンおよび溶媒である水の三者がなす界面の構造とそこでの相互作用を理解することがホフマイスター塩効果の理解にとって本質的に重要である。

我々が開発したマルチプレックスヘテロダイン検出振動和周波発生(HD-VSFG)分光法を用いると、非線形感受率($\chi^{(2)}$)の二乗を計測する従来法と異なり、 $\chi^{(2)}$ に対して線形なスペクトルを直接かつ比較的短時間で測定することができる¹。特に $\chi^{(2)}$ スペクトルの虚部($\text{Im}\chi^{(2)}$)は振動共鳴を直接反映し、さらに二乗による変形がないため、複雑な水のスペクトルの解析をする上で特に有利である。今回、我々はHD-VSFG分光法を用いて、正および負に帯電したイオン性界面活性剤単分子膜と種々の塩水溶液の界面における水の構造とホフマイスター系列との関係を調べた²。

図 2 にカチオン性の Cetyltrimethylammonium(CTA⁺)単分子膜と種々のナトリウム塩を含む同位体希釈水溶液界面における OH 伸縮領域の $\text{Im}\chi^{(2)}$ を示す。図2の $\text{Im}\chi^{(2)}$ スペクトルは 3100 から 3600 cm^{-1} の広範囲に渡って負のブロードな OH バンドを示す。バンドが負符号を持つのは信号を

与えている界面の水分子が平均して水素を下向きに配向していることに由来する。こ

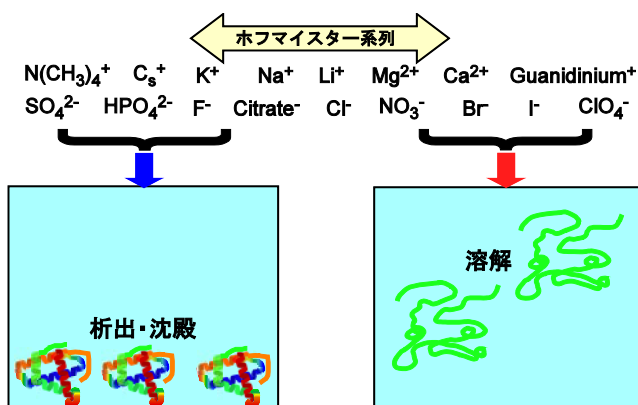


図 1. 上部に示すイオンのうち左側に示すイオンはタンパク質を析出・沈殿させる。中央に位置するイオンでは塩析の効果が小さくなり、右側のイオンは逆にタンパク質の溶解度を上げる働きをする。このようにイオンを加えた時に水溶液の性質がどれだけ変化するかの序列はホフマイスター系列と呼ばれ、非常に多くの溶質の多様な物性に共通してみられる。

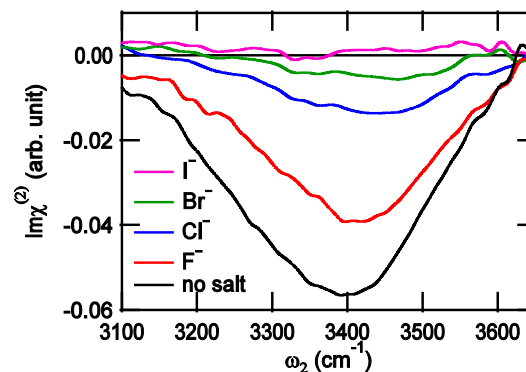


図 2. CTA⁺単分子膜/0.5M ナトリウム塩水溶液界面の $\text{Im}\chi^{(2)}$ スペクトル。(赤線) NaF、(青) NaCl、(緑) NaBr、(紫) NaI。参考のため塩を加えない場合のスペクトルを黒線で示す。

のような帯電界面では電気二重層内で配向している水が $\chi^{(2)}$ 活性となるので、信号強度は電気二重層の厚みに依存すると考えられる。実際、電気二重層が最も厚いとされる過剰塩を加えていない場合において最も強い OH バンドが観測されている(黒線)。塩を加えると二重層が圧縮されることにより OH バンドの強度は減少する。その中で、バンドの強度は F^- を含むものが一番大きく、 Cl^- , Br^- , I^- の順で小さくなる。これはサイズの大きなハロゲンイオンほど CTA⁺ 界面によく吸着し電気二重層を薄くするためと考えられる。特に I^- を含む場合は水の OH バンドがほとんど強度を持たず、この界面におけるイオンの吸着が主として接触吸着であることを示唆している。また、CTA⁺ 界面の OH バンド強度に見られるハロゲンの序列はホフマイスター系列と完全に一致している。従って、アニオンのホフマイスター系列は CTA⁺ 界面におけるアニオンの吸着力に起因すると考えられる。この結論は Cremer らが行った従来型の VSFG の研究結果と一致している³。

一方、図 3 に示す負に帯電した Dodecylsulfate (DS^-) 単分子膜界面におけるカチオンの効果は上述のアニオン効果とは異なる。ここで、図 3 の OH バンドが正の符号を持つのは負に帯電した界面において水分子が水素を上向きに配向していることを示す。重要な実験事実として、OH バンドの強度はカチオンのホフマイスター系列と一致しない。また、いずれのカチオンに対しても OH バンドが観測されたため、 DS^- 単分子膜界面におけるカチオンの吸着は非接触であると考えられる。従って、カチオンのホフマイスター系列の起源は界面とカチオンの接触吸着による直接的な相互作用ではありえない。一方、OH バンドの中央値を求めると Tetramethylammonium⁺ (TMA^+), Cs^+ , Li^+ , Mg^{2+} の順に高波数にシフトし、界面の水の水素結合強度の低下を示した。この序列は陽イオンのホフマイスター系列と一致する。従って、 DS^- 界面における水の水素結合構造とホフマイスター系列には相関があることが示唆された。以上から、ホフマイスター系列は、①界面と対イオンが接触吸着する場合はその吸着力(会合定数)、②界面とイオンが接触吸着しない場合は、界面の水の水素結合構造、これら 2 つの因子により決定されていると考えられる。

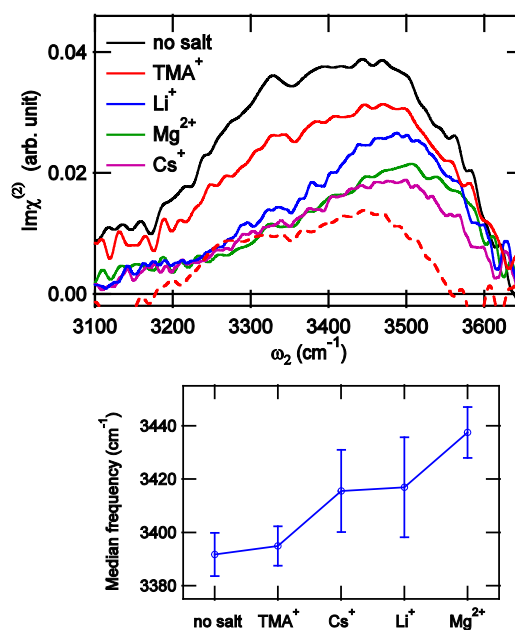


図 3. (上) DS^- 単分子膜/ $0.5M MCl_n$ 界面の $Im\chi^{(2)}$ スペクトル。(赤線) TMA^+ 、(青) Li^+ 、(緑) Mg^{2+} 、(紫) Cs^+ 。参考のため塩を加えない場合のスペクトルを黒線で示す。(下) OH バンドの中央値振動数とカチオンのホフマイスター系列の関係。

【参考文献】

- ¹ S. Nihonyanagi, S. Yamaguchi, and T. Tahara, *J. Chem. Phys.* **130** (2009) 204704.
- ² S. Nihonyanagi, S. Yamaguchi, and T. Tahara, *J. Am. Chem. Soc.* **136** (2014) 6155.
- ³ X. Chen, S. C. Flores, S.-M. Lim, Y. Zhang, T. Yang, J. Kherb, and P. S. Cremer, *Langmuir* **26** (2010) 16447.

Evaluation of pH at Neutral Lipid/Water Interfaces by Heterodyne-detected Electronic Sum Frequency Generation

Achintya Kundu, Shoichi Yamaguchi, Tahei Tahara
Molecular Spectroscopy Laboratory, RIKEN

The biological membrane is the boundary of a biological cell. One of the main structural components of the biological membrane is neutral lipid. The pH at the biological membrane is important for the formation of the membrane and the functional activity of the membrane. Therefore, it is essentially important to know the interface pH at the biological membrane.

We evaluated the interface pH at the lipid/water interfaces which mimic the biological membrane. The lipid/water interfaces were formed with lipids adsorbed at the air/water interface with their hydrophobic acyl chains pointing up towards the air and their hydrophilic head groups pointing down towards the bulk water.¹ pH spectrometry was applied to the lipid/water interfaces to evaluate the pH at the lipid interfaces using heterodyne-detected electronic sum frequency generation (HD-ESFG) and a pH indicator.^{2,3} The pH indicator was coadsorbed at the lipid/water interfaces with its alkyl chain aligned with the lipid acyl chains and its chromophore facing towards interfacial water. Figure 1 shows the lipid/water interface and the schematic representation of the experimental configuration.

We chose a surface active pH indicator, 4-heptadecyl-7-hydroxycoumarin (HHC). Figure 2a shows the acid-base equilibrium of the pH indicator. Studies were performed at the water interface with each of two neutral model lipids, shown in Figure 2b, 1,2-dipalmitoyl-*sn*-glycerol (DPG, nonionic) 1,2-dipalmitoyl-*sn*-glycero-3-phosphocholine (DPPC, zwitterionic).

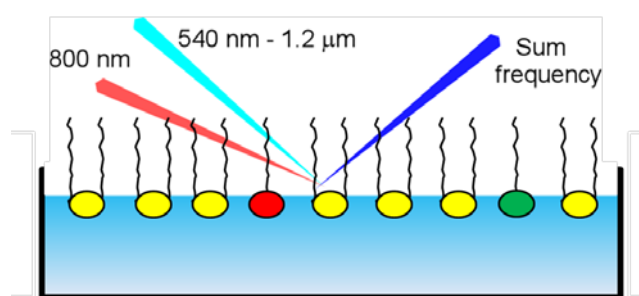


Fig. 1 Sketch of the lipid/water interface with pH indicator and the experimental configuration.

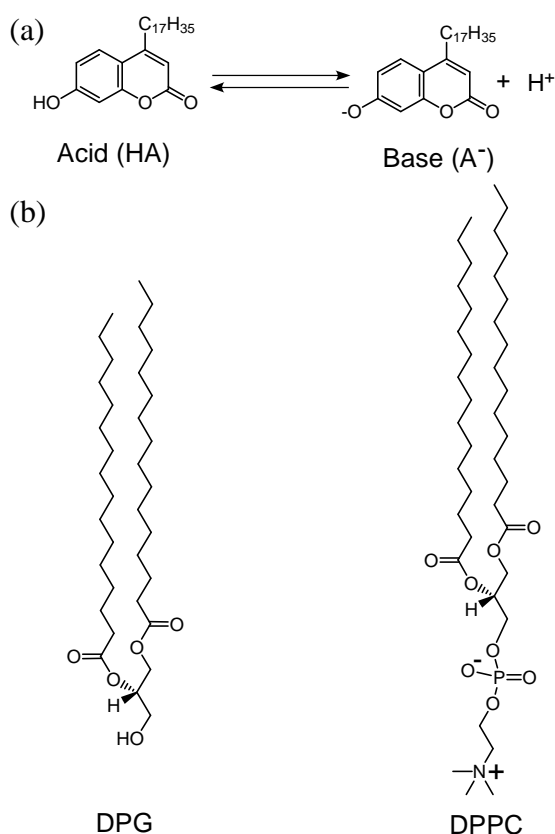


Fig. 2 (a) Acid-base equilibrium of the pH indicator, HHC. (b) Chemical structure of the two model lipids: DPG (nonionic) and DPPC (zwitterionic).

Figures 3a and 3b shows the interface selective electronic $\chi^{(2)}$ spectra of the pH indicator at the nonionic DPG/water interface. $\text{Im}\chi^{(2)}$ spectra (imaginary part of the $\chi^{(2)}$ spectra) exhibit an absorptive spectral feature, and these can be interpreted in the same way as UV-visible absorption spectra under the present two-photon resonant and one-photon nonresonant conditions.² The $\text{Im}\chi^{(2)}$ and $\text{Re}\chi^{(2)}$ (real part of the $\chi^{(2)}$ spectra) spectra exhibit isosbestic points approximately at 350 nm and 380 nm, which indicate only the acid-base equilibrium at the lipid/water interface.

By analyzing the bulk-pH dependence of the $\chi^{(2)}$ spectra, the bulk pH at which $[\text{HA}] = [\text{A}^-]$ is determined as 9.3. Generally, the pH is equal to the $\text{p}K_a$ (negative logarithm of the acid dissociation constant) when $[\text{HA}] = [\text{A}^-]$. However, this bulk pH at which $[\text{HA}] = [\text{A}^-]$ is not the $\text{p}K_a$ of the pH indicator at the DPG/water interface, because the pH is measured in the bulk. Assuming interfacial $\text{pH} = \text{bulk pH} + \Delta$, $\text{p}K_a$ is obtained as $9.3 + \Delta$.

The $\text{p}K_a$ is equal to the standard reaction Gibbs energy of $\text{HA} \rightarrow \text{H}^+ + \text{A}^-$ divided by $RT \ln 10$.

The standard reaction Gibbs energy is given as a function of the effective relative dielectric constant of the surrounding medium which can be estimated by the solvatochromism of A^- . The peak wavelength of the $\text{Im}\chi^{(2)}$ spectrum of A^- in Figure 3a allows us to estimate the effective relative dielectric constant of the DPG/water interface as 25. From this effective relative dielectric constant, the $\text{p}K_a$ of the pH indicator at the DPG/water interface is evaluated as 10.1. Because this $\text{p}K_a$ should be equal to $9.3 + \Delta$, Δ is obtained as +0.8. Similarly, we also estimate the pH at the zwitterionic lipid DPPC/water interface and find it to be lower than bulk by 0.6 pH units.

Although, both DPG and DPPC are neutral lipids, the pH at the DPG/water interface is higher than that in bulk whereas the pH at the DPPC/water is lower than that in bulk. This work clearly shows that the interface pH is substantially deviated from the bulk pH and that it changes largely depending on the head group of the lipids.

References

- (1) Mondal, J. A.; Nihonyanagi, S.; Yamaguchi, S.; Tahara, T. *J. Am. Chem. Soc.* **2012**, *134*, 7842.
- (2) Kundu, A.; Yamaguchi, S.; Tahara, T. *J. Phys. Chem. Lett.* **2014**, 762.
- (3) Yamaguchi, S.; Kundu, A.; Sen, P.; Tahara, T. *J. Chem. Phys.* **2012**, *137*, 151101.

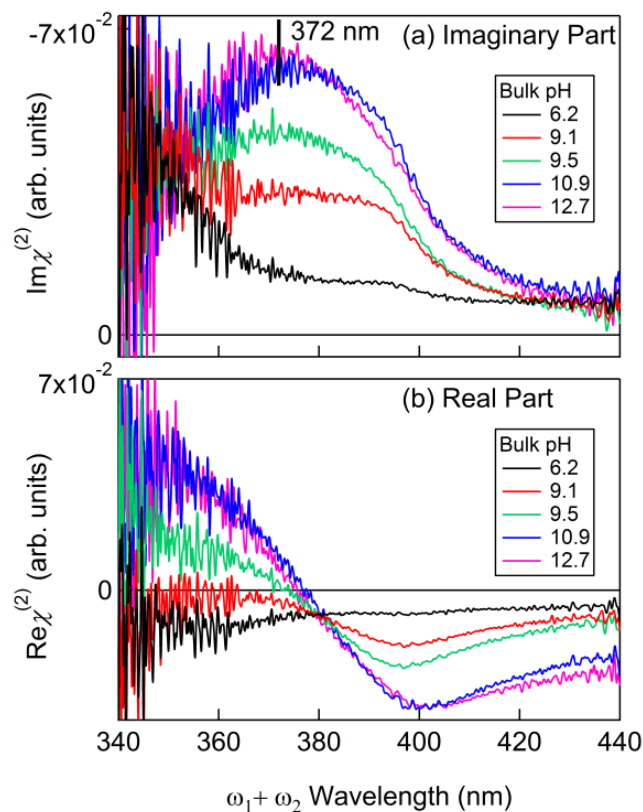


Fig. 3 (a) Imaginary and (b) real parts of the $\chi^{(2)}$ spectra of the pH indicator at the DPG/water interface. Black, red, green, blue, and pink lines represent spectra obtained at bulk pH 6.2, 9.1, 9.5, 10.9, and 12.7, respectively.

Water Structure at Nonionic Lipid/Water Interfaces Revealed by Heterodyne-Detected Vibrational Sum Frequency Generation Spectroscopy

Aniruddha Adhikari, Satoshi Nihonyanagi, Shoichi Yamaguchi, Tahei Tahara

Molecular Spectroscopy Laboratory, RIKEN

Despite its presence in nature and importance in many processes of biological relevance, our knowledge about lipid/water interfaces remains rather limited. This is chiefly due to difficulties in experimentally detecting such interfaces with sufficient molecular level sensitivity. Heterodyne-Detected Vibrational Sum Frequency Generation (HD-VSFG) is a novel nonlinear spectroscopic tool which allows us to overcome these difficulties and gain useful insights into lipid/water interfaces. The HD-VSFG experiment is capable of determining the complex second order nonlinear susceptibility ($\chi^{(2)}$) spectrum of a given interface. The imaginary part of $\chi^{(2)}$ ($\text{Im}\chi^{(2)}$) spectrum is an interface analogue of absorption spectrum in bulk hence it provides rich information about interfacial molecules. Furthermore, the sign of a resonance band in an $\text{Im}\chi^{(2)}$ spectrum provides a direct information about whether the interfacial molecule is oriented with its dipole pointing towards or away from the interface. Using HD-VSFG, we have previously studied interfaces between water and anionic, cationic and zwitterionic lipids and clarified the orientation and hydrogen-bond structure of water at these ionic lipid/water interfaces.^{1,2} In these ionic lipid interfaces, the overall orientation of interfacial water molecules was found to be governed by the charge or the local charge distribution present on headgroup moieties. In this work, we extend our HD-VSFG study of lipid/water interfaces and study the structure of water at a nonionic lipid/water interface.

Figure 1 shows the chemical structure of the nonionic lipids and amphiphiles chosen for investigation.

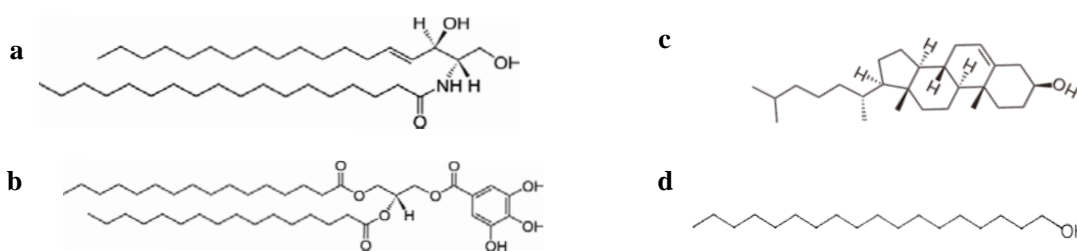


Figure 1. Chemical structures of a) C18-Ceramide; b) 1,2-dipalmitoyl-sn-glycero-3-galloyl; c) Cholesterol; d) Octadecanol

We used isotopically diluted water in our studies to minimize the effect of intra/intermolecular couplings in the $\text{Im}\chi^{(2)}$ spectra and thus allow a straightforward interpretation of the spectrum.

Figure 2 shows the $\text{Im}\chi^{(2)}$ spectra of water (HOD) surface covered by a monolayer of the lipid or amphiphile in the OH stretch region. The positive sign of the OH band indicates that the water at the interface of such nonionic species adopts net H-up orientation despite the absence of a charge on the lipid or amphiphile headgroup. The trend is observed to be common for all the four molecules studied despite substantial differences in chemical structure. Positive sign for the OH band was obtained in all the cases.

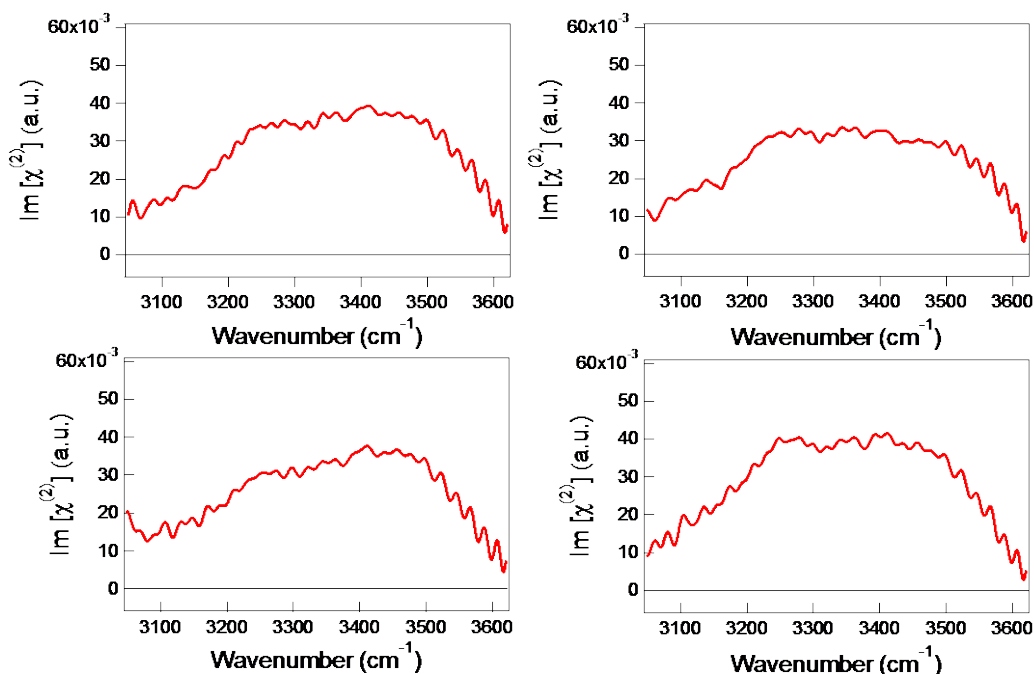


Figure 2. $\text{Im}\chi^{(2)}$ spectra of a) C18-Ceramide; b) 1,2-dipalmitoyl-sn-glycero-3-galloyl; c) Cholesterol; d) Octadecanol monolayers on 20% HOD-D₂O at air/water interface. All measurements in s-,s-,p- configuration.

All the molecules studied in this work bear headgroups that contain the hydroxyl functional group. The results in Figure 2 suggest that the hydroxyl oxygen in the headgroup is capable of behaving as an acceptor of hydrogen bond from the interfacial water molecules thus rendering their H atoms directed towards the headgroup's oxygen (thus favoring a net "H-up" orientation). It is concluded that the orientation and structure of interfacial water molecules in the vicinity of nonionic lipids is governed by scope of hydrogen bonding and is very different from that of zwitterionic lipids.

[References]

1. Mondal, J. A.; Nihonyanagi, S.; Yamaguchi, S.; Tahara, T. *J. Am. Chem. Soc.* **2010**, *132*, 10656.
2. Mondal, J. A.; Nihonyanagi, S.; Yamaguchi, S.; Tahara, T. *J. Am. Chem. Soc.* **2012**, *134*, 7842.

フェムト秒過渡吸収法による BLUFタンパク質のシグナル状態生成機構の研究

藤澤知績¹, 竹内佐年¹, 増田真二², 田原太平¹

理研・田原分子分光¹, 東工大・バイオ研究基盤支援総合セ²

BLUF(Blue Light sensing Using FAD)タンパク質はフラビン発色団FAD(flavin adenine dinucleotide)を持つバクテリアの青色光センサーの一種である。BLUFタンパク質内でFADが光を吸収すると、FADの光反応を経由してタンパク質に構造変化が起こり、その構造変化は光感知シグナルとして下流に伝わる。シグナル伝達が可能な状態(シグナル状態)では、光感知前の暗状態に対してFADの吸収スペクトルに約10nmのレッドシフトが観測されるのが特徴である。

BLUFタンパク質のシグナル状態にみられる吸収スペクトルのレッドシフトは、シグナル状態の生成がFAD自体の化学変化ではなく、FAD周りの水素結合の変化によって起こることを意味する。FADの近くにはグルタミン(Gln)とチロシン(Tyr)がどのBLUFタンパク質でも保存されており、これまでの研究からFAD-Gln-Tyr間の水素結合ネットワークの変化によってシグナル状態が生成することが分かってきた。しかし、FADの光反応によって水素結合が変化する仕組みも、その具体的な水素結合の構造も、諸説紛々として不明である。

昨年度、我々はBLUFタンパク質PapB(紅色細菌*Rhodospseudomonas palustris*由来)を対象としたフェムト秒過渡吸収測定を行い、PapBの暗状態からシグナル状態への状態変化はFADHラジカル(FADH•)を経由して起こることを示した。本年度は新たにPapBのシグナル状態の光反応を測定し、昨年度に得た暗状態の光反応と比較をした。一般にフラビン発色団の光反応は周囲の水素結合環境を反映して変化しやすい。そのため、シグナル状態と暗状態の光反応を比較することで、両者の間でFAD周りの水素結合状態の変化を検討し、シグナル状態の生成機構を考察した。

図1は450nmでPapBのシグナル状態を励起して得られる過渡吸収スペクトル(時間分解能:0.1ps)である。測定において、試料を非常に遅い速度でフローすることで励起体積内にシグナル状態を蓄積させてシグナル状態の過渡吸収スペクトルを得た。

光励起直後に現れるスペクトル(赤、0.7 ps)は第一励起状態(S₁状態)の生成に由来し、可視領域のブロードなS₁状態の吸収成分に加えて、暗状態のブリーチ(~450nm)とS₁状態からの誘導放出(~550nm)による負のバンドが観測される。S₁状態の減衰に伴って、600nm付近に反応中間体の生成による吸収成分(青、78 ps)が現れた後、最終的には新たな光生成物は生じず、ゼロ付近で平らなオフセット様のスペクトル(緑、693 ps)が残る。このことはシグナル状態を光励起した場合、S₁状態や反応中間体は元のシグナル状態に戻ることを意味している。

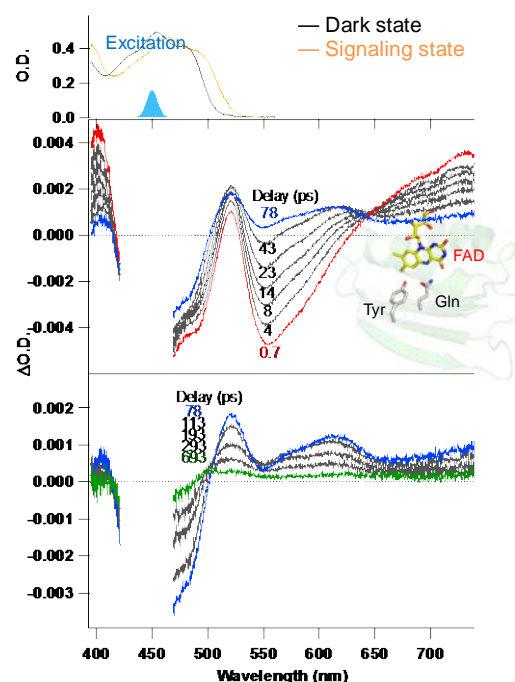


Figure 1. Absorption spectra of PapB and transient absorption spectra of the signaling state

図2は特異値分解を利用して行った遅延時間73psでのスペクトル分割の例である。図2の様に、どの遅延時間においても過渡吸収スペクトルは S_1 状態、反応中間体、および長寿命のオフセットの3つのスペクトル成分で構成することができ、得られたスペクトル形状から反応中間体は $FADH\cdot$ に同定された。このことは、PapBのシグナル状態を励起しても、暗状態の場合と同様に、FADにプロトン共役電子移動が起こることを意味する。

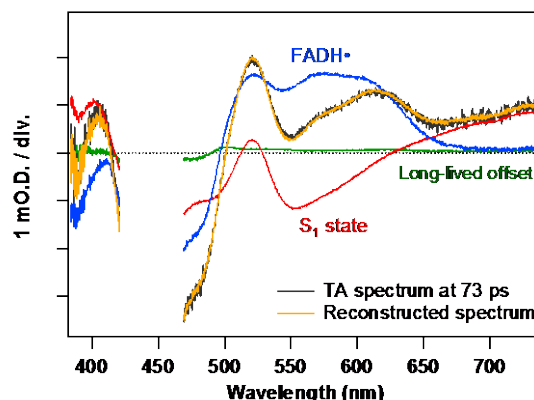


Figure 2. Decomposition of transient absorption spectrum

スペクトル分割から得られた S_1 状態と $FADH\cdot$ の時間プロファイルを図3Aに示す。 S_1 状態は2つの減衰成分を持ち、このうち早い減衰を示す S_1 状態から $FADH\cdot$ が生成することが分かる。フィッティング解析から得られる S_1 状態の寿命は24 ps (65%)と136 ps (35%)、 $FADH\cdot$ の寿命は135 psである。

今回得られたシグナル状態の光反応を昨年度に報告した暗状態の光反応と統一して図3Bに示した。暗状態とシグナル状態のどちらの光反応にも $FADH\cdot$ が観測される。その $FADH\cdot$ の生成・減衰にはフラビン結合部位のプロトン移動が関与するため、 $FADH\cdot$ のキネティクスはフラビン発色団まわりの水素結合構造を反映する観測量である。図3Aにおいて、 $FADH\cdot$ のキネティクスを暗状態とシグナル状態の間で比較すると両者は区別できないほど類似していることが分かった。

これまで、 $FADH\cdot$ が生成した後に発色団周りの水素結合ネットワークの変化が誘起されてBLUFタンパク質はシグナル状態になると提案されてきた[1]。この提案が正しい場合、 $FADH\cdot$ のキネティクスはシグナル状態生成に伴う発色団周りの水素結合変化によって変わるはずである。しかし、実際にはシグナル状態になっても $FADH\cdot$ のキネティクスには変化が見られない。そのためPapBの結果は、シグナル状態になるための水素結合の変化が $FADH\cdot$ の生成後に起こる従来の提案を支持していない。PapBの結果は $FADH\cdot$ の生成前（あるいは生成中）に水素結合変化が起こる新しいシグナル状態生成機構を示唆している。

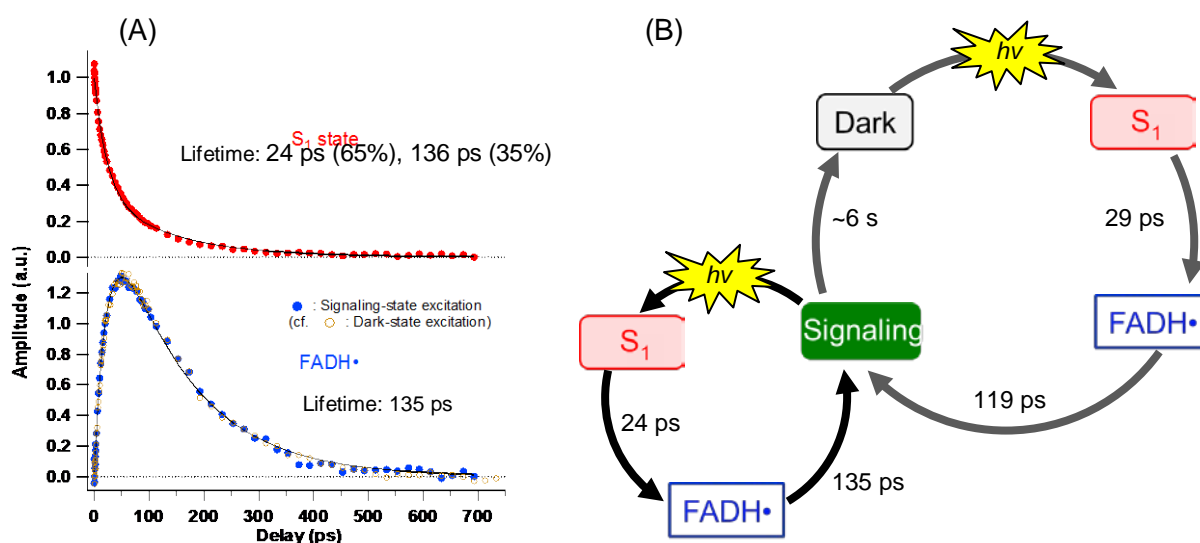


Figure 3. (A) Temporal profiles of S_1 state (●) and $FADH\cdot$ (●) obtained with signaling-state excitation and the fit curves (solid line). $FADH\cdot$ kinetics (○) obtained by dark-state excitation is plotted for comparison. (B) Illustration of combined photoreactions of the dark and signaling states of PapB.

[1] M. Gauden et al. *Proc. Natl. Acad. Sci. USA* **2006**, *103*, 10895.

アナバナセンサリーロドプシンのフェムト秒カーゲート蛍光分光

田原 進也^{1,2}, Wei Zhengrong¹, 竹内 佐年¹, 大谷 弘之², 田原 太平¹

理研・田原分子分光¹、東工大・生命理工²

【序】レチナール蛋白質は7回膜貫通型蛋白質であり、その内部に、リジン残基のアミノ基とプロトン化シッフ塩基結合したレチナール発色団を持つ。レチナール蛋白質はナノ秒から秒の時間領域で様々な生理機能を発揮するが、これらの生理機能は、フェムトからピコ秒の時間領域における発色団の光異性化によって発現する。この光異性化反応は完全に部位特異的に起こり、しかもその量子収率は0.6と高く、有機溶媒中の約3倍にも達する。このような蛋白質中における高い反応部位特異性と量子収率を実現するメカニズムは興味深い。

レチナール蛋白質の中でも古細菌型ロドプシンは、*all-trans*レチナールを有する*all-trans*体と、*13-cis*レチナールを有する*13-cis*体の混合物である。ところがBacteriorhodopsinのような従来の古細菌型ロドプシンにおいては、*13-cis*体から*all-trans*体への一方向のみの光変換が起こるため、明順応状態(光定常状態)において*all-trans*体がほぼ100%を占め、*13-cis*体はわずかしか存在しない。そのため、古細菌型ロドプシンにおいて、*all-trans*体の光反応過程や生理機能はよく理解されているが、*13-cis*体については光異性化とそれに続く光反応が起こることは知られているものの、その詳細は明らかにされていない。

ところが、近年発見された*Anabaena* sensory rhodopsin(ASR)では、*all-trans*体と*13-cis*体との間で光相互変換反応が起こり、明順応状態において60~80%の蛋白質が*13-cis*体として存在する(Fig. 1)[1]。したがってASRはこれまで困難であった*13-cis*体レチナール蛋白質の光反応の研究にとって最適な系といえる。

そこで、我々はフェムト秒時間分解カーゲート蛍光分光装置を構築し(Fig. 2)、それを用いてASRの超高速蛍光ダイナミクスを研究した。この種の時間分解測定で高繰り返し光源を用いた場合、寿命の長い光反応中間体が再度励起され、その結果、光反応中間体の蛍光が観測されてしまう可能性がある。そこで我々の測定では1 kHz励起光源と試料の循環装置を用い、再励起の問題を除いた。これにより、ASRの励起状態ダイナミクスを明らかにすることができたので、その詳細を以下にまとめる。

【実験】ASRを大腸菌に発現させ、*n*-dodecyl- β -D-maltosideによって可溶化後、Ni²⁺-NTAカラムにより精製した。試料の光学濃度ならびに体積はそれぞれ4 OD₅₅₀/cm, 50 mLであった。励起光の繰り返し、中心波長およびパルスエネルギーはそれぞれ1 kHz, 550 nm, 40 nJ/pulseであった。カー媒

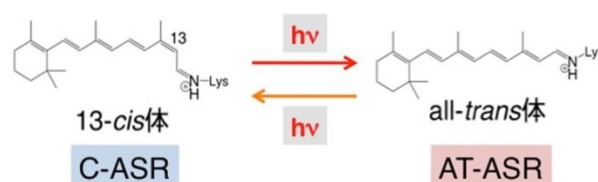


Figure 1. *Anabaena* sensory rhodopsin の発色団構造。

質にはブロモベンゼンを用いた。ゲート光は1100 nm, 15 $\mu\text{J}/\text{pulse}$ とした。装置応答関数の半値全幅は250 fsであった。

【結果および考察】

all-trans 体(AT-ASR)と 13-cis 体(C-ASR)の時間分解蛍光スペクトルを Figure 3 に示す。これらのスペクトルを波長 620 nm から 760 nm まで積分し、その強度を遅延時間に対してプロットした(Fig. 4)。

AT-ASR の時間トレースをフィッティング解析したところ、2 成分の指数関数の和でフィッティングすることができた。各成分の時定数はそれぞれ 700 fs および 1.8 ps であった。このことは、基底状態の AT-ASR が二種類存在するか、あるいは励起状態に 2 つの過渡種が存在するかのどちらかであることを示唆する。

一方で C-ASR の時間トレースは 1 成分の指数関数でフィッティングでき、その時定数は 250 fs であった。したがって C-ASR の S_1 状態の寿命は 250 fs であることがわかる。この励起状態寿命は、光異性化が起こる二重結合を軸としたねじれ運動の周期 200 fs と同程度である。このことは S_1 状態の C-ASR はねじれ運動を繰り返すことなく基底状態に緩和し、光生成物を与えることを意味する。すなわち C-ASR の S_1 ポテンシャル曲面は、反応座標に沿って無障壁であることが示唆される。

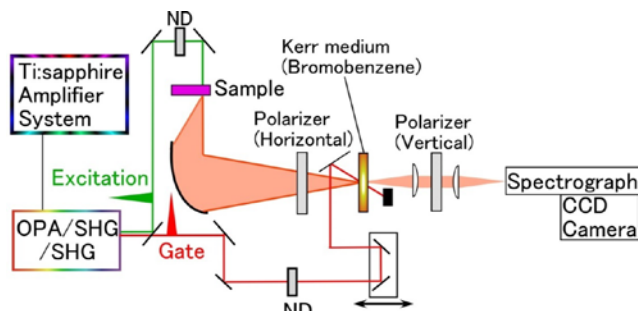


Figure 2. フェムト秒カーゲート蛍光分光装置。

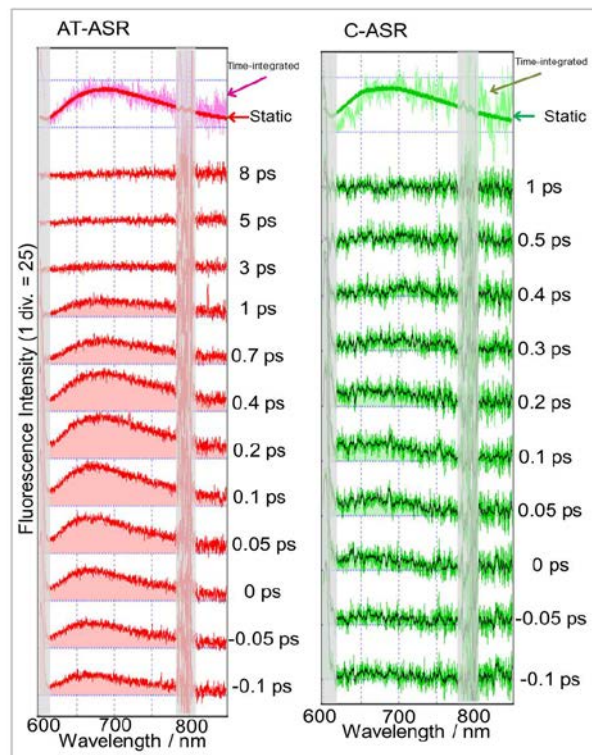


Figure 3. 時間分解蛍光スペクトル。

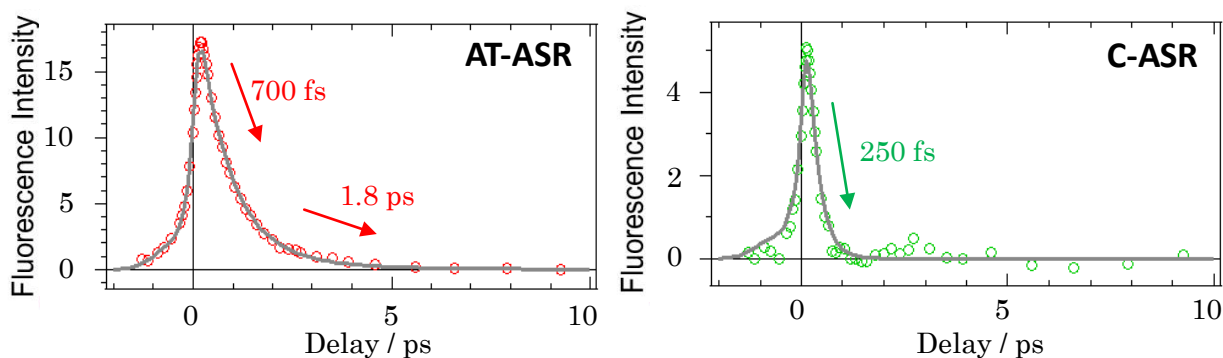


Figure 4. 蛍光強度時間トレース。

【参考文献】

[1] A. Kawanabe *et. al.* *J. Am. Chem. Soc.*, **2007**, 129, 8644-8649.

Substituent effect on the MLCT excited-state dynamics of Cu(I) complexes studied by femtosecond time-resolved absorption spectroscopy

Linqiang Hua, Munetaka Iwamura, Satoshi Takeuchi, Tahei Tahara

Molecular Spectroscopy Laboratory, RIKEN

Bis-diimine Cu(I) complexes have been attracting a great deal of attention from the viewpoints of both fundamental science and applications. The photophysical/photochemical properties of the Cu(I) complex are closely related to the flattening distortion occurring in the MLCT excited state, and are

significantly affected by substituents introduced at the 2-, and 9-positions of the ligands. Previously, we investigated the excited-state dynamics of three Cu(I) complexes with different substituents, $[\text{Cu}(\text{phen})_2]^+$, $[\text{Cu}(\text{dmphen})_2]^+$, and $[\text{Cu}(\text{dpphen})_2]^+$ (Figure 1), by femtosecond time-resolved emission spectroscopy, and revealed that the flattening distortion becomes slower for the complex having bulkier substituents [1]. However, the substituent effect on the ultrafast dynamics of the bis-diimine Cu(I) complexes has not yet fully clarified, because the femtosecond emission spectroscopy can detect only emissive states. In fact, the relaxation pathway of $[\text{Cu}(\text{phen})_2]^+$ has remained unsolved, since no emission was observed from transient states after the flattening distortion. Therefore, it is highly desirable to examine and compare the MLCT excited-state dynamics of the three Cu(I) complexes by complementary femtosecond time-resolved absorption spectroscopy for full understanding of the substituent effect. In this study [2], we carried out femtosecond time-resolved absorption measurements of the three Cu(I) complexes with the $S_1 \leftarrow S_0$ photoexcitation. Unlike the data reported so far, the direct $S_1 \leftarrow S_0$ excitation in our measurement made the observation simpler and interpretation straightforward. Furthermore, we also performed time-resolved absorption spectroscopy with 35-fs time resolution to observe the coherent nuclear dynamics in the MLCT states, which clarifies the vibrational dephasing in the initial excited state.

As shown in Figure 2, the transient absorption of $[\text{Cu}(\text{phen})_2]^+$ in dichloromethane exhibited a positive band at 570 nm due to the S_1 absorption immediately after the $S_1 \leftarrow S_0$ photoexcitation. The 570-nm band showed a slight intensity increase with a time constant of 0.2 ps, reflecting the flattening distortion in the S_1 state.

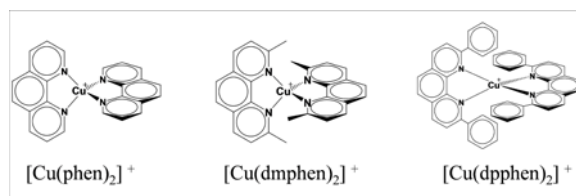


Figure 1. Molecular structures of three bis-phenanthroline Cu(I) complexes.

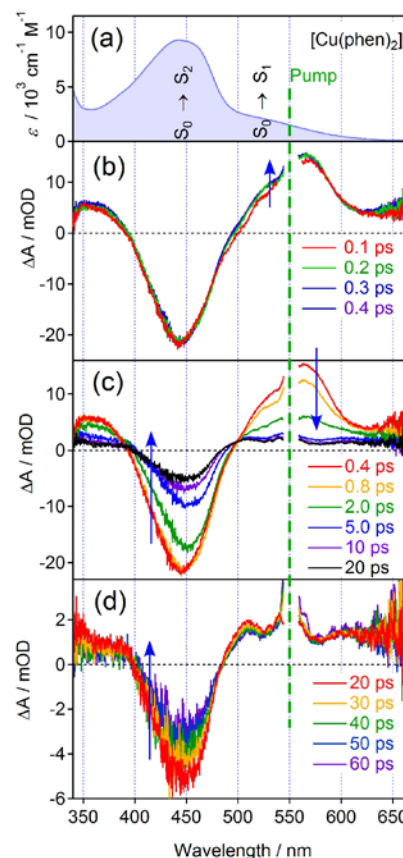


Figure 2. (a) Steady-state and (b-d) femtosecond time-resolved absorption spectra of $[\text{Cu}(\text{phen})_2]^+$ in dichloromethane (550 nm excitation, 2 mM).

The transient absorption of the flattened S_1 state was clearly observed, although its fluorescence was not observed in our previous femtosecond up-conversion measurement in the visible region. The transient absorption due to the flattened S_1 state decayed with a time constant of 1.8 ps, and the bleaching of the S_0 state recovered accordingly. This observation clarifies that the S_1 state of $[\text{Cu}(\text{phen})_2]^+$ is predominantly relaxed to the S_0 state by internal conversion. On the other hand, the transient absorption of $[\text{Cu}(\text{dpphen})_2]^+$ showed a 0.9-ps intensity increase of the S_1 absorption due to the flattening distortion, and then exhibited a 11-ps spectral change due to the intersystem crossing. This excited-state dynamics of $[\text{Cu}(\text{dpphen})_2]^+$ is very similar to that of $[\text{Cu}(\text{dmphen})_2]^+$. In the ultrafast pump-probe measurements with 35 fs time resolution, $[\text{Cu}(\text{phen})_2]^+$ and $[\text{Cu}(\text{dpphen})_2]^+$ exhibited oscillation due to the nuclear wavepacket motions of the initial S_1 state, as observed before for $[\text{Cu}(\text{dmphen})_2]^+$ (Figure 3). It was found that the dephasing time of the oscillation agrees well with the time constant of the flattening distortion in each complex. This result indicates that the initial S_1 states have well-defined vibrational structures and that the vibrational coherence is retained in their short lifetimes.

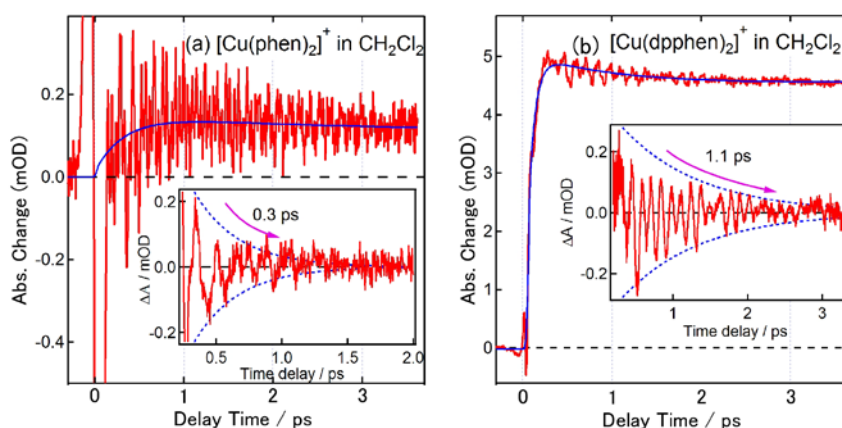


Figure 3. Pump-probe traces of (a) $[\text{Cu}(\text{phen})_2]^+$ and (b) $[\text{Cu}(\text{dpphen})_2]^+$ in dichloromethane (pump: 550 nm, probe: 1000 nm).

The obtained time-resolved data revealed that the relaxation scheme of $[\text{Cu}(\text{phen})_2]^+$ is significantly different from those of the other two complexes. We consider that the difference arises from different magnitudes of the structural change occurring in the S_1 state. Since $[\text{Cu}(\text{phen})_2]^+$ has no substituents, it can undergo a large structural change, becoming close to the square-planar structure. As a result, the S_0 and S_1 potential energy surfaces get energetically close at the flattened structure, which significantly accelerates the $S_1 \rightarrow S_0$ internal conversion over other competing relaxation pathways such as intersystem crossing to the T_1 state. In the other $[\text{Cu}(\text{dpphen})_2]^+$ and $[\text{Cu}(\text{dmphen})_2]^+$, such an extensive flattening distortion is prohibited by the steric hindrance due to the substituents at the 2- and 9-positions of the ligands. Thus, the internal conversion rate is much smaller than the rate of intersystem crossing, so that the flattened S_1 state relaxes predominantly to the T_1 state. The present study accounts for the difference in the relaxation pathways of the three Cu(I) complexes depending on the substituents, and provides a unified view for the substituent effect on the ultrafast dynamics of the MLCT excited state.

[1] M. Iwamura, S. Takeuchi, T. Tahara, *Phys. Chem. Chem. Phys.* 16, 4143 (2014).

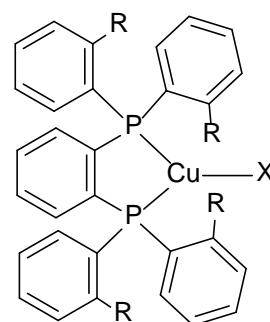
[2] L. Hua, M. Iwamura, S. Takeuchi, T. Tahara, *Phys. Chem. Chem. Phys.* 17, 2067 (2015).

熱励起型遅延蛍光性三配位銅錯体の構造と光特性

大澤 正久, 田原太平

理研・田原分子分光

イリジウム (Ir) を中心金属とする重金属錯体が有機エレクトロルミネッセンス (EL) の燐光型発光材料として報告され、蛍光型発光材料に対する優位性が認められている。しかしながら、これらの高効率燐光材料の多くは希土類及び貴金属を含むものに限られておりコスト面で問題があった。我々は次世代燐光材料として、安価でかつ豊富な埋蔵量が見込まれる銅 (Cu) に注目し発光材料の開発を行ってきた。図 1 に示すような三配位強発光性銅一価錯体を使用したプロトタイプデバイスを製作し、実用レベルの外部量子収率を達成した[1]。この材料の特徴は、ビスホスフィン配位子の二つのリン配位原子にリンクしたアリール基のオルト位に導入した置換基 (R) にある。この置換基が 4 つめの配位座をブロックすることで、特異な三配位構造を安定化している。また励起状態の計算から、この錯体の発光遷移は $(\sigma+X) \rightarrow \pi^*$ に基づくこと、及び一重項励起状態と三重項励起状態のエネルギー差が極めて小さいことが判明した。前者は、多くの四面体型銅錯体に見られる金属 \rightarrow 配位子 (MLCT) タイプの遷移とは異なることを示している。



R = Me; X = Cl(1), Br (2) and I(3)
R = Et; X = Br(4)
R = iPr; X = Br(5)

図 1. 三配位銅錯体の構造。

最高被占軌道(HOMO) が金属の軌道だけでなくリン配位子の軌道も含まれていること、また X (ハロゲン配位子) $\rightarrow \pi^*$ (配位子) つまり LLCT 的な遷移も併せ持つことを示唆しており、そのため錯体の発光特性が配位子の性質に大きく依存することになる。後者はこの発光が熱励起型遅延蛍光であることを意味している。励起一重項状態と三重項状態のエネルギー差が極めて小さいと室温付近で両者は熱平衡に達する。励起三重項状態から熱励起され励起一重項状態になり、この状態からの発光が遅延蛍光となる。この場合も原理的にはイリジウムのリン光材料と同等の 100% の内部量子収率が期待できる。今回、二座ホスフィン配位子を含めた三配位錯体の発光特性の詳細を検討した。

ビスホスフィン配位子は溶液状態では、ごく弱い発光しか示さないが固体状態では緑色に発光する。図 2 にビスホスフィン配位子の吸収・発光スペクトルを示した。アリールホスフィンに特徴的な大きなストークスシフト ($\sim 14,000 \text{ cm}^{-1}$) が観測された。このことは、配位子の発光がリン原子上のローンペアから配位子の π^* への CT 的遷移に基づくことを示唆しており、ストークスシフトは励起状態でのリン原子回りの構造変化 (平面化) によって説明される。また

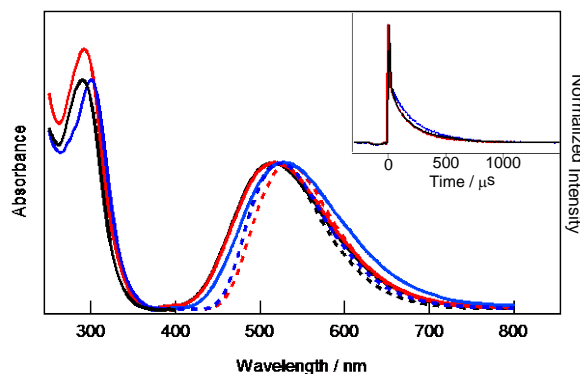


図 2. 配位子の吸収・発光スペクトル (固体状態)
R = Me (黒), Et (赤), and iPr (青)、室温は実線、77Kは破線。
右上には発光寿命測定のプロファイルを示した。

置換基の電子供与能が増してもそのスペクトルの差はわずかなものであった。サイクリックボルタンメトリーの測定から配位子の酸化電位はハメット則に従い低下していることが判明し、この事実から置換基の電子的効果は HOMO だけでなく LUMO にも作用していることがわかる。そのため結果としてバンドギャップはほとんど変化しなかったと理解できる。

発光寿命の測定において短い成分 (< 20 ns) と長い成分 (~ 200 μs) が同時に観測されたこと (図 2、右上)、77 K においては 10 ms を超える長寿命となり、発光極大が長波長化し、量子収率も大きく上昇すること、以上の事実は室温での長寿命成分が熱励起型遅延蛍光であることを強く示唆している。77 K における長寿命化と発光極大の長波長化は発光が遅延蛍光 (室温) から燐光へと変化したと説明できる。

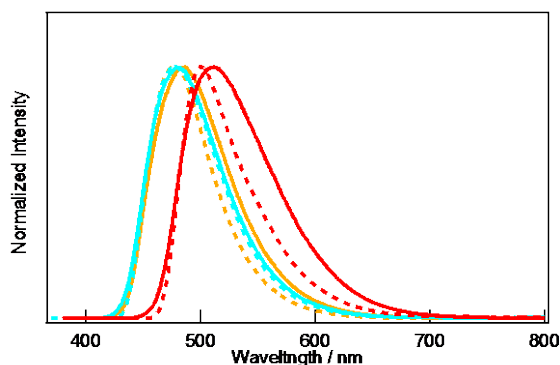


図 3. 錯体 **2**(赤)、**4**(オレンジ)、**5**(水色)の発光スペクトル(固体状態)。実線は室温、破線は 77 K。

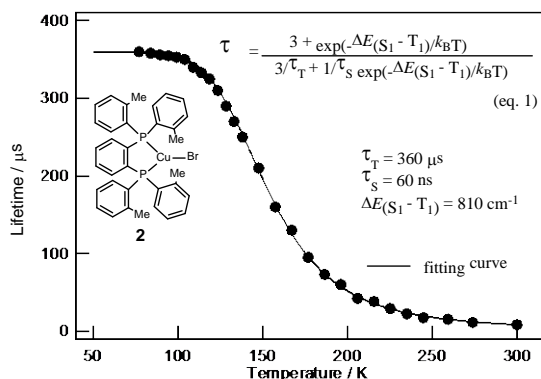


図 4. 錯体 **2** の発光寿命の温度依存性。図中のフィッティング曲線は eq. 1 によるもの。

図 3 に錯体 **2**、**4**、**5** の発光スペクトルを示す。室温から 77 K へと変化させると錯体 **2** の半値幅はかなり減少し、非発光プロセスの原因となる励起状態での構造変化が抑制されていることがわかる。一方、錯体 **4**、**5** においてはほとんど変化しないことから置換基が大きくなると室温においても十分構造変化が抑制できることを示唆している。実際、室温での発光量子収率は $2 < 4 < 5$ の順であった。また室温で数 μs であった発光寿命は 77 K では数百倍と長寿命化し、発光量子収率も向上していることから室温の発光が遅延蛍光であることが示唆された。図 4 に錯体 **2** の発光寿命の温度依存性の測定結果を示した。これらの測定値を eq. 1 によってフィッティングすることで一重項励起状態と三重項励起状態間のエネルギー差 $\Delta E(S_1-T_1)$ を求めることができる。τ として 100 K 以下でほぼ一定になった 360 μs を使用し、最小二乗法によって $\Delta E(S_1-T_1) = 810 \text{ cm}^{-1}$ と決定された。同様に測定を行ったところいずれの錯体においてもエネルギー差は 1000 cm^{-1} 以下となり遅延蛍光性が支持された[2]。つまり、これら三配位型銅錯体の強発光性は遅延蛍光によるものと結論できる。また今回の結果はこの錯体の発光特性が配位子の遅延蛍光性に由来していることを明らかにするとともに [3]、錯体の発光色をチューニングするためには配位子の分子設計が鍵となることを示している。

【参考文献】

- [1] Hashimoto, M.; Igawa, S.; Yashima, M.; Kawata, I.; Hoshino, M.; Osawa, M. *J. Am. Chem. Soc.* **2011**, *133*, 10318. [2] Osawa, M. *Chem. Commun.* **2014**, *50*, 1801. [3] Osawa, M.; et al. *Dalton. Trans.* **2015**, in press.

スフィンゴミエリン脂質二重膜のアミドバンドに対する理論的解析

八木清¹, Pai-Chi Li¹, 城田幸一郎², 小林俊秀², 杉田有治¹

理研・杉田理論分子科学¹, 理研・小林脂質生物学²

【背景】生体膜には、機能を持った膜タンパク質や糖鎖などが集積した分子群が細胞内外の物質輸送に重要な役割を果たしており、脂質膜に浮かぶ筏という意味で「ラフト」と呼ばれている。しかし、ラフト構造は極めて動的であり、生体膜中にどのように存在しているのか、その描像を明らかにする計測手法は限られており、従って、その存在も含め、未だ多くの論争が続いている[1]。スフィンゴミエリン (SM) はラフトを構成する主要な脂質分子の一つであり、図1のようにheadとtail groupをつなぐ中間部位に、スフィンゴシン由来のアミド骨格とOH基を持つ。これらの極性基が水素結合したSMクラスターがラフト生成に関わっていると考えられるが、生体膜におけるクラスターの動態は未だに明らかでない。

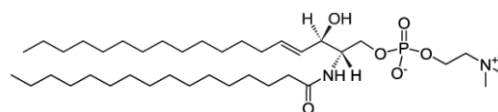


図 1. SM の化学式

最近、城田と小林は、ラマン分光法によりSMリポソームの振動スペクトルを取得し、SMのアミドI (C=O伸縮振動)と思われる強いピークを1645 cm^{-1} に観測した。興味深いことに、この振動バンドはSM/DOPC混合膜にも観測されるが、SM/DPPC混合膜では消失する。SMはDOPCでは分散しないが、DPPCでは分散することが知られており[2]、従って、この振動バンドはSMクラスターの生成を示すマーカバンドとなることが示唆された。しかし、過去の文献では、この領域に弱いバンドしか観測されておらず、その強度の弱さから水の変角振動と考えられていた。

本研究では、観測されたラマンバンドの帰属を明らかにするため、分子動力学法 (MD) と量子化学計算によりSM二重膜のラマンバンドを計算した。

【SM二重膜に対するMD計算】Venableら[3]により開発されたSM用の古典力場を用いてSM二重膜に対するMD計算を実施した。ユニットセルに128個のSM分子と5012個の水分子を含む系を用意し、温度・圧力一定のMD計算を100 ns実行した。圧力は1 atm, 温度は23°Cと50°Cの2つで計算した。プログラムはNAMDを用いた。

図2にMD計算により得られたSM二重膜の構造を示す。SM二重膜は転移温度が38°C付近にあり、23°Cではゲル相、50°Cでは液晶相となる。図2から、50°Cの結果はtailグループが乱雑になっているのに対し、23°Cの結果はtailグループが綺麗に配列しており、相が異なっていることが明らかである。また、液晶相ではゲル相よりも膜内部に多くの水分子が入っていることが分かった。液晶相とゲル相では、1個のSM分子当たり平均して水分子は3.9個と2.1個だった。

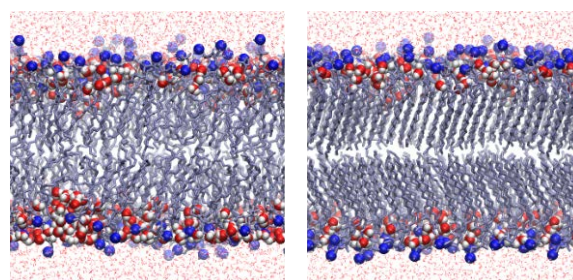


図 2. MD 計算で得られた SM 二重膜の構造。温度が 50°C (左) と 23°C (右) ではそれぞれ液晶相、ゲル相となる。コリンの窒素 (青) の平均位置より内側に入っている水分子がハイライトされている。

得られたトラジェクトリーに対して、アミド基の水素結合ネットワークの解析を行った。その結果、アミド基は、液晶相ではほとんど単独で存在するのに対し、ゲル相では2量体が主と

なることが分かった。これは、液晶相では、水分子が膜内部に多く入り込むため、アミド基と水の水素結合が構築され、アミド基同士の水素結合が妨げられるためである。

【SMクラスターに対する量子化学計算】図3に示すSMのモデル分子を用いて、トラジェクトリーからSMクラスターを取り出し、量子化学計算により構造最適化とラマンスペクトルの計算を行った。図3のモデル分子に対し、4次の非調和性まで考慮したポテンシャルを生成し、VMP2法により振動数を求めた。得られた調和と非調和振動数の比により得られる非調和補正係数を用いて、SMクラスターの調和振動数を補正した。計算レベルにはB3LYP/6-31++G(d,p)、プログラムはGaussian09を用いた。得られたスペクトルをSMクラスターに対する重み平均を取ることで、全スペクトルを計算した。

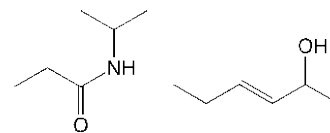


図3. 量子化学計算に用いたSMのモデル分子。

計算されたスペクトルを、実験結果とともに図4に示す。液晶相とゲル相の結果を比較すると、ゲル相の方がアミド基の2量体が増えることを反映し、赤線で示す2量体のアミドIバンドが低波数側に広がっているのが分かる。ゲル相の計算結果は、リポソームを溶液から取り出してから1時間後の実験結果（実線）とよく一致する。実験では、このスペクトルは時間とともに変化し、48時間後に定常化する。そのスペクトル（点線）には、 1645 cm^{-1} に明瞭なピークがあり、 1665 cm^{-1} 付近に肩バンドがある。リポソームが試料台に置かれている間の変化は、リポソームが乾燥し、SM二重膜から水分が失われた時の変化に相当する。従って、 1645 cm^{-1} のピークは、水を失うことで、2量体（あるいはさらに大きい多量体）が生成したことを示唆している。一方、水素結合ネットワークから孤立した単量体は、水分量の変化に影響を受けずに残るため、 1665 cm^{-1} のピークは相対的に突出してくると考えられる。

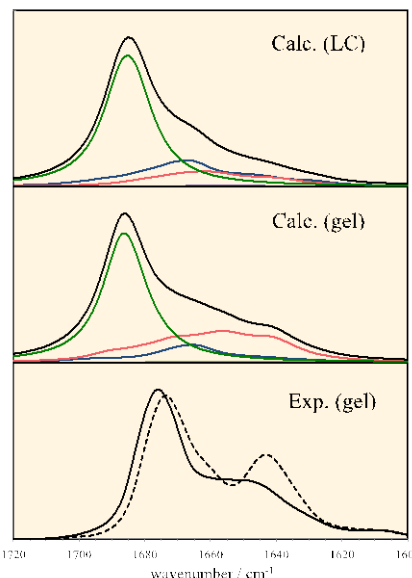


図4. SM二重膜のラマンスペクトル。計算による液晶相（上）とゲル相（中）のスペクトル。緑線はCC伸縮振動、赤線と青線は、それぞれ、単量体と二量体のアミドIバンド。（下）実験スペクトル。実線と点線は、それぞれ、リポソームを溶液から資料台へ取り出してから1時間と48時間後のスペクトル。

【まとめ】本研究では、SM二重膜に対するMD計算と量子化学計算を実施し、アミドバンドのラマンスペクトルを計算した。計算結果は実験スペクトルを良好に再現し、帰属が不明確であった 1645 cm^{-1} のピークはアミドIバンドであることを決定できた。

振動分光実験と理論計算を組み合わせることで、動的に複雑な構造を持つ分子系の解析技術を確立し、柔らかな構造を持つ分子系の動的構造を明らかにすることができた。

【参考文献】

1. 鈴木健一, 楠見明弘, 生物物理 **53**, 295 (2013).
2. P. R. Maulik, G. G. Shipley, Biophys. J. **70**, 2256 (1996); C. Yuan, J. Furlong, P. Burgos, L. J. Johnston, Biophys. J. **82**, 2526 (2002).
3. R. M. Venable et al., Biophys. J. **107**, 134 (2014).

を解明するためのシミュレーション研究に広く使える可能性を示している。今後の研究課題としては、ATP分子に結合する Mg^{2+} などの2価イオンとATPおよびタンパク質の相互作用を正しく見積もることである。

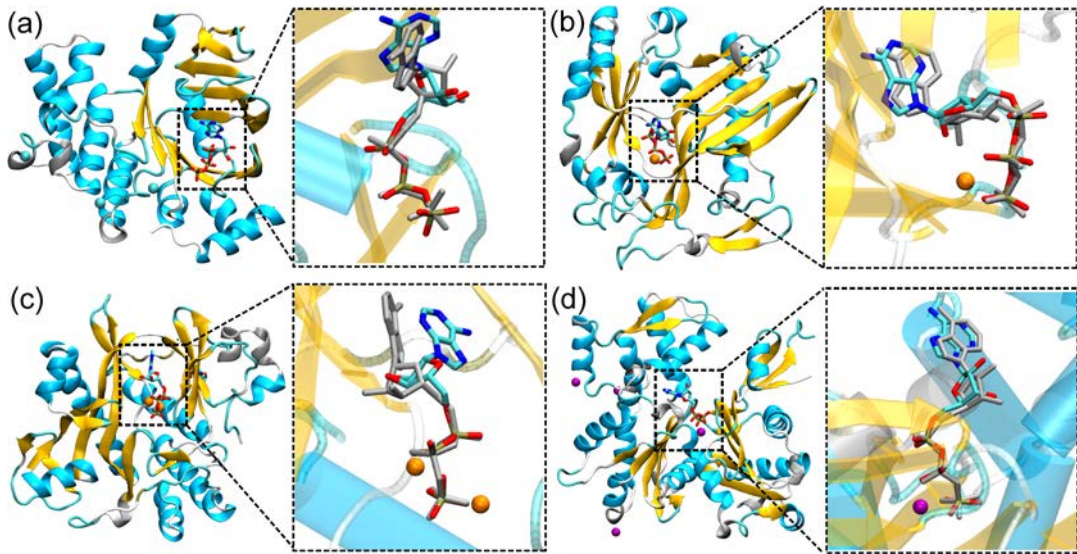


図2. 4つのATP結合タンパク質の分子動力学計算前後のATP分子の構造変化

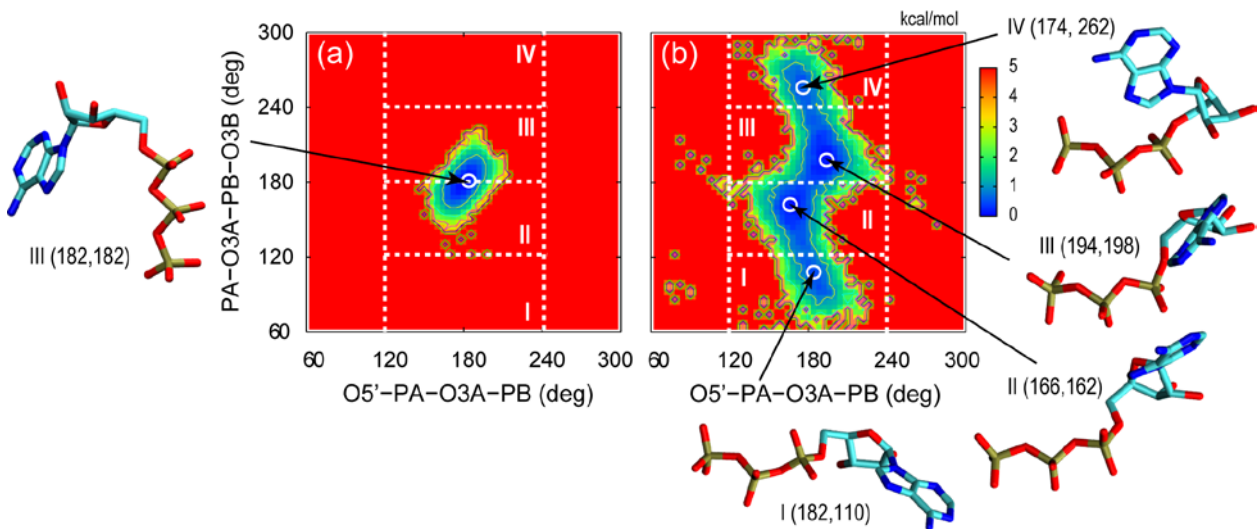


図3. (a) C27、(b) mod-C27を用いた水溶液中のATP分子の自由エネルギーランドスケープ

【参考文献】

Y. Komuro, S. Re, C. Kobayashi, E. Muneyuki and Y. Sugita: “CHARMM Force-Fields with Modified Polyphosphate Parameters Allow Stable Simulation of the ATP-bound Structure of Ca^{2+} -ATPase”, *J. Chem. Theory. Comput.* **10**, 4133-4142 (2014).

Direct observation of adsorption geometry for the van der Waals adsorption of a single π -conjugated hydrocarbon molecule on Au(111)

Ju-Hyung Kim,^{1,2} Jaehoon Jung,² Kazukuni Tahara,³ Yoshito Tobe,³ Yousoo Kim,² and Maki Kawai¹

¹Department of Advanced Materials Science, The University of Tokyo

²Surface and Interface Science Laboratory, RIKEN

Understanding the interfacial interaction between π -conjugated hydrocarbon (π -CHC) molecules and metal surfaces is of great importance not only in the field of fundamental surface science but also other application areas such as organic electronics [1-4]. Indeed, π -CHC molecules and gold (Au) as an electrode are receiving much attention as promising materials due to high charge-carrier mobility and a low hole-injection barrier, respectively. Extensive efforts, therefore, have been devoted to study the interfacial interaction with various π -CHC molecules, such as benzene, pentacene, perylene, and coronene, on the noble Au(111) surface which is the most chemically inert and most densely packed facet of Au. Photoemission studies have observed their weak van der Waals (vdW) adsorption characters, where the molecular π -states are preserved and accompanied with molecular level broadening, and have suggested that the pillow effect (i.e., electron density polarization at the interface) mainly contributes to the formation of interface dipole [3,4]. Nevertheless, the detailed interfacial electronic structures and precise adsorption geometries at the atomic scale have not yet been clarified for the vdW adsorption process of a π -CHC molecule onto the noble metal surface. It is because a vdW potential minimum of the process has been considered too shallow to determine a specific adsorption configuration of a π -CHC molecule on the noble metal surface.

Single-molecule studies using scanning tunneling microscopy/spectroscopy (STM/STS) have contributed to revealing interfacial electronic and geometric structures at organic-metal contacts in detail. However, in the case of the vdW adsorption of a single π -CHC molecule on Au(111), only few STM/STS studies have been reported, and the correlation between adsorption geometry and interfacial electronic structures has still been veiled due to the weak adsorption characters. As a representative example, although Soe et al. successfully observed the interfacial electronic structures of the single pentacene molecule on a relatively reactive elbow site of herringbone reconstructed Au(111), a precise adsorption configuration could not be discussed due to an undefined local surface structure at the elbow site [5].

In this work, we provide a first direct observation of adsorption geometry of a well-designed π -CHC molecule, i.e., dehydrobenzo[12]annulene (DBA), on Au(111) using an atomically-resolved STM study combined with vdW density functional (vdW-DF) methodology. Our observations on an atomically-resolved scale clearly indicate that the DBA molecule has only one adsorption configuration on Au(111) (see Fig. 1(a) and (b)), even though the weak vdW adsorption characteristics of DBA/Au(111) were examined by means of STS and vdW-DF calculations. Based on the precisely determined adsorption geometry of DBA/Au(111), the

vdW-DF calculation results imply that even a very small contribution of the orbital interaction at the organic-metal interface can constrain adsorption structure even for the weak vdW adsorption (see Fig. 1(c)). The importance of orbital interaction involved in the adsorption of a π -CHC molecule on Au(111) emerges as a clear correlation between the relative stabilities of local minimum structures and their order of density of states (DOS) broadening, which results from the weak electronic coupling of the molecular π -state with the Au d state.

In conclusion, our combined study using STM/STS and vdW-DF calculations provides a comprehensive description of the interfacial geometric and electronic structures of the π -CHC molecule adsorbed on the noble Au surface at the single-molecule level, specifically selecting the well-designed system of DBA/Au(111) for this purpose. Our observations of the weak vdW adsorption system clearly indicate that a π -CHC molecule can have a specific adsorption configuration, even on the noble Au surface. Based on the precisely determined adsorption geometry of DBA/Au(111), the vdW-DF calculations provide improved knowledge of orbital interactions at the interface between a π -CHC molecule and the Au(111) surface. Such interfacial orbital interaction originates from the weak electronic coupling between the molecular π -state and the electronic states of the Au surface, which can play a decisive role in constraining adsorption geometry even in the archetypal vdW adsorption system. Our study provides not only deeper insight into the formation of interfacial electronic structures at organic-metal contacts beyond the vdW scheme, but also new perspectives to organic electronics using π -CHC molecules on the Au surface.

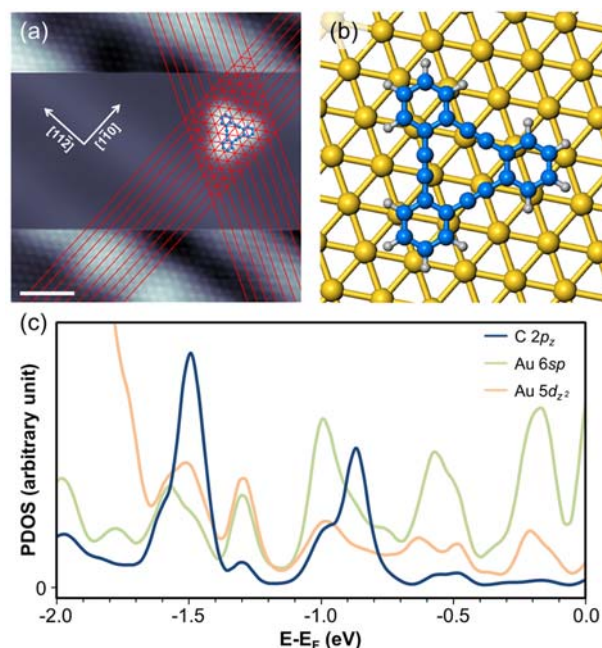


Figure 1. (a) STM image of isolated DBA molecule on Au(111) obtained by spatially varying the tunneling conditions (top and bottom: $V_s = -2$ mV, $I_t = 9.0$ nA, Scale bar (S) = 1.5 nm; middle: $V_s = -500$ mV, $I_t = 0.4$ nA). (b) Optimized structure of DBA/Au(111) by vdW-DF calculation (C, blue; H, grey; Au, yellow). (c) PDOS diagrams for the occupied π -states (C $2p_z$), the HOMO and the doubly degenerated HOMO-1 states, of DBA/Au(111), with the $5d_{z^2}$ and $6sp$ states of Au(111).

[Reference]

1. S. R. Forrest, *Chem. Rev.* **97**, 1793 (1997).
2. M. Eremtchenko, J. A. Schaefer, and F. S. Tautz, *Nature* **425**, 602 (2003).
3. H. Ishii, K. Sugiyama, E. Ito, and K. Seki, *Adv. Mater.* **11**, 605 (1999).
4. A. Kahn, N. Koch, and W. Gao, *J. Polym. Sci. Part B: Polym. Phys.* **41**, 2529 (2003).
5. W.-H. Soe, C. Manzano, A. De Sarkar, N. Chandrasekhar, and C. Joachim, *Phys. Rev. Lett.* **102**, 176102 (2009).

* This work has been published in *J. Chem. Phys.* **140**, 074709 (2014)

Functionalization of Graphene Grown on Metal Substrate with Atomic Oxygen: Enolate vs. Epoxide

Jaehoon Jung, Hyunseob Lim, Junepyo Oh, and Yousoo Kim

Surface and Interface Science Laboratory, RIKEN

Functionalization of graphene has attracted great scientific interest not only in controlling the physical properties of graphene, such as opening band gap to achieve semiconducting nature, but also in improving chemical adaptability to integrate graphene as a building block into a variety of functional devices. Due to the great simplicity of atomic species, atomic functionalization on the basal plane of graphene with covalent bonds has been considered one of the promising ways to maximize the utilizability of graphene [1], in which hydrogen, fluorine and oxygen have been extensively studied as a key species in order to induce symmetry breaking of graphene composed of sp^2 hybridized carbons. In particular, atomic oxidation allows compositional expandability through additional chemical reactions. At the limit of low coverage, whereas hydrogen or fluorine makes a single covalent bond with carbon atom, i.e., ontop configuration, on the basal plane of a graphene sheet, the attachment of atomic oxygen to graphene results in graphene epoxide, i.e., bridge configuration, in which an oxygen atom covalently interacts with two adjacent carbon atoms. Other possibility except epoxy group on the basal plane of graphene has been excluded, and thus it leads to the narrow choice of a chemical route not only for further functionalization but also for the development of graphene-based catalysts.

Recently, using periodic density functional theory (DFT) calculations, we first suggested that the atomic oxidation of graphene grown on a metal substrate results in the formation of graphene enolate, i.e., negatively charged oxygen adsorbed at ontop position on its basal plane, which is strikingly different from the formation of epoxy groups on free-standing graphene and on graphite [2]. Whereas the enolate is the transition state between two nearest epoxides on graphene and on graphite, we revealed that the enolate group forms on epitaxial graphene on a metal substrate exists as a local minimum, and further becomes more stable than the epoxide.

Figure 1 shows the (4×4) supercell structures employed in this study. Whereas free-standing graphene has only one type of ontop site for the atomic oxidation on its basal plane (Figure 1a), there are two different ontop configurations (OT1 and OT2, red and yellow dots, respectively), i.e., corresponding to the formation of graphene enolate, on graphite (Figure 1b) and Gr/Cu(111) (Figure 1c). The C atoms adjacent to the oxidized C atom locate on ontop and hollow sites of underneath graphite or metal layers for OT1

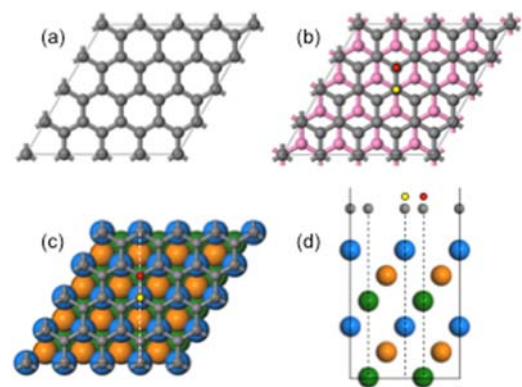


Figure 1. Simulated (4×4) supercell structures for (a) free-standing graphene, (b) graphite, and (c, d) graphene grown on Cu(111) substrate. Red and yellow dots indicate two different ontop configurations, OT1 and OT2, respectively, for atomic O adsorbate.

and OT2, respectively. Bridge configurations (BR), i.e., corresponding to the formation of graphene epoxide, are all identical in each system.

We examined the detailed potential energy surface for the migration of O adsorbate between the ontop and bridge sites on the graphene sheet. Figure 2 obviously shows the existence of OT1 (and OT2) as a local minimum on the Gr/Cu(111). Whereas the formation of BR is most favorable on both graphene and graphite compared with the adsorption at ontop sites (by ~ 0.9 eV), the adsorption site preference dramatically changes on the epitaxial graphene grown on Cu(111) substrates. On Gr/Cu(111), OT1 becomes more stable than BR by 0.10 eV, although OT2 is still less favorable than BR by 0.07 eV. These results imply that the interfacial interaction between graphene and metal substrate is crucial in accounting for the stability of O adsorbate.

Figure 3 shows the band diagrams of bare and OT1 Gr/Cu(111), and corresponding partial charge density plots at **K**-point. Figure 3c,d shows the partial charge density for degenerated electronic states at Dirac conical point, which indicates that the C 2p states of graphene are isolated from the electronic states of Cu(111). However, Figure 3f,g clearly shows that the 2p states of C atoms strongly interact with 3d states of underlying Cu atoms at the interface.

To summarize, our computational results strongly suggest that the atomic oxidation of graphene grown on metal substrate can provide an opportunity to extend graphene chemistry with the newly suggested functional group, i.e., enolate, on the basal plane of graphene. The interfacial interaction between graphene and metal substrate plays a crucial role not only in the formation of enolate as a local minimum but also in stabilizing it over the epoxide. Our computational study is expected to trigger experimental attempts to find the existence of graphene enolate on metal substrates and to design new chemical pathways utilizing it.

[Reference]

1. J. E. Johns and M. C. Hersam, *Acc. Chem. Res.* **46**, 77 (2013).
2. J. Jung, H. Lim, J. Oh, and Y. Kim, *J. Am. Chem. Soc.* **136**, 8528 (2014).

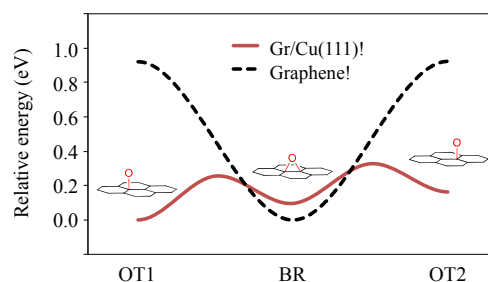


Figure 2. Potential energy surfaces for the oxygen migration between ontop (enolate) and bridge (epoxide) sites on free-standing graphene and Gr/Cu(111). The relative energy was used in constructing a potential energy surface

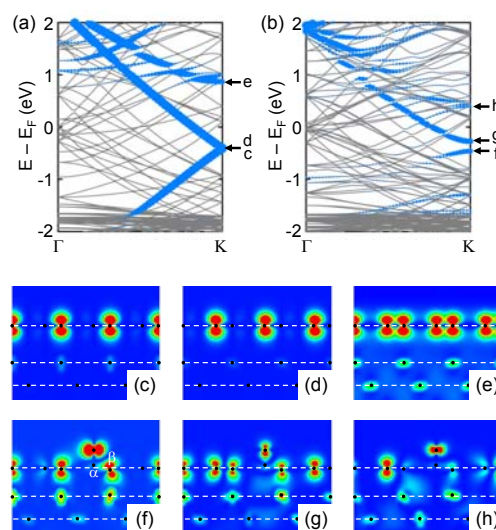


Figure 3. Band diagrams of (a) bare and (b) OT1 Gr/Cu(111). (c-h) The partial charge density plots for selected electronic states at **K**, for which energies are marked by black arrows in (a) and (b).

A New Sulfur-Metal Complex on Cu(111)

Holly Walen,^a Da-Jiang Liu,^b Junepyo Oh,^c Hyunseob Lim,^{c,†} J. W. Evans,^{b,d} Christine Aikens,^e
Yousoo Kim,^c and P. A. Thiel^{a,b,f}

^aDepartment of Chemistry, Iowa State University, Ames, Iowa 50011 USA

^bAmes Laboratory of the USDOE, Ames, Iowa 50011 USA

^cRIKEN Surface and Interface Science Laboratory, Wako, Saitama 351-0198, Japan

^dDepartment of Physics & Astronomy, Iowa State University, Ames, Iowa 50011 USA

^eKansas State University, Department of Chemistry, Manhattan, Kansas 66506 USA

^fDepartment of Materials Science & Engineering, Iowa State University, Ames, Iowa 50011 USA

It has been proposed that metal-adsorbate complexes can greatly accelerate rearrangements of metal nanostructures and surfaces. This issue is of importance for stability of catalysts or nanostructures, and has been the subject of prolonged speculation given that the complexity of such systems typically precludes definitive analysis.¹ Nonetheless, evidence continues to accumulate supporting the presence of mobile complexes on surfaces and, by implication, their role in metal transport. Adsorbates that form mobile surface complexes with metals include hydrogen, oxygen, alkylsulfides, and—the subject of this study—sulfur. The soft metals Cu, Ag, and Au, which are of great interest because of their catalytic and plasmonic properties, are expected to be particularly susceptible to this effect.

We studied a S-Cu complex which we later identified as Cu_2S_3 on the Cu(111) surface using scanning tunneling microscopy (STM). Experiments were performed with a low-temperature STM (Omicron) under ultrahigh vacuum. Sulfur was exposed to the surface from an electrochemical source, where S_2 is the dominant species, while the sample was held at room temperature. The sample temperature during deposition is notable for promoting sulfur dissociation on the surface. After deposition the sample was cooled to the observation temperature, around 5 K. We report sulfur coverage on the terraces rather than total sulfur coverage (which includes step decoration).

Figure 1 shows the heart-shaped Cu_2S_3 clusters on a Cu(111) terrace. They adopt three different orientations, rotated by 120° , in equal abundance. These orientations are such that the lobes of the heart align with three of the six close-packed directions of the Cu(111) surface.

We have used density functional theory (DFT) to check whether this assignment is reasonable in terms of stability, shape, orientation, and density. A variety of possible clusters, with optimized configurations, are

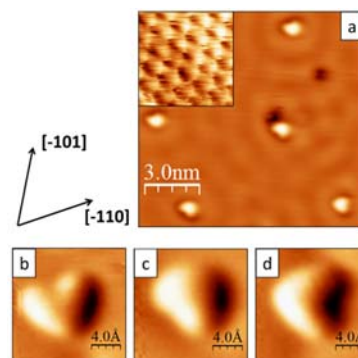


FIG. 1. STM images of Cu_2S_3 on Cu(111). **a)** Several Cu_2S_3 hearts on the terrace at low sulfur coverage, inset: atomic resolution of clean Cu(111). **b-d)** Derivative images of the three orientations of the hearts.

represented in Fig. 2. The chemical potential of S (μ_S) and the cluster diffusion barrier (E_d) appear at the top of each panel. The Cu_2S_3 complex in Fig. 2(a) has lower μ_S (and lower formation energy) than any others we have found.

Second, we have simulated the shape of the complexes using the Tersoff-Hamman method. The heart shape is evident for Cu_2S_3 and is compatible with the data. Furthermore, the area of the simulated Cu_2S_3 complex is $0.40\text{-}0.42\text{ nm}^2$, in good agreement with the experimental result ($0.39 \pm 0.04\text{ nm}^2$).

Third, to assess orientation, consider the two Cu_2S_3 complexes shown in Fig. 2(a-b). Both can have 3 energetically-equivalent orientations. Considering the pair of Cu atoms as a one-dimensional step edge, one S atom lies along an A-step, and the others (comprising the lobes) are along a B-step. This is exactly the experimental observation. In short, the stability of complex (a) can be rationalized by the presence of one S atom in a p4fh site, whereas (b) has none.

Finally, we examined Cu_2S_3 role in copper mass transport and compared to the complexes shown in Fig 2, as well as the Cu adatom. As previously mentioned, the formation of the Cu_2S_3 is lower than the other complexes, as well as the Cu adatom. The diffusion energy for this complex is also the lowest of these complexes. Both of these factors suggest that the Cu_2S_3 complex is responsible for mass transport in this system.

In summary, the predominant S-induced features on the Cu(111) terraces, at very low S coverages, are heart-shaped protrusions. DFT supports their assignment as Cu_2S_3 clusters. These clusters are always oriented in a way that allows one S atom in the cluster to bond at a p4fh site. This is different than any type of metal-sulfur surface complex observed previously, to our knowledge. Kinetic analysis shows that Cu_2S_3 is an important species for mass transport in this system.

[References]

1. P. A. Thiel, M. Shen, D.-J. Liu, and J. W. Evans, *J. Vac. Sci. Technol. A* **28**, 1285 (2010).

*This work has been accepted for publication in *J. Phys. Chem. C*

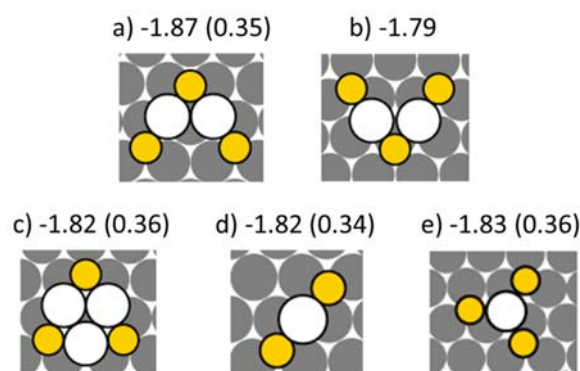


FIG. 2. Cu-S clusters on Cu(111) with lowest chemical potentials. Values of μ_S are given in eV. Diffusion barriers, E_d , are given in parentheses, also in eV. White circles represent Cu adatoms, small yellow are S adatoms, and gray are Cu atoms in the Cu(111) surface. Panels (a) and (b) are different configurations of Cu_2S_3 , (c) is Cu_3S_3 , (d) CuS_2 , and (e) CuS_3 .

Scanning Tunneling Luminescence and Theoretical Studies of Electron Energy Dissipation at a p -type GaAs(110) Surface

H. Imada,¹ K. Miwa,¹ J. Jung,¹ T. K. Shimizu,^{1,†} N. Yamamoto,² and Y. Kim¹

¹Surface and Interface Science Laboratory, RIKEN

²Department of Condensed Matter Physics, Tokyo Institute of Technology

[†]Current address: National Institute for Materials Science

Electron injection from the tip of a scanning tunneling microscope into a p -type GaAs(110) surface has been used to induce luminescence. Atomically-resolved photon maps revealed a significant reduction in luminescence intensity at surface states localized near Ga atoms. Quantitative analysis based on first principles calculations and a rate equation approach was performed to describe the perspective of electron energy dissipation at the surface. Our study reveals that non-radiative recombination through the surface states is a dominant process for the electron energy dissipation at the surface, which is suggestive of the fast scattering of injected electrons into the surface states.

Energy dissipation of electrons, such as recombination and scattering, plays a significant role in current electronic technologies. In particular, recombination at surfaces is one of the principal processes responsible for reducing the operational efficiency of (opto)electronic devices and (photo)catalytic systems. However, thus far, it has not been feasible to obtain quantitative information about surface recombination at the atomic-scale, mainly because of technical limitations.

We investigated energy dissipation at a p -type GaAs(110) surface with atomic-resolution using scanning tunneling luminescence (STL) spectroscopy (Fig. 1(a)). The experimental data were theoretically analyzed using first principles calculations and a rate equation approach.

Figure 1(b) shows STL spectra measured at various sample voltages and a photoluminescence (PL) spectrum as a reference. Luminescence in STL was observed only at positive sample bias voltages within a range of $|V_s| \leq 2$ V, and the spectrum shape does not depend on the bias voltage. The shape of the STL spectra is almost identical to that of PL. Because the luminescence in PL occurs mainly inside the bulk, it is concluded that the light emission in STL also occurs inside the bulk.

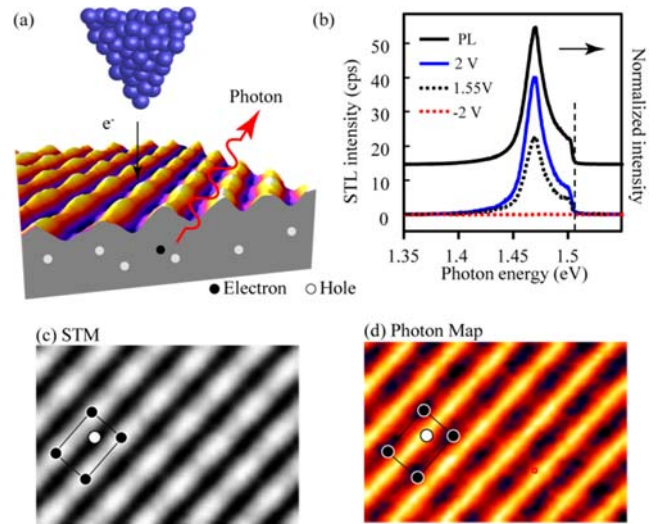


FIG. 1 (a) A schematic drawing of STL measurement of p -doped GaAs. Luminescence inside the bulk is induced by electron injection with an STM tip. (b) STL spectra at various voltages and PL spectrum measured on the same sample. (c) An atomically resolved STM image and (d) an STL photon map of GaAs(110) ($V = 1.8$ V). A unit cell at identical positions is shown (black: Ga, white: As).

An atomically-resolved STM image and STL photon map measured at a sample voltage of 1.8 V are shown in Fig. 1(c) and (d). The atomic rows in the STM image apparently run in the [001]. STL photon maps show similar stripe-like patterns running in the [001] direction. However, opposite to the STM, which shows bright spots at Ga sites, dark spots were observed at Ga sites in the photon map.

Local variation of the photon intensity in STL (Fig. 1(d)) can be analyzed by considering local electron-injection into the electronic states distributed on the GaAs(110) surface and dynamic processes of the electrons at the surface. We investigated the electronic structure of GaAs(110) using density functional theory (DFT) calculations. Figure 2(a) shows the band structure of the GaAs(110) surface, in which the bulk band structure is also projected for comparison. Figures 2(b)-(d) show spatial distribution of charge densities of the electronic states in the lowest unoccupied band at Γ - and X -points which dominantly contribute to electron tunneling in our experimental condition. Figure 2(b) clearly displays that $|\Psi_{1,\Gamma}|^2$ penetrates into the bulk whereas $|\Psi_{1,X}|^2$ is localized at the surface. Figure 2(c) shows a relatively uniform distribution of $|\Psi_{1,\Gamma}|^2$ on the surface. In contrast, $|\Psi_{1,X}|^2$ is strongly localized around the surface Ga atoms (Fig. 2(d)).

Next, we consider dynamics of the electrons injected into the surface states. We assume that electrons are injected into either Γ - or X -points, and the radiative recombination takes place only at the Γ -point. It is noteworthy that the bottoms of Γ - and X -valleys of the C_3 band are close in energy and the electrons can be scattered between these valleys. By solving rate equations regarding the number of electron in Γ - and X -points, we found that 99.99% of the electrons injected into the Γ -point are scattered into the X -point via $\Gamma \rightarrow X$ intervalley scattering, and 53% of the electron in X -point go through non-radiative recombination at the surface.

In conclusion, we have investigated electron energy dissipation at the p -type GaAs(110) surface based on atomically resolved STL observations and theoretical analysis. Tunneling electrons injected into the surface mainly undergo non-radiative recombination through the surface states localized near surface Ga atoms. The key process should be the fast $\Gamma \rightarrow X$ intervalley scattering that prevents the injected electrons from penetrating into the bulk conduction band, which suppresses the luminescence in the bulk. Microscopic analysis of carrier injection, scattering and recombination processes with atomic spatial resolution would contribute to the fundamental understanding of carrier dynamics and energy conversion at surfaces.

[Reference]

1. P. Ebert *et al.*, *Phys. Rev. Lett.* **77**, 2997 (1996).
2. M. Hoshino, and N. Yamamoto, *MRS Symposium Proceeding* **738**, 149 (2002).
3. D. Fujita, K. Onishi, and N. Niori, *Nanotechnology* **15**, S355 (2004).

*This work has been submitted to *Phys. Rev. Lett.* (under review process)

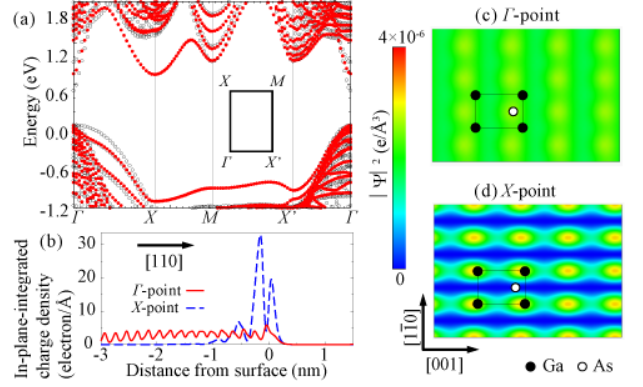


FIG. 2. (a) Band structure for GaAs(110) surface (red) and projected bulk band structure (black). (b) Charge densities $|\Psi_{1,i}|^2$ ($i = \Gamma, X$) were plotted as a function of the distance from the surface. (c), (d) Charge densities $|\Psi_{1,i}|^2$ ($i = \Gamma, X$) in a (110) plane.

Thickness dependence of electronic structures of single H₂Pc on NaCl ultrathin insulating films

Miyabi Imai^{1,2} Hiroshi Imada² Tomoko K. Shimizu^{2,†} Maki Kawai¹ and Yousoo Kim²

¹Advanced Materials Science, School of Frontier Sciences, the University of Tokyo

²Surface and Interface Science Laboratory, RIKEN

[†]Current address: National Institute for Materials Science

Tuning the electronic structure of organic molecules in contact with metal substrates is essential to achieve efficient charge transport in various organic devices. Ultrathin insulating films are useful in this regard because they work as buffer layers. In addition to electronically decoupling adsorbates from metal substrates, new dimensionality, *i.e.*, thickness, enables to control surface properties such as work function¹ and chemical reactivity². There have been many reports on scanning tunneling microscopy/spectroscopy (STM/STS) studies of organic molecules adsorbed on ultrathin insulating films, but correlation between film thickness and electronic structures of adsorbates has not been clarified³. In this study, we investigated the electronic structure of single metal-free phthalocyanine (H₂Pc), which is a p-type π -conjugated molecule, adsorbed on ultrathin NaCl films with various thickness on a Au(111) single crystal using low temperature STM/STS.

By depositing NaCl with the sample held at room temperature (RT), 1 and 2 ML (100)-terminated NaCl islands were observed (Fig. 1a). After a subsequent sample anneal to about 100 °C, 4 ML NaCl islands as wide as 100 nm² could be found (Fig. 1b). This enables us to use 1, 2, and 4 ML NaCl islands and bare Au(111) as substrates. H₂Pc adsorbed on all substrates as a single isolated molecule (Fig. 1c).

The dI/dV spectrum of the molecule on each substrate (Fig. 2a) shows two peaks whose origins are HOMO and quasi-degenerated LUMO and LUMO+1 but the peak positions are different by several hundred mV with the thickness of NaCl insulating films. Comparing molecular levels on different thick NaCl films, an energy diagram is useful since which refers to the vacuum level whereas the lateral axis of STS spectra refer to the Fermi levels of the substrates even though the work function of the substrates has thickness dependence.

In order to determine the differences of the work function, we measured dZ/dV spectra on 1, 2, 4 ML NaCl films (Fig. 2b). The peaks pointed by arrows are the field emission resonances whose energy shifts are related to the work function differences. The averaged peak shifts of 1, 2 and 4 ML NaCl films from bare Au(111) are 0.95 eV, 0.72 eV and 0.80 eV respectively, indicating the work function difference between them are several hundred meV and depend on the NaCl thickness.

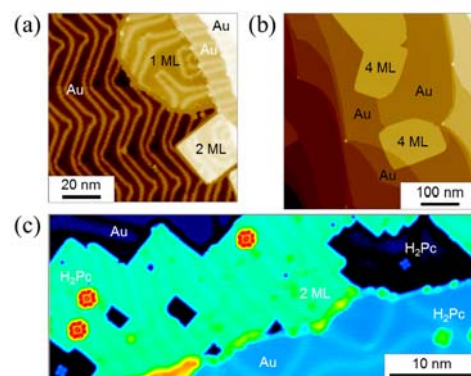


Fig.1 STM image obtained after NaCl deposition (a), after annealing (b), and after H₂Pc deposition. (a), (b) $V_b = -2.0$ V, $I_t = 4$ pA, (c) $V_b = +1.3$ V, $I_t = 4$ pA

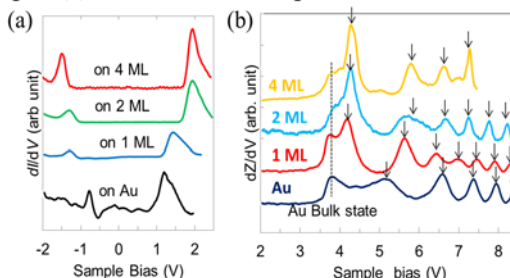


Fig.2(a) dI/dV spectra of single H₂Pc on Au(111), and 1, 2, and 4 ML NaCl islands. (b) dZ/dV spectra measured on bare Au(111), 1, 2, and 4 ML NaCl films.

We also take into account of the difference of potential drop within NaCl films with different thickness. It should be noted that on insulating films STS peak positions of HOMO and LUMOs are not equivalent to the molecular levels because of the potential drop within the films because molecules exist on NaCl films. HOMO and LUMO levels at the zero bias (E_{HOMO} , E_{LUMO}) can be determined by subtracting V_{NaCl} from their peak energies (V_{HOMO} , V_{LUMO}) in STS spectra.

$$E_{HOMO/LUMO} = V_{HOMO/LUMO} - V_{NaCl}$$

V_{NaCl} can be deduced by simple approximation, considering this junction as a capacitor partially filled with a dielectric material. From the formula in the field of classical electromagnetism, and the result that applied bias (V_{sample}) is the sum of V_{NaCl} and V_{vac} , V_{NaCl} is represented by the following equation.

$$V_{NaCl} = \frac{\frac{z\epsilon_r}{d}}{1 + \frac{z\epsilon_r}{d}} V_{sample} = \frac{z\epsilon_r}{d + z\epsilon_r} V_{sample}$$

Here, ϵ_r is relative dielectric constant of the dielectric material. From these equations, E_{LUMO} and E_{HOMO} were calculated using the parameters shown in Table1.

With the deduced values of work function differences and potential drops within NaCl films, the energy diagram was constructed (Fig. 3). From the diagram, mainly two obvious features were found: the increase of the gap with the thickness and the alignment of the gap centers within the margin error. The gap broadening is found in the previous studies on various kinds of molecule/metal systems using photo electron spectroscopies. This phenomenon is explained as a result of coulomb interaction with an image charge. The alignment of the gap suggests that the center is independent from the work function of the substrate, indicating the controllability of the energy gap between molecular levels and E_F , which is important for charge injection, solely by the work function. The fact that the gap center on Au(111) did not align is the evidence that the rule of the molecular level alignment on an ultrathin insulating film is totally different from those on a metal substrate. While the molecular level alignment on Au(111) shows the coupling with the Fermi level, those on NaCl films is explained by the model of the vacuum level alignment combined with image charge effect. These result suggest Our results show two the most important aspect on the molecular electronic structure, HOMO-LUMO gap size and the energy difference between the Fermi level of substrates and the levels of frontier orbitals, is tunable by the thickness of insulating films and work functions of the substrates. Our results suggest one way to control of molecular electronic structures with the thickness of buffer layers.

[Reference]

1. H. C. Ploigt et al., *Phys. Rev. B* **76**, 195404, 2007.
2. J. Jung et al., *Phys. Rev. B* **82**, 085413, 2010.
3. J. Repp et al., *Phys. Rev. Lett.* **94**, 026803, 2005.

Table Parameters used for the calculation of potential drop. ϵ_r : dielectric constant, z : the distance between the tip and the substrate, d : the thickness of the NaCl film.

	ϵ_r	z (pm)	d (pm)
1 ML	2.0	1032	288
2 ML	3.2	841	576
4 ML	5.9	628	1152

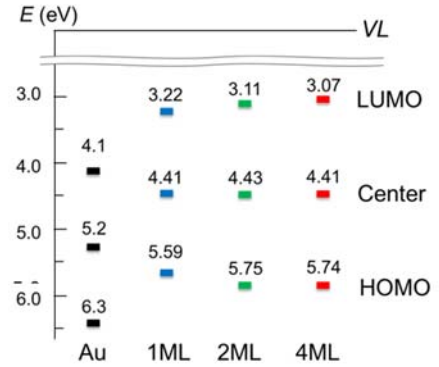


Fig. 3 the energy diagram of H₂Pc/NaCl/Au(111). The levels of LUMO, HOMO and the center of HOMO and LUMO are shown.

Finding isomerization pathways for a single azobenzene derivative on the Ag(111) surface

Emiko Kazuma¹, Mina Han², Jaehoon Jung¹, Junepyo Oh¹, Takahiro Seki², and Yousoo Kim¹

¹Surface and Interface Science Laboratory, RIKEN

²Department of Molecular Design and Engineering Graduate School of Engineering, Nagoya University,

Azobenzene is one of the most attractive candidates for molecular switches based on the difference in conductance between *cis*- and *trans*- isomers. Although the *cis*-*trans* isomerization has been well studied on photochromism, the isomerization pathway has not been clarified yet. Two proposed pathways of in-plane inversion by bending NNC bond and out-of-plane rotation by torsion of two phenyl rings (Fig. 1) have been controversial.¹⁻³

Scanning tunneling microscopy (STM) provides real-space evidence of molecular motions and structure changes and has been applied to investigating the isomerization of a single azobenzene not only by imaging at single-molecule level but also by inducing the isomerization with tunneling electrons from the tip of an STM.^{2,3} If obvious different changes in molecular configuration depending on the isomerization pathways can be directly visualized with the STM, the preferential pathway would be clarified. Herein, we strategically designed and synthesized an original azobenzene derivative with asymmetric functional groups to make it easy to distinguish molecular configuration in STM images for clarifying the isomerization pathway.

We investigated isomerization pathways of a single 4-isopropoxy-3'-methoxyazobenzene (IMA) (Fig. 1) molecule adsorbed on Ag(111) surface with a cryogenic (5 K) ultra-high vacuum STM (Omicron GmbH). We observed four different IMA isomers before and after injection of tunneling electrons (Fig. 2a). The compact molecules are two different *cis*-isomers (*cis*-A and B) and the elongated molecules are two different *trans*-isomers (*trans*-A and B). To confirm this assignment, we calculated electrostatic potential (ESP) maps. The high negative density of the ESP map for a molecule weakly adsorbed on a metal surface often corresponds to protrusions in STM images obtained at low voltages². The ESP maps in Fig. 2b agree well with the STM images in Fig. 2a. Right after vacuum deposition,

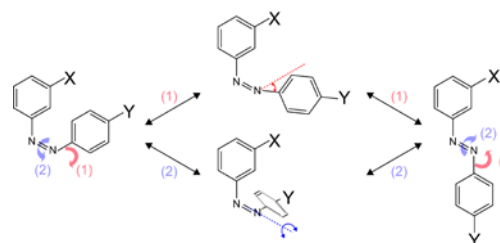


Figure 1 Two isomerization pathways of azobenzene derivatives. (1) inversion (CNN bending) and (2) rotation (CNNC torsion). Functional groups of IMA are X = OCH₃ and Y = OCH(CH₃)₂.

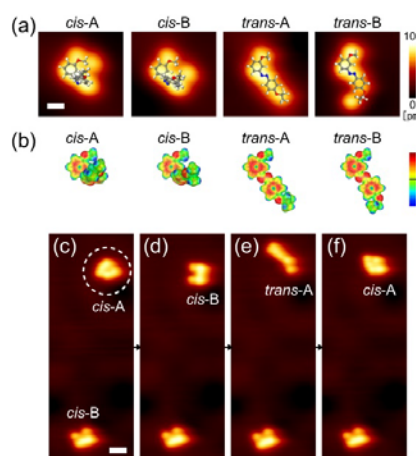


Figure 2 (a) STM images of four different IMA-isomers superimposed with ball-and-stick models as optimized in the gas phase. (b) ESP maps of the same models in (b). STM images (c) before and (d-f) after sequential injection of tunneling electrons into the molecule in the white dot circle in (c). The conditions of applied voltage pulse [tip bias(V_t), tunneling current (I_t), time (t)] are [0.45 V, 1.0 nA, 5 sec], [1.6 V, 1.0 pA, 5 sec], and [0.5 V, 1.0 pA, 5 sec] for (d), (e) and (f), respectively. All STM images were measured at 0.1 V and 0.1 nA. Scale bars are 0.5 nm in (a) and 1.0 in (c-f), respectively.

two different *cis*-isomers were observed and 72% was *cis*-A and 28% was *cis*-B from total of 141 molecules.

To explore isomerization behavior of a single IMA, the STM tip was placed above the N=N bond of IMA and tunneling electrons were injected. A *cis*-A molecule changed to *cis*-B (Fig. 2c→d) during applying pulse at ≥ 0.42 V and *cis*-B reverted to *cis*-A at ≥ 0.48 V. Therefore, although the reversible conformational changes between *cis*-A and B were achieved, the isomerization from *cis*- to *trans*-IMA cannot be induced by vibrational excitation at lower bias unlike the previous report.²

In contrast, under the higher bias, both *cis*-A and B isomerized to *trans*-A (Fig. 2d→e) and *cis*-B isomerized to *trans*-B. Bias dependencies of the reaction probability indicate the *cis*-A selectively isomerized to *trans*-A at ~ 1.5 V but the *cis*-B isomerized competitively to *trans*-A or B at ~ 1.5 V. On the other hand, *trans*-A reverted to rather *cis*-A than *cis*-B (Fig. 2e→f) at ~ 0.5 V, because the reaction barrier might be lower than that for isomerization from *trans*-A to *cis*-B. Reversion from *trans*-B to *cis*-B was also achieved at ~ 1.5 V although the half of them was broken. Therefore, the reversible isomerization of IMA was achieved by exciting molecules with tunneling electrons. Isomerization from *trans*-B to *cis*-A and conformational changes between *trans*-A and B were not observed.

Since *cis*-*trans* isomerization should occur via the in-plane inversion or the out-of-plane rotation, we can determine a preferential pathway by comparing the molecular structures from the geometrical viewpoint. From the STM images, *trans*-A has elongated structure which results from increase in the CNNC bond angle of *cis*-A. This means the isomerization pathway from *cis*-A to *trans*-A is inversion and vice versa. In contrast, two functional groups of *trans*-B are located at opposite sides across the azobenzene body, which would be possible only by rotation around the N=N bond of *cis*-B. Thus, the reversible isomerization between *cis*-B and *trans*-B is based on rotation. The suppression of the isomerization between *cis*-A and *trans*-B would be due to steric hindrance between two functional groups during rotation. Thus, the rotation pathway is forbidden for *cis*-A. As summarized in the potential energy surface in Fig. 3, only the inversion pathway is allowed for *cis*-A and *trans*-A, but on the other hand, both inversion and rotation pathways are competitive for *cis*-B. Therefore, we concluded that the isomerization pathway is different depending on the initial structure of the molecules.

In conclusion, we have clarified the isomerization pathways of IMA molecules on Ag(111) as the structure changes observed with STM at single-molecule level. The IMA molecules on Ag(111) have two stable *cis* structures (*cis*-A and B) and reversible isomerization between *cis*- and *trans*-IMA was achieved by injecting tunneling electrons. The isomerization mechanism is different depending on the initial structure of the molecules. These findings would give a guide to design azobenzene derivatives for the development of molecular switches.

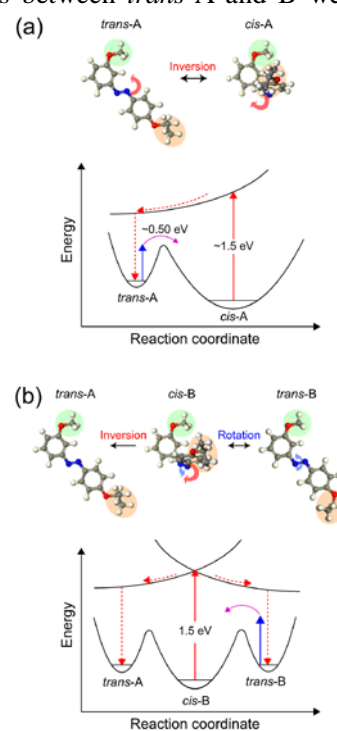


Figure 3 Schematic illustrations for the isomerization pathways and the potential energy diagrams.

- [References]** 1) H. Rau, E Lüddecke, *J. Am. Chem. Soc.* **1982**, *104*, 1616. 2) J. Henzl, et. al, *Angew. Chem. Int. Ed.* **2006**, *45*, 603.
3) B.-Y. Choi, et. al, *Phys. Rev. Lett.* **2006**, *96*, 156106.

Lattice-Contraction-Induced Moiré Patterns in Direction-Controlled Epitaxial Graphene on Cu(111)

Hyunseob Lim, Jaehoon Jung, Hyun Jin Yang and Yousoo Kim

Surface and Interface Science Laboratory, RIKEN

We demonstrated the direction-selective growth of epitaxial graphene (EG) on Cu(111) for the first time. Our results imply that the synthesis of EGs with a unidirectional orientation on Cu surface is also feasible, although Cu has been well-known as a weakly interacting metal with graphene. We also developed a novel method to analyze various Moiré patterns induced by lattice contraction in EGs even with a unidirectional orientation.

Chemical vapor deposition on a Cu surface is one of the feasible methods for industrial applications, because large-area monolayer graphene film can be achieved. However, grain boundaries- and wrinkle-formation in the graphene film are known to reduce the electrical performance of graphene. One of the ideal methods to achieve the uniform graphene films with high quality is controlling orientations of each grain in graphene as an identical direction. Nevertheless, the direction-controlled growth has never been realized on Cu surface because of the weak interaction between Cu and EG. Indeed, previous STM studies only showed EGs with various $R\theta$ on Cu(111). [Gao et al., Nano Lett. 2010, 10, 3512-3516.]

This study describes the unidirectionally grown EGs by means of atomically-resolved STM imaging and the analysis of Moiré patterns. Both STM images showing EG and Cu lattices together and the atomic-resolution analysis of Moiré patterns revealed that the *zigzag* direction of EG edge is identical to the $[1\bar{1}0]$ direction of Cu(111) (0 degrees of rotational angle ($R\theta=0^\circ$)) (**Figure 1(c and d)**). Both Fourier-transformed (FT) images obtained from EG and Cu(111) regions (Figure 1e and f, respectively) also show hexagonal spot patterns with the same directions in a reciprocal space. Our observations, therefore, clearly reveal that the *zigzag* direction of EG is well-matched with the symmetric $\langle 1\bar{1}0 \rangle$ axes of the Cu(111) surface ($R\theta = R0^\circ$) (**Figure 1(e and f)**). In addition, we observed various Moiré patterns even with an identical rotational angle (all EGs in our experiments are direction-controlled) (**Figure 2**), which cannot be explained by the conventional method with rotational angle dependence. For understanding this observation, we considered the influence of “lattice contraction in

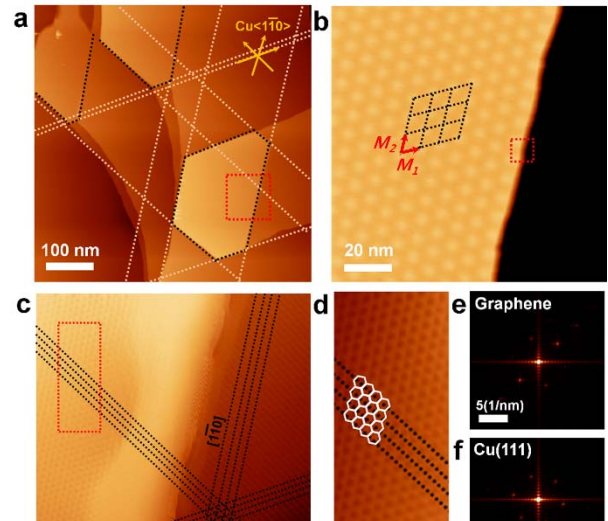


Figure 1. (a) Large area STM image of EGs. (b) STM image of Moiré pattern corresponding to red-dotted rectangle in Figure 1a. (c) STM image corresponding to red-dotted rectangle in Figure 1b. (d) Atomically-resolved STM image of the red-dotted rectangle in Figure 1c. The atomic arrangement of carbon atoms is depicted with white lines. (e and f) 2D FT images of (e) EG and (f) Cu(111), respectively.

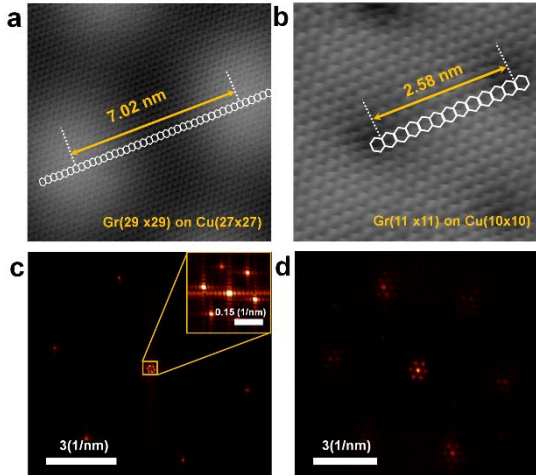


Figure 2. (a and b) Atomic-resolution STM images of Moiré patterns with (a) 7.02 nm and (b) 2.58 nm of L_M . In those STM images, (a) 29 and (b) 11 of benzene rings are counted between the closest two Moiré spots. (c and d) 2D FT images from STM images in Figure 2a and 2b, respectively. Inset image in Figure 2c corresponding to the small yellow rectangle at the center of Figure 2c.

graphene contraction on Moiré patterns with identical $R0^\circ$ was also investigated to explain various types of Moiré patterns observed in our EGs by using a correlation plot between L_M^{Cal} and $\Delta a_{Gr}^{Cal}/a_{Gr}$. This approach is not only reliable for our observations, but also useful in determining the precise atomic scale structure of EG on the other surfaces.

These atomic scale studies would accelerate fundamental studies for a better understanding of the interactions between graphene and a metal surface, as well as the practical development of a synthetic method for higher quality graphene films on Cu surfaces.

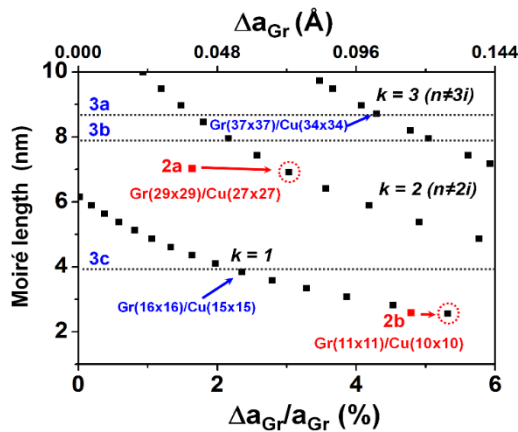


Figure 3. A correlation plot of all plausible L_M versus $\Delta a_{Gr}/a_{Gr}$ values depending on the n and k values, when $\rho = 0$ ($R0^\circ$). L_M^{Exp} and $\Delta a_{Gr}^{Exp}/a_{Gr}$ values for 2a and 2b are marked with red-filled rectangles, and L_M^{Exp} values for 3a, 3b and 3c are plotted by black dotted lines. Several L_M^{Cal} and $\Delta a_{Gr}^{Cal}/a_{Gr}$ values of ($Gr(n \times n)/Cu(n' \times n')$) corresponding to experimentally-observed Moiré patterns are indicated by blue arrows for convenient understanding.

*This work has been published in Adv. Mater. Interfaces 1 (2014) 1300080

EG”, and suggested a novel analysis method utilizing a correlation plot between the degree of EG lattice contraction and the length of the corresponding Moiré patterns. For the EGs on Cu(111) with $R0^\circ$, Moiré superstructures can be represented as $Gr(n \times n)/Cu(n' \times n')$, indicating that the primitive unit cells of the Moiré superstructures are composed of $n \times n$ and $n' \times n'$ unit cells of EG and the Cu(111) surface, respectively. Then, L_M and $\Delta a_{Gr}/a_{Gr}$ values can be calculated (L_M^{Cal} , $\Delta a_{Gr}^{Cal}/a_{Gr}$) for all possible Moiré superstructures generated by the given n and n' . Thus, L_M^{Cal} and $\Delta a_{Gr}^{Cal}/a_{Gr}$ for each $Gr(n \times n)/Cu(n' \times n')$ can be obtained by using Equation (3) and (4).

$$\Delta a_{Gr}^{Cal}/a_{Gr} = 1 - (n - k) a_{Cu}/n a_{Gr} \quad (k = n - n', n \neq ki, i: \text{integer}) \quad (3)$$

$$L_M^{Cal} = n a_{Gr} (1 - \Delta a_{Gr}^{Cal}/a_{Gr})$$

Structurally-Driven One Dimensional Electron Confinement in Sub-5-nm Graphene Nanowrinkles

Hyunseob Lim and Yousoo Kim

Surface and Interface Science Laboratory, RIKEN

Graphene-based carbon materials such as fullerenes, carbon nanotubes, and graphenes have distinct and unique electronic properties that depend on their dimensionality and geometric structures. Graphene wrinkles with pseudo one-dimensional (1D) structures have been observed in a graphene sheet. However, their 1D electronic properties have never been observed because of their large widths. We demonstrate the unique electronic structure of graphene nanowrinkles (GNW) in a graphene sheet grown on Ni(111), the width of which was small enough (less than 5 nm) to cause 1D electron confinement. Use of spatially resolved, scanning tunneling spectroscopy revealed band-gap opening and a 1D van Hove singularity in the GNW, as well as the chemical potential distribution across the GNW. Our demonstration of 1D electron confinement in a graphene creates the novel possibility of controlling its electronic properties not by chemical modification but by “mechanical structuring in a controlled manner”.

Epitaxial graphene (EG) with GNWs was synthesized by dissociating acetylene on a clean Ni(111) surface. The rapid cooling process is necessarily required, which is the most critical step to

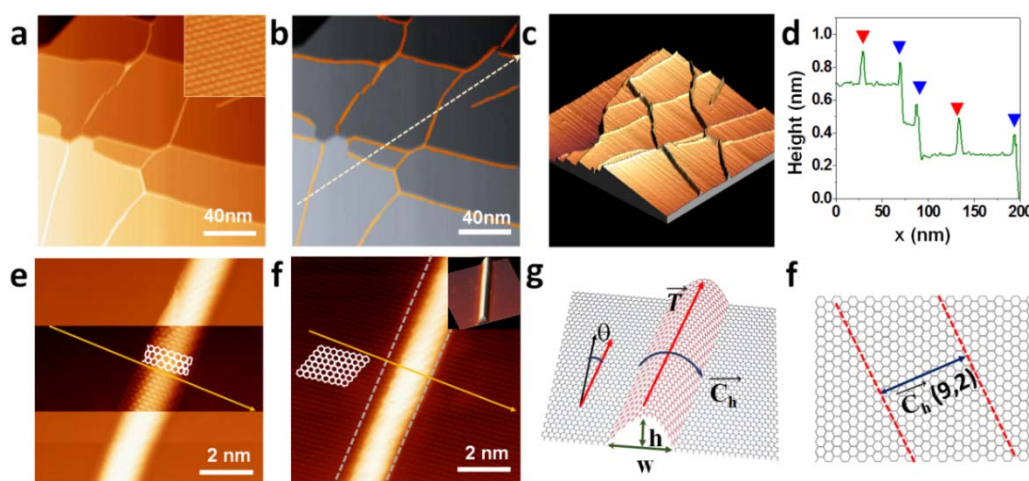


Figure 1. **a–c**, STM images of EG on Ni(111). **a**, Original image, (inset) graphene lattice on pEG region. **b**, Recolored image showing GNWs with orange color. **c**, 3D STM image of the EG and GNWs. **d**, Height profile along the white dashed arrow in **b**. Red triangles and blue triangles indicate the GNWs on the terrace of the Ni(111) surface and at step edges of the Ni(111) substrate, respectively. **e, f**, High-resolution STM images with different scanning conditions. **e**, (top and bottom) $V_s = 1$ V and $I_f = 1$ nA, (center) $V_s = 0.05$ V and $I_f = 1$ nA. Orange arrows indicate the \vec{C}_h direction identified in **g**, and white hexagonal patterns indicate the carbon atoms. **f**, $V_s = 0.05$ V and $I_f = 6$ nA. **g, h**, Schematic drawings **g** to clarify the meaning of the parameters used to specify the structure of the GNWs and **h**, for the (9,2) GNW observed in **e** and **f**.

synthesize GNWs. Most of the GNWs were observed in the region where the terrace width of the underlying Ni surface was as short as several tens of nanometers (Fig. 1a–c). These GNWs have been recolored with orange in Fig. 1b, and a line profile along the white arrow in Fig. 1b is plotted in Fig. 1d, which shows that the GNWs on the terrace have larger widths and lower heights than the GNWs at the step edges.

The electronic structures of GNWs located on the terraces of the underlying Ni(111) were investigated by scanning tunneling spectroscopy (STS) and dI/dV mapping. The dI/dV spectrum measured

on the GNW (red line in Fig. 2a) by STS included four strong peaks, v_1 and v_2 for the valence band side, and c_1 and c_2 for the conduction band side, the indication being that there were discrete electronic states in the local density of states (LDOS). There was no evidence of such discrete electronic states on the pEG area (blue line in Fig. 2a). The Dirac point was not clearly apparent, even on the pEG area, because chemisorption on a Ni substrate strongly perturbs the electronic structure of graphene. The dI/dV image revealed the spatial distribution of the LDOS. The dI/dV images were obtained at various V_s voltages, including the voltages at peak positions [$V_s = -0.6$ V (v_1) and 0.5 V (c_1)] and between v_1 and c_1 ($V_s = -0.2$, 0.01, and 0.2 V) as well. At the peak positions, the measured dI/dV intensities, which are indicative of the LDOS, were higher on the GNW area than on the pEG area. In contrast, lower LDOSs were observed on the GNW at V_s values in the energy gap between v_1 and c_1 (ΔE_g); this behavior is similar to the “band-gap opening” feature of a single-walled CNT (SWCNT). These discrete states in LDOS have never been observed in the STS previously performed on other graphene wrinkles. To examine the plausibility of the other possible mechanism, 1D electron confinement, we investigated the width dependence of 1D electron confinement. It is apparent that ΔE_g values decreased with increasing widths of the GNWs, but vHS peaks were not observed in GNWs with widths greater than 3.5 nm. We therefore suggest that 1D electron confinement is the most likely explanation for the unique states in GNWs.

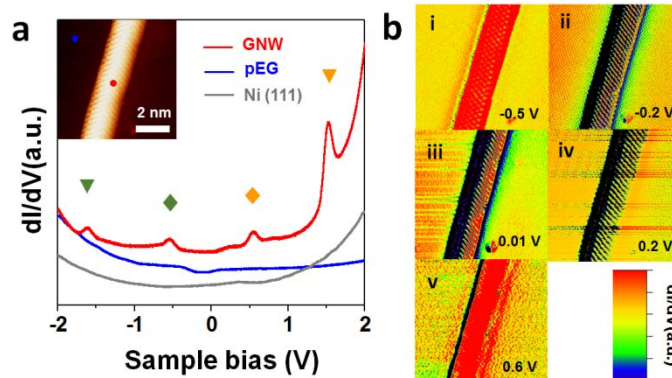


Figure 2. **a**, STS spectra on (gray line) bare Ni(111), (blue line) flat graphene, and (red line) GNW. The symbols above the peaks indicate (green diamond) v_2 , (green triangle) v_1 , (orange triangle) c_1 (from conduction band), and (orange diamond) c_2 . **b**, dI/dV mapping images of GNWs obtained at $V_s =$ (i) -0.5 V, (ii) -0.2 V, (iii) 0.01 V, (iv) 0.2 V, and (v) 0.6 V.

*This work has been submitted to Nature Nanotechnology (under review process).

Lateral hopping of a CO on Ag(110) by multiple overtone excitation

Junepyo Oh¹, Hyunseob Lim^{1,5}, Ryuichi Arafune², Jaehoon Jung¹, Hiromu Ueba³, Maki Kawai⁴, and Yousoo Kim^{1*}

¹Surface and Interface Science Laboratory, RIKEN, Japan

²International Center for Materials Nanoarchitectonics, National Institute for Materials Science, Japan

³Division of Nano and New Functional Materials Science, University of Toyama, Japan

⁴Departments of Advanced Materials Science, University of Tokyo, Japan

⁵Center for Multidimensional Carbon Materials, Institute of Basic Science, Korea.

The vibrational excitation of adsorbate on metal surface has been extensively studied as a fundamental step of various surface dynamic phenomena [1,2]. Vibration-mediated molecular dynamic behaviors on solid surface, involving molecular motion and reaction, can be induced by inelastic electron tunneling (IET) process with a scanning tunneling microscope (STM). Action spectroscopy with STM (STM-AS) [3] reveals vibrational energies of a single molecule based on the dynamic response, such as hopping, rotation, desorption and chemical reaction, to the excitation energy of inelastically tunneled electrons from the STM tip. In this study, we have investigated the lateral hopping motion of a CO molecule adsorbed on Ag(110) surface by using STM-AS method. The mobility of CO molecules adsorbed on Ag(110) surface was reported by Ho et al. [4], but there are no experimental report about the dynamics of CO on Ag(110) surface. Herein, we have investigated the lateral hopping motion of a CO molecule adsorbed on Ag(110) surface by using STM-AS method to clarify the hopping mechanism experimentally.

STM-AS measurements were then carried out for vibrationally-induced hopping motion of CO molecules on Ag(110). The hopping yield $Y(V)$ and rate $R(I)$ were estimated from the current traces as function of V and I , respectively. Action spectra reveal that $Y(V)$ provides sample bias voltages corresponding to the active vibrational modes responsible for molecular hopping motion [3,5]. $R(I)$ exhibits a power-law dependence on I and reaction order n , $R(I) \propto I^n$ [6-8], and thus describes that how many electrons are required for an event. FIG. 1 shows the action spectra obtained with a tunneling current of 20 nA (●), and 1 nA (▲). The action spectra exhibit a novel feature for the vibrationally-induced hopping motion of CO molecules on Ag(110), in which the drastic increases of $Y(V)$ were observed at four threshold voltages of ~64, ~96, ~160, and ~261 mV (marked with black arrows). The observed threshold energies are surprisingly well-matched with the first, second, third overtone value of $\nu(\text{M-C})$, and $\nu(\text{C-O})$, respectively. The current dependence of the $R(I)$ was then measured as

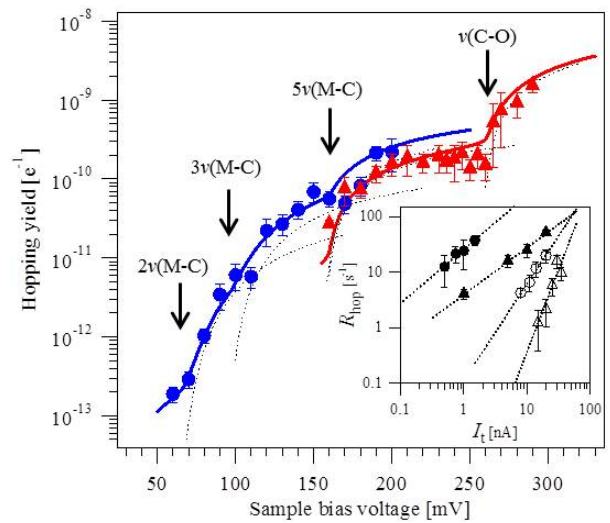


FIG. 1. Action spectra for lateral hopping of a CO molecule as a function of V . The inset shows the hopping rate (R_{hop}) of a CO molecule as a function of I for the sample bias voltages, 90 (Δ), 140 (\circ), 180 (\blacktriangle), and 280 mV (\bullet).

presented in the inset of FIG. 1. The estimated reaction orders n are 2.96, 1.73, 0.84, and 0.97 for the sample bias voltages, 90, 140, 180, and 280 mV, respectively. FIG. 2 shows a schematic diagram for the hopping mechanism through multi-step excitations of overtone modes of $\nu(\text{M-C})$, in which energy scale and ladder-climbing excitation features are described based on the experimentally obtained vibrational energy and reaction orders. The detailed hopping mechanism can be expressed as follows: (a) triple-step excitation of first overtone, $2\nu(\text{M-C})$, for $64 \text{ mV} < V_s < 96 \text{ mV}$, (b) double-step excitation of second overtone, $3\nu(\text{M-C})$, for $96 \text{ mV} < V_s < 160 \text{ mV}$, and (c) single-step excitation of fourth overtone, $5\nu(\text{M-C})$, for $160 \text{ mV} < V_s < 261 \text{ mV}$, respectively. These excited vibrational energies transfer to the RC mode (HT mode) by anharmonic coupling process [9], and finally CO overcomes the energy barrier (ϵ_B) for lateral hopping motion. The ϵ_B can be estimated as $128 \text{ meV} < \epsilon_B < 160 \text{ meV}$ from FIG. 2.

In conclusion, we investigated the lateral hopping mechanism of individual CO molecules adsorbed on Ag(110) surface using action spectroscopy with low-temperature STM. We found that lateral hopping motion of a CO can be induced not only by the excitation of $\nu(\text{C-O})$ mode but also by vibrational excitations of several overtone modes of $\nu(\text{M-C})$, especially including higher overtone modes. To the best of our knowledge, our result is the first observation on the molecular motion induced by vibrational excitations of multiple overtone modes. Our results not only open a new opportunity to utilize higher overtone modes of adsorbate for triggering elementary process of surface chemistry but also stimulate further spectroscopic and theoretical investigation to gain the deep insight into underlying surface dynamics, such as energy transfer mechanism and the influence of substrate, leading to efficient excitations of multiple overtone modes.

References

- [1] J. T. Yates and T. E. Madey, *Vibrational spectroscopy of molecules on surfaces* (Plenum Press, 1987).
- [2] H. Ueba, S. G. Tikhodeev, and B. J. Persson, in *Current-Driven Phenomena in Nanoelectronics*, edited by T. Seideman (Pan Stanford Publishing, 2010).
- [3] Y. Sainoo, Y. Kim, T. Okawa, T. Komeda, H. Shigekawa, and M. Kawai, *Phys. Rev. Lett.* **95**, 246102 (2005).
- [4] H. J. Lee and W. Ho, *Science* **286**, 1719 (1999).
- [5] K. Motobayashi, Y. Kim, H. Ueba, and M. Kawai, *Phys. Rev. Lett.* **105**, 076101 (2010).
- [6] Y. Kim, T. Komeda, and M. Kawai, *Phys. Rev. Lett.* **89**, 126104 (2002).
- [7] J. I. Pascual, N. Lorente, Z. Song, H. Conrad, and H.-P. Rust, *Nature* **423**, 525 (2003).
- [8] B. C. Stipe, M. A. Rezaei, and W. Ho, *Science* **279**, 1907 (1998).
- [9] T. Komeda, Y. Kim, M. Kawai, B. N. J. Persson, and H. Ueba, *Science* **295**, 2055 (2002).

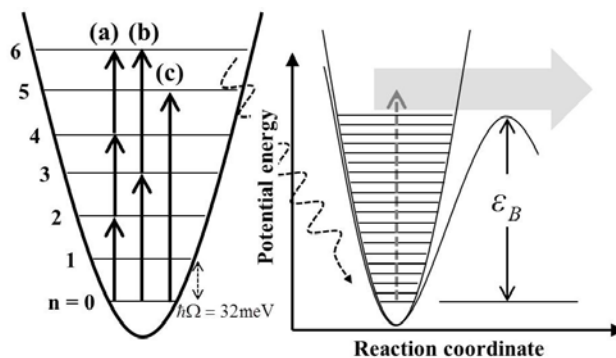


FIG. 2. Schematic representation of vibrational excitations of multiple overtone modes originated from metal-molecule stretching mode, $\nu(\text{M-C})$, 32 meV: (a) first, (b) second, and (c) fourth overtone modes.

Observation of bond weakening during photodesorption

-SFG/STM studies of CO-RuTPP/Cu(110)

Takuma Omiya,^{1,2} Heike Arnolds,² Rasmita Raval,² and Yousoo Kim¹

¹Surface and Interface Science Laboratory, RIKEN ²Surface Science Research Centre, University of Liverpool

Desorption is one of the most fundamental surface dynamics, its mechanism is still in debate. Conventionally, laser desorption has been studied by two pulse correlation measurement (2PC), simply detect desorption products by mass spectrometer. 2PC allows us to study how long does desorption takes after first pulse arrives, but no detail information about before desorption. After 2000, sum frequency generation spectroscopy (SFG) has been utilized to study contribution of vibrational excitation. Several groups proposed that frustrated rotational modes are crucial to realize desorption [1-3]. Their claims are based on transient redshift of C-O stretch mode on metal surface, which generally means CO-metal bond gets stronger, an opposite of desorption. This counterintuitive results guide us to a question, either only FR mode appear in frequency shift or other mode (CO-metal bond) also contributes but not able to see due to the larger effect by FR. Moreover, we are not sure that mechanism of laser driven desorption is same with thermal desorption. Thermal desorption can be explained by electronic friction model, on the other hand, laser desorption is thought to be occurred by DIET model, desorption induced by electronic transition. Is there any vibrational excitation in DIET process as well?

For the deeper understand of desorption mechanism, we chose a unique molecular system, namely, CO on ruthenium tetraphenyl porphyrin(RuTPP) on Cu(110) surface. The porphyrin molecule is introduced to facilitate electronic transition, which expects to induce photodesorption and direct coupling between hot electron and $2\pi^*$ of CO. Indeed, we found that facile laser desorption from CO-RuTPP/Cu(110) than CO/Cu(110) although CO-RuTPP is thermally more stable. We first doubt that resonant electronic transition occurs, however, three different frequencies namely 400nm, 532nm and 800nm pump beams shows similar desorption tendency. CW laser cannot induce measurable photodesorption. Moreover, desorption rather depends on pump fluence, so the cause likely due to the hot electrons. This is same with extensive studies of CO/metal surfaces, the question is why CO-RuTPP shows much easier laser desorption.

Next, we studied electron-vibration coupling during photodesorption to understand vibrational contribution for photodesorption. Figure 1 shows time evolution of C-O stretch modes from CO/Cu(110) and CO-RuTPP/Cu(110). CO/Cu(110) exhibits frequency shift up to -9cm^{-1} just after pump beam arrives, which is known to be driven by excitation of FR mode. Note that we do not see any measurable CO desorption from Cu(110) in this experimental condition. In contrast, CO-RuTPP shows very different frequency shift. Under the low fluence (= less desorption condition), we only see the slow and small redshift. This indicates that electronic contribution or FR coupling do not appear in CO-

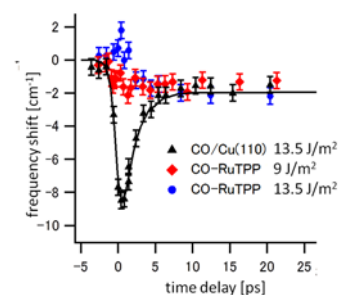


Figure 1 Transient pump induced changes in CO internal stretch frequency.

RuTPP. At the high fluence, when laser desorption become measurable, we start to see the blueshift around time zero. CO-Ru bond gets weaker. We observed similar blueshift with either 532nm or 800nm pump beam, and degree of blueshift depends on fluence.

We further investigate the origin of this blue shift. There are five possible contributions, 1) direct or 2) indirect electronic transition, 3) C-O or 4) CO-Ru vibrational excitation or 5) move to different adsorption site as a metastable state. By looking at the spectra shape during pump probe, the spectra are nicely reproduced by standard SFG equation. If hot electrons directly couples with CO $2\pi^*$, there is spectral distortion happens as observed NO/Ir(111). Moreover, we do not see the significant intensity reduction as observed in the CO/Ru(001) in desorption condition. This indicates that there is no long lived metastable state as proposed to desorption of CO/metal. We also monitors high order transition of C-O stretch mode though vibrational hot band, but do not see the significant intensity change during pump probe. Since we can eliminate four of five possibility, vibrational coupling between C-O stretch mode and CO-Ru stretch mode is most likely the origin of blue shift.

Why CO-metal excitation happens effectively on RuTPP? Direct vibrational excitation may induce desorption. To confirm this, we used scanning tunneling microscopy to perform action spectroscopy (STM-AS). STM-AS can be used to determine responsible vibrational mode of surface motion including desorption. Desorption probability against to applied voltage is plotted into figure 2-a, which indicates that low desorption probability even at 1V. This indicates that electronic transition seems required for the CO desorption. To understand electronic structure, we performed scanning tunneling spectroscopy (STS) as shown in figure 2-b, which shows several peaks after CO adsorption to RuTPP. This can be originated from ligand induced state. In the liquid phase, CO desorption from CO-RuTPP is known to trigger via $(d,2\pi^*)$ transition. This transition can be accessed from higher energy transition via thermal relaxation. This transition can alone explain the higher photodesorption probability, but no direct relation with blue shift, since we have not observed distortion of SF spectra during pump probe. So, we believe that during thermal relaxation process from higher energy electronic transition, excitation of M mode occurs to induce blueshift of C-O stretch mode.

In summary, we have observed CO desorption and blueshift of C-O stretch mode during laser irradiation. The phenomena is likely driven the $(d,2\pi^*)$ transition together with M mode excitation though the thermal relaxation from electronic transition. We report the first observation of bond weakening during photodesorption through the vibrational spectroscopy, and realize that even in the DIET process, vibrational excitation can occur.

[Reference]

1. M.Bonn *et al.*, *Phys. Rev. Lett.* **84**, 4653 (2000).
2. F.Fournier *et.al* *J.Chem.Phys.* **121**, 4839 (2004).
3. K.Inoue *et.al* *J.Chem.Phys.* **137**, 024704 (2012).

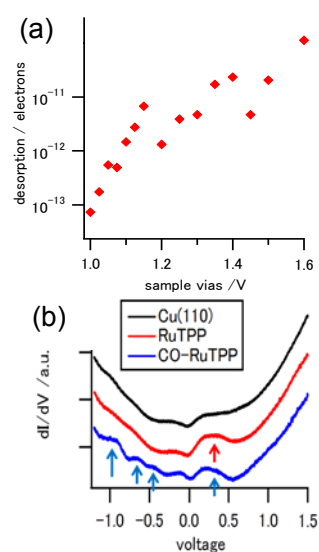


Figure 2 (a) desorption probability of CO from RuTPP/Cu(110) against to sample bias. (b) dI/dV spectra. Measurement is performed at 5K.

Supramolecular assembly through interactions between molecular dipoles and alkali metal ions

Tomoko K. Shimizu,^{1,†} Jaehoon Jung,¹ Hiroshi Imada,¹ and Yousoo Kim¹

¹Surface and Interface Science Laboratory, RIKEN

[†]Current address: National Institute for Materials Science

Establishing a way to fabricate well-ordered molecular structures is a necessary step towards advancement in organic optoelectronic devices. In this study, we revealed that the use of interactions between electric dipoles of molecules and alkali metal ions enables the formation of a well-developed homogeneous monolayer of diarylethene (DAE) molecules on the Cu(111) surface with the aid of NaCl co-deposition [1]. DAE has an intrinsic dipole resulting from its unique structure. It is well-known for its photochromism and thus switching properties as well as optoelectronic and optomechanical applications have been intensively studied. Homogeneous monolayers composed of DAE have so far been achieved by designing and synthesizing modified DAE molecules such as thiolated DAE for self-assembled monolayer. However, the strong intermolecular coupling may hamper control of the switching state of such individual molecules.

We used a simple DAE molecule called 1,2-bis(2,4-dimethyl-5-phenyl-3-thienyl)-3,3,4,4,5,5-hexafluoro-1-cyclopentene (FIG. 1) on the Cu(111) surface. Deposition of the closed-form isomer of DAE on the Cu(111) surface with pre-adsorbed NaCl islands under ultra-high vacuum lead to randomly distributed adsorption of the molecules on Cu(111). After annealing the sample at ~ 360 K, well-ordered molecular films, which are composed of linear molecular rows, appeared on Cu terraces (FIG. 2a). The same superstructure was also formed from deposition of the open-form isomers because the open-form isomer transforms into the closed-form isomer on Cu(111) using the thermal energy provided during annealing process. The stabilities of the two isomers are reversed on Cu(111) compared to that in solution [2]. Post-deposition of NaCl also results in the formation of the same structure, which strongly indicates the necessity of Na, Cl, or both for superstructure formation. To confirm this, we performed XPS experiments for two samples, *i.e.*, NaCl/Cu(111) and DAE +NaCl/Cu(111). The results indicate that Na bonds

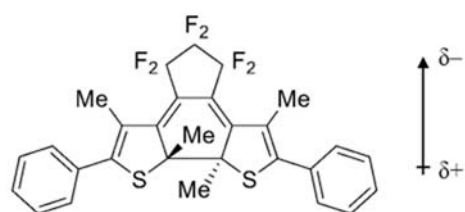


FIG. 1. Structure of the closed-form DAE used in this study and the orientation of molecular dipole moment.

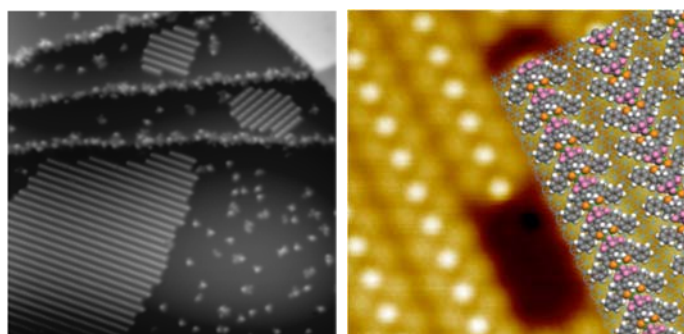


FIG. 2. a STM image ($80 \times 80 \text{ nm}^2$; -2 V , 50 pA) of closed-form DAE deposited at room temperature on Cu(111) with pre-deposited NaCl islands followed by annealing at $85 \text{ }^\circ\text{C}$. b Enlarged STM image ($9 \times 9 \text{ nm}^2$; $+1 \text{ V}$, 30 pA) with superstructure model.

FIG. 2. a STM image ($80 \times 80 \text{ nm}^2$; -2 V , 50 pA) of closed-form DAE deposited at room temperature on Cu(111) with pre-deposited NaCl islands followed by annealing at $85 \text{ }^\circ\text{C}$. b Enlarged STM image ($9 \times 9 \text{ nm}^2$; $+1 \text{ V}$, 30 pA) with superstructure model.

to DAE and Cl disappears from the surface because of the penetration into the bulk.

Analysis of enlarged STM images allowed us to construct a model for the molecular superstructure (FIG 2b). Based on it, periodic DFT calculations were carried out in order to gain insight into the formation of the DAE superstructure on Cu(111); we focused on the driving force leading to the anisotropic geometric configuration of the molecular film. FIG 3a and 3b show the most stable optimized structures for the molecular rows without and with Na⁺ ions between neighboring DAE

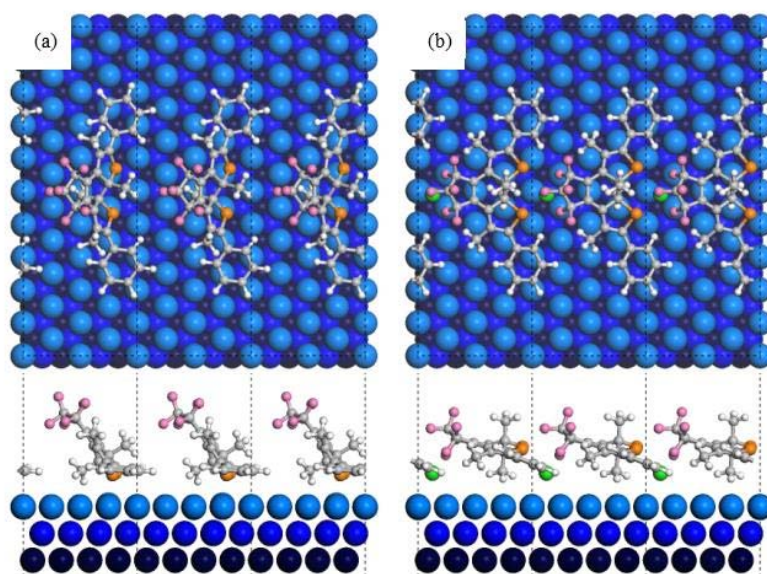


FIG. 3. Top and side views of the DFT-optimized DAE row structure without (a) and with (b) Na. C: gray, H: white, F: pink; S: orange; Na: green; Cu: blue.

molecules, respectively. In the absence of Na⁺ ions, two sulfur atoms of the DAE molecule interact mainly with the Cu substrate; this is also accompanied by van der Waals interactions between the phenyl rings and substrate. Thus, the DAE molecules should be oriented in the upright adsorption configuration. In contrast, when Na⁺ ions are inserted between neighboring DAE molecules, the adsorption orientation in the molecular row is significantly altered, in which the Na⁺ ions adsorbed on Cu(111) strongly interact with two fluorine atoms of DAE and thus draw the electronegative part of the DAE molecule closer to the substrate.

To obtain a proof of ionization of Na on the Cu(111) surface, we also extracted the charge density difference maps for the molecular row without and with Na. Depletion of the charge around Na, where its net charge is +0.77e, were found. Calculated density of states also shows Na 3s states being located in empty states away from the Fermi level. The ion–dipole interactions along the axis of the molecular row also compensate for the reduced interfacial interaction between the DAE molecules and the Cu(111) substrate.

In conclusion, we demonstrated the formation of a well-ordered superstructure of photochromic diarylethene molecules on Cu(111) by means of vacuum evaporation of either isomer with NaCl co-deposition followed by mild annealing. Na⁺ incorporation is evident from a comparison of experimental STM images with DFT calculations. The key to the superstructure formation with anisotropic geometric configuration, *i.e.*, the formation of a linear row structure, is suggested to be cation–molecular dipole interactions. Our results demonstrate a potential strategy to utilize alkali metal co-deposition to simultaneously control electronic properties and tune intermolecular interactions.

[Reference]

1. T. K. Shimizu, J. Jung, H. Imada and Y. Kim, *Angew. Chem. Int. Ed.* **53**, 13729-13733 (2014).
2. T. K. Shimizu, J. Jung, H. Imada and Y. Kim, *Chem. Commun.* **49**, 8710-8712 (2013).

Thermally activated transition from 1D to 2D superstructure: Squaric acid on Au(111)

Kan Ueji^{1,2}, Jung Jaehoon¹, Junepyo Oh¹, Kazuo Miyamura², Kim Yousoo¹

¹Surface and Interface Science Laboratory, RIKEN

²Department of Chemistry, Faculty of Science, Tokyo University of Science

Polymorphs have at least two types of unit cells. Although they contain the same molecules, polymorphs with different unit cells exhibit different physical properties. Therefore, polymorphic transitions of molecular assemblies on solid surfaces have attracted great interest for applications in the development of organic-based functional devices. Polymorphic transitions of supramolecular assemblies at liquid–solid interfaces have been extensively studied so far.^[1] However, the use of ultrahigh–vacuum (UHV) conditions provides a different approach for fabricating “solvent-free molecular assemblies” and controlling their morphology and physical properties. Studying polymorphic transitions under UHV conditions, which take place without solvents and are based on molecule–substrate interactions, intermolecular interactions, or both, are important for gaining fundamental insights into the underlying mechanisms involved. Although the structural versatility afforded by such polymorphic transitions are important for designing molecular assemblies that serve as building blocks for device miniaturization, to the best of our knowledge, there have been only a few reports on polymorphic transitions under UHV conditions with focus on the dimensionality of molecular assemblies on solid surfaces, such as changing the surface coverage.^[2]

In order to achieve polymorphic transitions with dimensional variation induced solely by thermal annealing, we herein employ squaric acid (H₂SQ) as a prototype system. H₂SQ molecule has a layered structure with hydrogen bonding. The electrical properties of H₂SQ have been reported to be strongly associated with the thermally induced phase transitions, both in the molecular crystal^[3a] as well as thin film^[3b] states.

The results of the present study indicate that the H₂SQ molecules formed two types of superstructures on Au(111). A narrow 1D ribbon structure was observed after depositing the H₂SQ molecules onto Au(111) at room temperature. Subsequent thermal annealing without additional deposition of H₂SQ molecules resulted in a polymorphic transition of the 1D ribbon structure to a 2D carpet superstructure. The 1D ribbon was long and narrow, whereas the 2D carpet was a nearly square island that was several thousand square nanometers in size. The

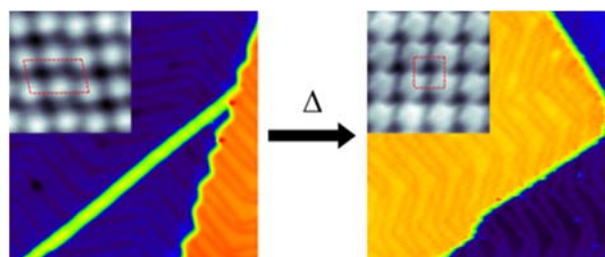


Fig. 1 STM images of (left) as-deposited 1D ribbon and (right) 2D carpet H₂SQ superstructure obtained after annealing. Inset images are at molecular resolution.

STM images of both the 1D ribbon and the 2D carpet structures indicated that they grew on large terraces without isolated molecules and small clusters, implying that there is sufficient energy for diffusion at room temperature and the H₂SQ molecules experience strong intermolecular interactions. Consequently, the polymorphic transition from the 1D ribbon to the 2D carpet structure may be strongly associated with

intermolecular interactions. In order to prove this hypothesis, molecularly resolved STM images of the ribbon and carpet with Au (resolved on an atomic-scale) were acquired. The images indicated no clear periodic coincidence of the molecular arrangement of the 1D ribbon and 2D carpet structures with the Au lattice, implying incommensurate molecular arrangements for both 1D and 2D structures on Au(111). Additionally, the experimental observations indicated that the polymorphic transitions induced by thermal annealing resulted in a change in the unit cell morphologies and dimensionalities of the molecular superstructures, on the basis of the variations in the present intermolecular interactions determined by the unit cell parameter.

To interpret the experimental results obtained by STM, we carried out extensive periodic density functional theory calculations with a variety of molecular arrangements using the DFT-D2 method, which allows full consideration of the intermolecular interactions including van der Waals forces. The calculations revealed that the first and second most stable superstructures have an energy difference of 0.12 eV per H₂SQ molecule and the calculated unit cell parameters for these superstructures show good agreement with the experimental values for 2D carpet and 1D ribbon, respectively. Therefore, the polymorphic transition from the 1D to 2D superstructure by thermal annealing observed in our STM experiments can be clearly described as a thermodynamic process. Interestingly, the component molecules of the 1D ribbon and 2D carpet structures have different isomers depending on the relative position of the two hydrogen atoms. The less stable 1D structure compared to the 2D structure consists only of ZZ isomers, which are more stable than EZ isomers. On the other hand, after annealing, the 2D structure is composed of only EZ isomers. These results indicate that different driving forces induce the formation of the two superstructures. While the initial formation of the 1D superstructure at room temperature is determined by the relative monomeric stability of the H₂SQ isomers in the gas phase, the polymorphic transition from the 1D to the 2D superstructure by annealing can be explained by a change in the overall stabilization mechanism, from the stability of individual monomers to the stability of the assembled structure.

In summary, we achieved thermally activated dimensional control *via* polymorphic transition of a H₂SQ molecular assembly on Au(111) under UHV conditions. The 1D and 2D molecular arrangements achieved depend on the stability of the conformational isomers and assembled structures.^[4]

Reference

- [1] M. O. Blunt *et al.*, *J. Am. Chem. Soc.*, 2013, **135**, 12068. [2] C. Iacovita *et al.*, *Chem. Eur. J.*, 2012, **18**, 14610. [3] (a) D. Semmingsen *et al.* *J. Chem. Phys.*, 1977, **66**, 4405; (b) T. Shimada, *et al.* *Jpn. J. Appl. Phys.*, 2008, **47**, 1422. [4] K. Ueji *et al.*, *Chem. Commun.*, **50**, 11230-11233. (2014)

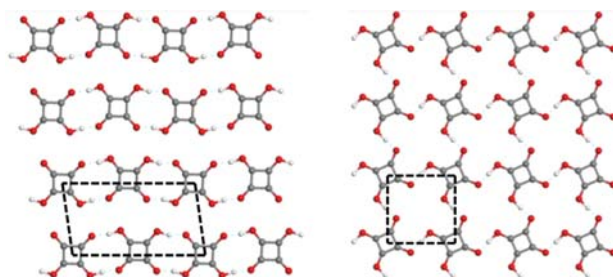


Fig. 2 Optimized superstructure of (left) 1D ribbon and (right) 2D carpet. Dotted lines indicate the unit cells.

Laterally confined dynamics of a bridge-adsorbed CO on Pt(111)

Hyun Jin Yang^{1,2}, Maki Kawai² and Yousoo Kim¹

¹Surface and Interface Science Laboratory, RIKEN

²Department of Advanced Materials Science, The University of Tokyo

Chemisorption of an adsorbate converts all degrees of freedom into vibrational degree of freedom, and dynamic processes of the adsorbate on a surface is described with potential energy surface (PES) in terms of one of the vibrational modes, namely reaction coordinate (RC) modes. Inelastically tunneling electron-induced processes such as lateral hopping, rotation and intramolecular switching also have been described with PES that categorized with the shape and the repetitiveness.¹⁻³ Still most cases are limited to the process of a single molecule free of any intermolecular interaction, and the role of intermolecular interaction has been not investigated yet.

Here we report a surface dynamic process which is described with a novel type double well PES confined inside a local molecular structure composed up of multiple molecules, by means of molecularly resolved imaging and single-molecule spectroscopy using scanning tunneling microscopy (STM). CO adsorbed on Pt(111), the text-book adsorption system, is well known for primary ontop-site occupation with $(\sqrt{3}\times\sqrt{3})R30^\circ$ overlayer structure (near 1/3 ML), followed by $c(4\times 2)$ domain formation that having one ontop CO (CO_T) and one bridge CO (CO_B) at 0.5 ML of surface coverage.⁴ In addition to revealed details of coverage-dependent overlayer structures,⁵ we found that the CO_B enclosed with four CO_T molecules ($c(\sqrt{3}\times 2)$ rect unit, Figure 1a-b) is the stabilized form of CO_B over a wide range of surface coverage. Moreover, the CO_B shows fluctuation of tunneling currents with increased sample bias voltage (V_s), where CO_T molecules never changes the position nor shows any current fluctuation in that V_s range. It was found that this fluctuation is due to lateral shuttling of CO_B onto adjacent ontop site (T) confined inside the $c(\sqrt{3}\times 2)$ rect unit, probed in two-level telegraph-type current in the time trace obtained at the center of $c(\sqrt{3}\times 2)$ rect unit, with $V_s = 227.5$ mV (Figure 1c).

Confinement of CO_B at the center of $c(\sqrt{3}\times 2)$ rect unit, as well as the shuttling motion of it can be described with PES scheme which includes the influence of intermolecular interaction. With assuming the fixed position of CO_T during the motion of CO_B and considering the shortest intermolecular distance confined in the $c(\sqrt{3}\times 2)$ rect unit, the intermolecular interaction imposed to the

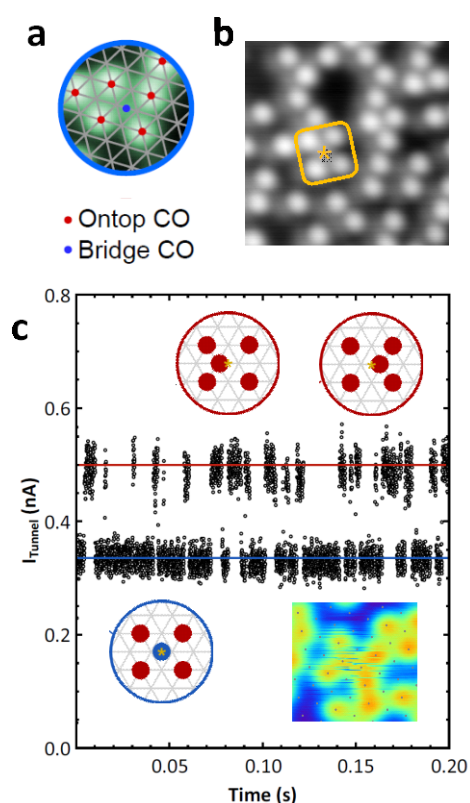


Figure 1 a and b STM images of $c(\sqrt{3}\times 2)$ rect unit, a with superimposed model. c the time trace obtained at 227.5 mV with schematic model of CO_B shuttling and a STM image with the fluctuation.

CO_B with respect to the amount of displacement can be estimated with a simple vector calculation. Resultant PES of the $c(\sqrt{3}\times 2)\text{rect}$ unit constructed by linear combination of estimated intermolecular interaction and PES of an isolated CO is shown at Figure 2a, indicating that (a) the bridge site (B) is indeed stabilized than the adjacent atop site due to the confinement, and (b) the lateral shuttling of CO_B involves a metastable site (T^*) which is distinguished from other CO_T , in terms of the position of minimum with respect to the Pt lattice and the potential energy.

Action spectra of this shuttling motion between B and T site is obtained with time traces at various V_S , as shown in Figure 2b, with the result of numerical fitting to the established model. The threshold at 229 and 252 mV for $\text{B}\rightarrow\text{T}^*$ and $\text{T}^*\rightarrow\text{B}$ hopping coincide to the vibrational energy of C-O internal stretch (IS) mode of CO_B and CO_T , respectively. Thus, the mechanism of this motion above the threshold is considered to be anharmonic coupling of IS mode to the RC mode. Moreover, the estimated reaction constant of $\text{B}\rightarrow\text{T}^*$ hopping fits into the branching ratio with previously known parameters for CO_B , strongly supporting the anharmonic coupling scheme.

Furthermore, the action spectrum of $\text{T}^*\rightarrow\text{B}$, which has never been demonstrated nor measured, gives the first measurement of IS mode energy for a metastable CO_{T^*} . The threshold at 252 mV implies possibly distinguished vibrational energy of IS mode for CO_{T^*} , significantly differ from it of CO_T (260 meV). Also, half-order change in the motion yield at the threshold indicates the stronger contribution of lower energy modes than IS mode for $\text{T}^*\rightarrow\text{B}$ hopping, which is also reasonably explained with the suggested PES with reduced energy barrier and stiffened RC mode energy for T^* than them of T. The contribution of intermolecular interaction is considered with action spectra taken at various surface coverages and the residence time analysis. These quantitative analysis of the hopping motion of COB not only demonstrates the intermolecular interaction-driven motion, but offers new opportunities to measure spectroscopic information of previously unknown metastable state which can be resolved only with microscopic investigation.

[References]

- ¹ T. Komeda, Y. Kim, M. Kawai, B.N.J. Persson, and H. Ueba, *Science* **295**, 2055 (2002).
- ² T. Okada, Y. Kim, M. Trenary, and M. Kawai, *J. Phys. Chem. C* **116**, 18372 (2012).
- ³ W. Auwärter, K. Seufert, F. Bischoff, D. Eciija, S. Vijayaraghavan, S. Joshi, F. Klappenberger, N. Samudrala, and J.V. Barth, *Nat Nano* **7**, 41 (2012).
- ⁴ H. Steininger, S. Lehwald, and H. Ibach, *Surf. Sci.* **123**, 264 (1982).
- ⁵ H.J. Yang, T. Minato, M. Kawai, and Y. Kim, *J. Phys. Chem. C* **117**, 16429 (2013).

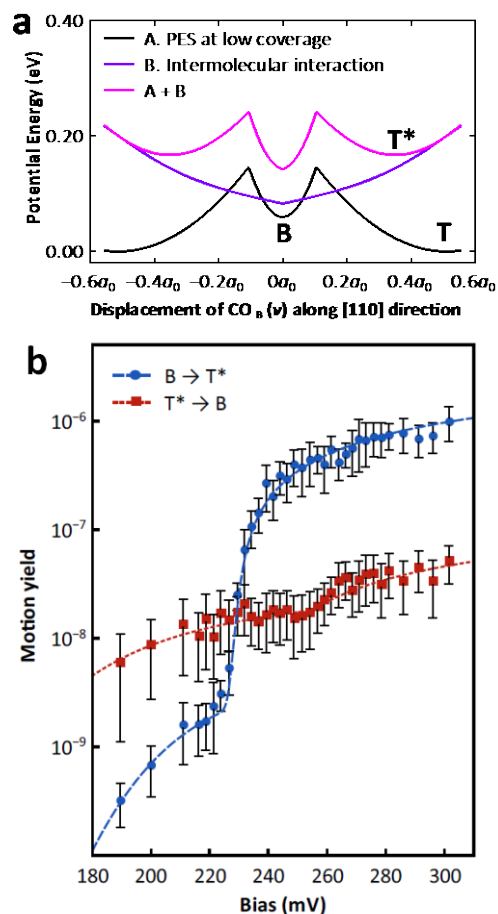


Figure 2 **a** Constructed PES for a $c(\sqrt{3}\times 2)\text{rect}$ unit, **b** the action spectra for $\text{B}\rightarrow\text{T}^*$ (blue circle) and $\text{T}^*\rightarrow\text{B}$ hopping (red square).

Surface morphology of atomic nitrogen on Pt(111)

Zhu Liang¹, Hyun Jin Yang^{2,3}, Yousoo Kim² and Michael Trenary¹

¹Department of Chemistry, University of Illinois at Chicago

²Surface and Interface Science Laboratory, RIKEN

³Department of Advanced Materials Science, The University of Tokyo

Knowledge of adsorbate structure is essential to understand the surface reaction mechanisms, which provides basic understanding on the practical catalysis. Some of those reactions accompany the formation of atomic adsorbates such as atomic oxygen (O), hydrogen (H) and nitrogen (N). However, comparing to extensively-studied atomic H and O on Pt(111) surface, there are only limited number of studies for atomic N due to difficulties in producing clean N layer. For the investigation of atomic N layers, oxydehydrogenation reaction of ammonia with atomic oxygen ($3\text{O}(\text{ad})+2\text{NH}_3(\text{ad})\rightarrow 2\text{N}(\text{ad})+3\text{H}_2\text{O}(\text{g})$) has been suggested to form ordered overlayer of N,¹ characterized with low-energy electron diffraction (LEED) with two superstructures, (2×2) and $(\sqrt{3}\times\sqrt{3})\text{R}30^\circ$.²

In this study we achieved well ordered overlayer of atomic N at different surface coverages, at the atomic level with low temperature scanning tunneling microscopy (STM), by means of modified ammonia oxydehydrogenation reaction ($3\text{O}_2(\text{ad})+4\text{NH}_3(\text{ad})\rightarrow 4\text{N}(\text{ad})+6\text{H}_2\text{O}(\text{g})$)(Figure 1a). The oxydehydrogenation reaction was achieved by annealing $\text{NH}_3\text{-O}_2$ covered surface to temperatures between 300 and 400 K, and controlling the ratio of two gases, the amount of exposure and the annealing temperature resulted in the desired overlayers with various compositions and coverages, including previously reported (2×2) and $(\sqrt{3}\times\sqrt{3})\text{R}30^\circ$ structures(Figure 1b).

If the exposures were high but the amount of ammonia was not enough to remove all the oxygen from the surface, the annealing to 370 K resulted in a mixed N and O overlayer as shown in Figure 2a. Coadsorbed N and O form a mixed $(2\times 2)\text{-N+O}$ phase, as indicated with blue circle (N) and red circle (O), with almost constant N:O ratio (0.56:0.44). Atom-resolved images with modified STM tip and the precise imaging of step edge clearly revealed that both N and O atoms occupies the face-centered-cubic hollow sites. While both atoms appear as depressions, the O atoms are deeper than the N atoms, which is in good agreement with theoretical simulations.³

Precise control of stoichiometry between ammonia and oxygen gives that pure N overlayers, from isolated

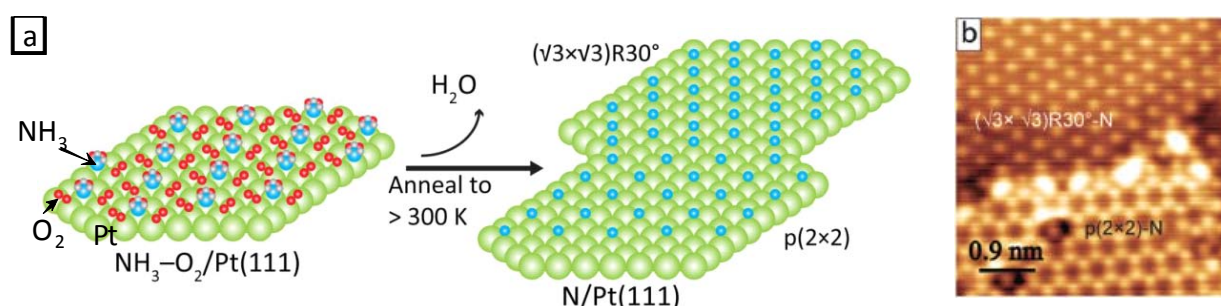


Figure 1 (a) Schematic drawing of the oxydehydrogenation reaction for atomic N on Pt(111), and (b) representative overlayer structures of atomic N, $p(2\times 2)$ and $(\sqrt{3}\times\sqrt{3})\text{R}30^\circ$.

molecules to (2×2) and $(\sqrt{3}\times\sqrt{3})R30^\circ$ phases. Isolated N atoms on Pt(111) appear as depressions in the STM images at low coverages as shown in the left part of Figure 2b, which is different from the dense N layer which appears in ordered overlayer structures (right part of Fig. 2b and Figure 3c). This is attributed to the interference effect between tunneling channels through overlapping orbitals at neighboring atoms. Fully covered, dense N islands appeared in two phases, (2×2) (Fig. 3c) and $(\sqrt{3}\times\sqrt{3})R30^\circ$ (Figure 3d), which are consistent with previous LEED studies. The determining factor for the ratio between $(\sqrt{3}\times\sqrt{3})R30^\circ$ and (2×2) phase is the annealing temperature, where $(\sqrt{3}\times\sqrt{3})R30^\circ$ phase dominates at lower (<360) temperature while (2×2) phase dominates at $T > 400$ K. This is due to a N coverage decrease associated with the onset of $N_2(g)$ desorption at 400 K, as well as the stability of (2×2) phase over $(\sqrt{3}\times\sqrt{3})R30^\circ$ structure. Detailed investigation of (2×2) phase revealed that there are two types of Pt atoms with different apparent heights, where the more brighter Pt atom is in contact with N atom while less brighter Pt is not, confirmed with STM images at various sample bias voltage. For higher-coverage $(\sqrt{3}\times\sqrt{3})R30^\circ$ structure shows uniform hexagonal lattice, with only one type of Pt atom. Most of the defects in the N overlayer are at the boundaries between the two phases or at the boundaries between domains of the same phase. Within a domain the defect density is as low as 0.8%, while domain sizes as big as $20\text{ nm} \times 20\text{ nm}$ were observed.

The establishment of the conditions for preparing pure and well-ordered layers of nitrogen on Pt(111), and the determination of the exact structure of these layers at the atomic level, paves the way for future studies by both experimental and theoretical methods of the reactivity of nitrogen with other adsorbed atoms and molecules as a way to establish mechanisms of surface chemical reactions that are of relevance to important problems in heterogeneous catalysis.

[Reference]

1. T. S. Amorelli, A. F. Carley, M. K. Rajumon, M. W. Roberts, and P. B. Wells, *Surf. Sci.* 315, L990 (1994).
2. E. Herceg, J. Jones, K. Mudiyansele, and M. Trenary, *Surf. Sci.* 600, 4563 (2006).
3. P. Sautet, *Surf. Sci.* 374, 406 (1997)

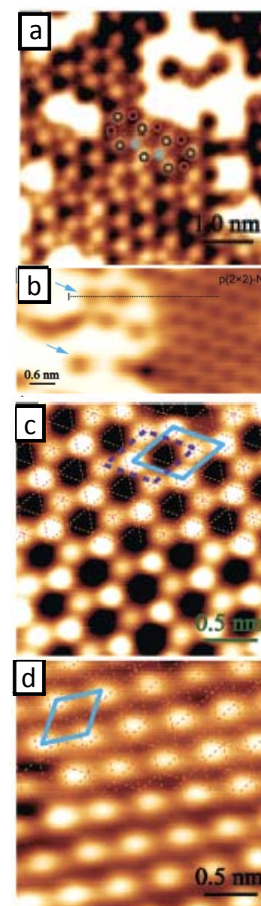


Figure 2 Various phase of overlayer structures obtained: (a) mixed (2×2) -N+O, (b) low-coverage N, (c) $p(2\times 2)$ -N and (d) $(\sqrt{3}\times\sqrt{3})R30^\circ$ phases.

磁性不純物問題に対するブロックランチョス密度行列繰り込み群法

白川知功, 柚木清司

理研・柚木計算物性物理

分子システムにおける磁性不純物問題は、グラフェンに吸着した水素や酸素などの吸着原子・分子の磁性出現の問題から、遷移金属タンパク質中の遷移金属イオンのスピン状態、例えば、ミオグロビン中の鉄のスピン状態など、非常に広範囲な対象を含んだ極めて基本的な問題のひとつである。磁性あるいはスピン出現の起源は電子間クーロン相互作用であり、したがってこれらの分子システムは典型的な強相関電子系と見ることができる。固体物質中の磁性不純物問題は、近藤問題として物性物理科学の分野では昔から知られており50年以上も研究されている。その過程で開発された理論的手法としては、近似的解析方法や一部の特殊な模型の厳密解の他に数値的繰り込み群法（NRG法）を用いた数値計算手法などがあげられる。特に、NRG法は固体物質中の近藤効果解明に重要な役割を果たした。しかしながら、NRG法をはじめこれらの手法では、上述した分子システム中の磁性不純物問題、例えば、スピン密度の空間的分布の解析や遷移金属イオンにおけるスピン多重項効果などを取り扱うには不十分である。そこで、我々は、この困難を解決するために、磁性不純物問題に対する新しい数値計算手法の開発を行っている。

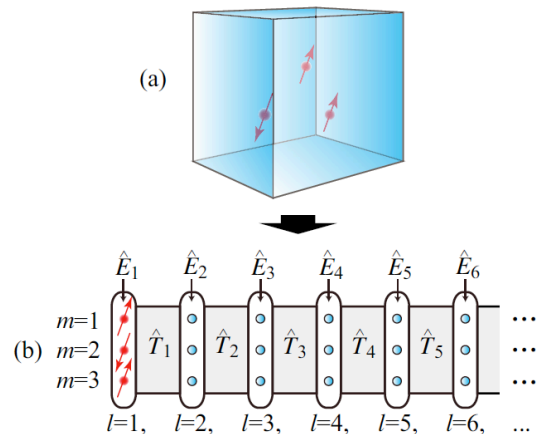


図1: 3次元伝導バンド中にある三つの磁性不純物模型(a)はBL変換により3レッグ梯子模型(b)に変換される。空間的に離れた位置に存在する三つの不純物サイト(矢印を伴った赤丸)は、BL変換によりそのまま梯子模型の一番左端($l=1$)に移される。従って、不純物サイト中のクーロン相互作用はBL変換後も局所的である。

そのひとつの方法として、我々はブロックランチョス密度行列繰り込み群法（BL-DMRG法）を新たに提案した[1]。密度行列繰り込み群法（DMRG法）は1992年にS. Whiteにより提案され、それ以来物性物理科学の分野では、強相関量子系を中心として非常に盛んに用いられている。DMRG法では、系を部分系と環境のふたつにわけ部分系の密度行列を少数の基底で十分精度よく表すように基底を最適化する方法で、次元を中心とした低次元系に非常に有力な方法である。したがって、DMRG法を直接、磁性不純物問題に適用する場合、その有効性は基本的には次元磁性不純物模型に限られる。我々は、ブロックランチョス（BL）変換を用いてまず磁性不純物模型を次元（あるいは数レッグ梯子模型）に変換し、得られた模型に対してDMRG法を用いることを提案（BL-DMRG法）した（図1参照）。BL-DMRG法では、次元に限らず2、3次元磁性不純物模型を取り扱うことができ、しかも複数の軌道から構成される磁性不純物に対してもそのスピン多重項効果を近似なく取り扱うことが可能である。これは、BL変換においては最初の基底を磁性不純物サイトに選ぶことによって、磁性不純物サイト内のクーロン斥力

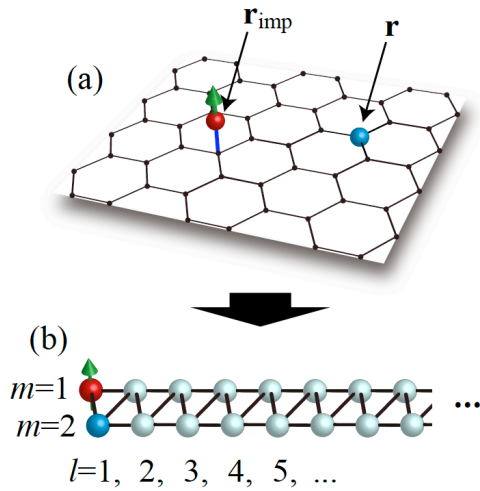


図 2: グラフェン中の磁性不純物サイト (r_{imp}) と伝導サイト (r) との実空間スピン相関関数は、BL 変換において最初の基底として磁性不純物サイトと注目する伝導サイトを選ぶことによって BL-DMRG 法により計算出来る。

磁性不純物の場合、図3より一見磁性不純物スピンの遮蔽されているように見えるが、実はそのスピンは遮蔽されていないこと、したがって、近藤効果が起きていないことを意味している。BL-DMRG法では動的相関関数も計算することができ、磁性サイトの局所状態密度および局所スピン感受率の計算結果は、近藤効果が起きていないこととコンシステントであることも確認できた。

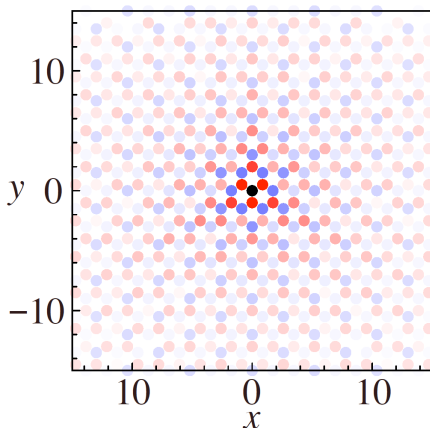


図 3: 磁性不純物-伝導電子実空間スピン相関関数 $S_i(\mathbf{r})$ 。磁性不純物は中心の黒丸に位置する。伝導サイトは $\mathbf{r}=(x,y)$ に位置し、色の違い (赤: 正、青: 負) が $S_i(\mathbf{r})$ を示している。

が変換後得られた梯子模型でも局所的のままだからである (図1)。

BL-DMRG法の応用例として、グラフェン内の磁性不純物問題に適用した。BL-DMRG法では、従来の方法 (NRG法等) では計算が困難であった量、例えば、磁性不純物周りのスピン分布も実空間で計算が可能になった。それは、BL変換を行う際に最初の基底として磁性不純物サイトと注目しているサイトを選ぶことによってBL-DMRG法を行うことが出来る (図2)。

BL-DMRG法により計算した磁性不純物-伝導電子実空間スピン相関関数 $S_i(\mathbf{r})$ の一例を図3に示す。伝導電子のスピンが磁性不純物スピン (黒円で示されたサイトにひとつ存在) を遮蔽している様子が実空間で分かる。もう少し定量的に調べるために図4に $S_i(\mathbf{r})$ を $|\mathbf{r}|$ の関数として示す。磁性不純物がない場合 (図で赤丸) と比べてみると、 $S_i(\mathbf{r})$ の遠方での振る舞い $|\mathbf{r}|^{-\alpha}$ の冪 α が2から3へと異なっていることがわかる。つまり、この

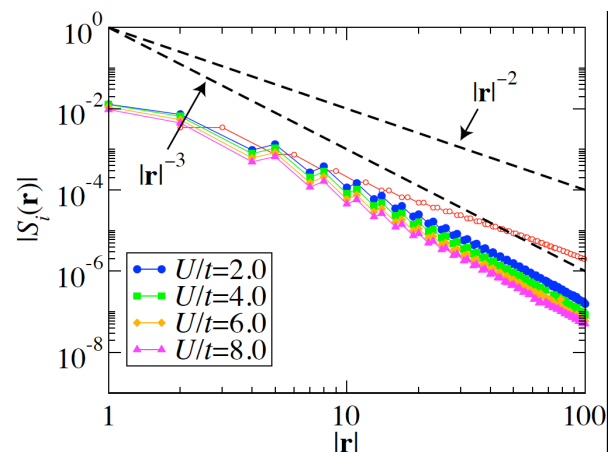


図 4: 磁性不純物-伝導電子実空間スピン相関関数 $S_i(\mathbf{r})$ 。 U は不純物サイトのクーロン斥力の強さを表す。赤丸はクーロン相互作用がない場合の $S_i(\mathbf{r})$ 。

【参考文献】

- [1] T. Shirakawa and S. Yunoki, Phys. Rev. B **90**, 195109/1-21 (2014).

Block Lanczos Density-Matrix Renormalization Group Method for General Magnetic Impurity Models

Tomonori Shirakawa, Seiji Yunoki

Computational Condensed Matter Physics Laboratory, RIKEN

Magnetic impurity problems in molecular systems include a wide range of complexes. The typical examples are the emergence of magnetic moment in adatom such as hydrogen and oxygen absorbed onto graphene, and the spin state of transition metal ion in metalloprotein such as an iron ion in myoglobin. The origin of magnetism is due to Coulomb interactions among electrons and thus these molecular systems are considered as typical strongly correlated electronic systems. The magnetic impurity problems in solid materials, known as the Kondo problem, have been studied over 50 years in the field of condensed matter physics. During the course of these studies, many theoretical approaches have been developed, including approximate analytical methods, analytically exact solutions for several special cases, and numerical methods such as numerical renormalization group (NRG) method. Specially, the NRG method has played a major role on understanding the Kondo effect in solids. However, these approaches are not enough to address the magnetic problems in the molecular systems, for example, to resolve the magnetic moment distribution around the magnetic impurity in real space and to understand the spin multiplet effects. To overcome these difficulties, we have been developing new numerical approaches for the magnetic impurity problems.

As one of the promising approaches, we have recently proposed block Lanczos density-matrix renormalization group (BL-DMRG) method [1]. The density-matrix renormalization group (DMRG) method was originally proposed in 1992 by S. White and since then it has been extensively employed to study various strongly correlated quantum systems in condensed matter physics. However, the power of this method is limited to one-dimensional (1D) systems and quasi 1D systems (i.e., a few leg ladder systems). Therefore, the direct application of DMRG method to the impurity problems in two or three dimensions is not realistic. Instead, we have shown that the block Lanczos (BL) transformation of any impurity models in any spatial dimensions can be mapped onto effective 1D or quasi-1D models with the magnetic impurity sites untouched, and thus the Coulomb interactions on the impurity sites remain local in the resulting effective models (see Fig.1). After the BL transformation, we can safely apply the DMRG method to examine the impurity properties.

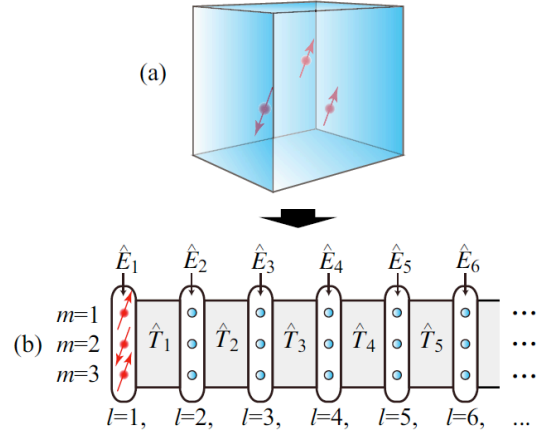


Fig.1: A magnetic impurity model with three magnetic impurities (a) is mapped exactly onto an effective three-leg ladder model (b) by the BL transformation. The three impurity sites (indicated by red circles with arrows) located separately in real space are transferred onto the three sites on the left most rung in the resulting ladder model, and thus the Coulomb interactions on the impurity sites remain local.

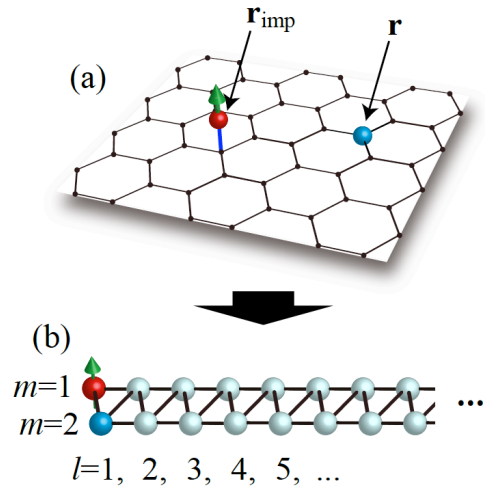


Fig.2: Spin correlation function $S_i(\mathbf{r})$ between the impurity site (\mathbf{r}_{imp}) and the conduction sites (\mathbf{r}) can be calculated by taking the impurity site and the conduction site for interest as the initial BL bases in the BL-DMRG method

the surrounding conduction electrons. To quantitatively understand the behavior, Fig.4 shows $S_i(\mathbf{r})$ as a function of $|\mathbf{r}|$. Comparing the results for the case with no magnetic impurity (denoted by red circles), it is clearly observed that $S_i(\mathbf{r})$ behaves as $|\mathbf{r}|^{-\alpha}$ with $\alpha=3$ in the asymptotic reason, instead of $\alpha=2$ as in the case with no magnetic impurity. This implies that the magnetic spin is not completely screened and thus no Kondo effect occurs in this impurity model. The BL-DMRG method can also calculate dynamical quantities and we find that the results for the local magnetic susceptibility and the local density of state at the Fermi level

are good qualitative agreement with the ones for $S_i(\mathbf{r})$, i.e., no Kondo screening.

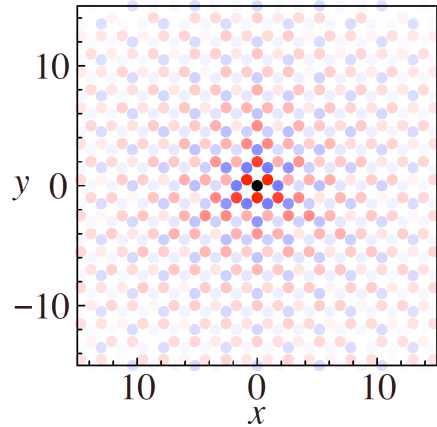


Fig.3: Spin correlation function $S_i(\mathbf{r})$ between the impurity site and the conduction site. The magnetic impurity is located at the center (indicated by a black circle). The conduction site is located at $\mathbf{r}=(x,y)$ and the color difference indicates the value of $S_i(\mathbf{r})$ (red: positive, blue: negative).

We have applied the BL-DMRG method to study the impurity problem in graphene. The BL-DMRG method allows us to calculate the spatial distribution of spins around the magnetic impurity, which is sometimes problematic in other numerical methods such as the NRG method. The reason why the BL-DMRG can calculate these spatially dependent quantities in real space is because when the BL transformation is applied we can take the impurity site and the conduction site for interest as the initial Lanczos bases so that these two sites are isolated in the resulting two-leg ladder model with the Coulomb interactions remaining local (see Fig.2).

Figure 3 shows an example of the spin correlation function $S_i(\mathbf{r})$ between the impurity site (\mathbf{r}_{imp}) and the conduction site (\mathbf{r}). It is noticed in Fig.3 that the impurity spin at the center (indicated by a black circle) is screened by the

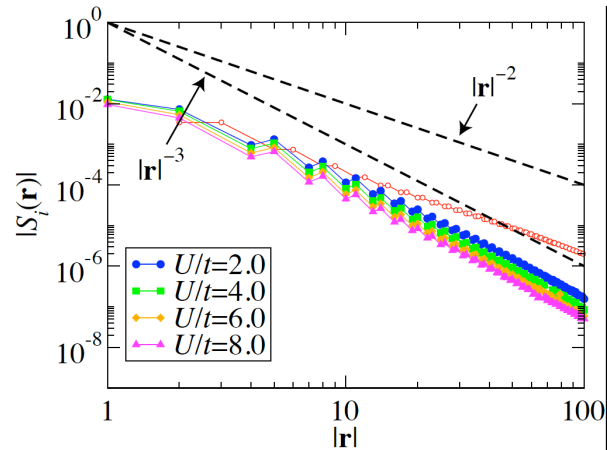


Fig.4: Spin correlation function $S_i(\mathbf{r})$ between the impurity site and the conduction site. U denotes the Coulomb interaction on the impurity site. For comparison, $S_i(\mathbf{r})$ for the non-interacting limit is also plotted by red circles.